UNIVERSITY OF CALIFORNIA
RIVERSIDE

Measurement of Transverse Single Spin Asymmetry for π^0 Production in Polarized Proton Proton Collisions at $\sqrt{s} = 510$ GeV

A Dissertation submitted in partial satisfaction
of the requirements for the degree of

Doctor of Philosophy

in

Physics

by

David Kapukchyan

March 2025

Dissertation Committee:

Dr. Kenneth N. Barish, Chairperson
Dr. Richard Seto
Dr. Miguel I. Arratia Munoz

The Dissertation of David Kapukchyan is approved:

Committee Chairperson

University of California, Riverside

Acknowledgments

I have been fortunate enough to have so many people support me in my academic endeavors throughout the years. I would like to start first by thanking my family for their continued support without which I could not have pursued my dreams in science. First my Yaya, who taught me the importance of education and learning. My mom and dad, Narine and Hovsep, who have always supported me even though they didn't really understand why I have chosen this path. My older brother Samvel who has always been there for me and encouraged me. My younger brother Manvel who always believes in my success and pushes me to that end, along with his wife Kathleen, and their children who provide me with a great sense of joy. My grandparents, Maritza and Karapet Bandikyan, who continue not just to encourage my intellectual pursuits but, along with the rest of my family including my uncles, cousins, aunts, etc., my personal ones as well to be a better person. I want to thank my advisor Ken Barish, who has supported me over the years as I pursued my many interests and projects. He was always there whenever I needed anything or wanted to try something new and would never discourage me from trying. I would also like to thank Akio Ogawa, who I have worked with closely over these years and learned many things from him and throughly enjoyed our conversations. I would also like to thank Oleg Eyser who could I always count on for his useful advice. I would also like to thank Elke Aschenauer who helped make this analysis possible with her tireless efforts to get the forward upgrade built and running. I would also like to thank Bill Christie, and Bob Soja who helped me to better understand STAR and whose help made me a better experimentalist. I would also like to thank Tim Camarada whose help I can always count on when I was working at STAR.

Oleg Tsai who was instrumental in the construction of the detectors I used in this analysis and whose insight helped me understand calorimeters better. Stephen Trentalange for his help and advice. Gerard Visser who helped me better appreciate electronics. Tonko who was always there when I needed help to interface with STAR. Last, but certainly not the least, Carl Gagliardi for his useful insights and help in getting the FCS built and running. I would also like to thank the many engineers, technicians, and scientists at BNL without whose effort this work would not be possible.

To Voski – my yaya – who put me on this journey

ABSTRACT OF THE DISSERTATION

Measurement of Transverse Single Spin Asymmetry for π^0 Production in Polarized Proton Proton Collisions at $\sqrt{s} = 510$ GeV

by

David Kapukchyan

Doctor of Philosophy, Graduate Program in Physics
University of California, Riverside, March 2025
Dr. Kenneth N. Barish, Chairperson

The Transverse Single Spin Asymmetry (TSSA) in polarized proton proton collisions has proved to be a valuable tool in understanding the internal structure of the proton. Specifically, to understand the origin of the proton's spin. Initially, it was thought that the three quarks that make up the proton solely contribute to the proton's spin. However, experiments showed that the spin contribution of the quarks is insufficient to account for the total spin. Current theories posit that the quarks and gluons (partons) inside a proton carry transverse momentum that is coupled to the proton's spin which affects the production of the particles generated with respect to the polarization. The TSSA measures this asymmetry of particle production for a proton whose spin is polarized transverse to its momentum. The measurement of the TSSA provides input into those theoretical models to understand the different contributions of the quarks and gluons to the overall spin. To measure the π^0 TSSA, polarized beams of protons are generated at the Relativistic Heavy Ion Collider (RHIC). The detector at RHIC utilized in this dissertation is the Solenoidal Tracker At RHIC (STAR) and a major part of this work was building, installing, and commissioning

an upgrade to the STAR detector system. The upgrade expanded STAR's tracking and calorimetry capability for 2.5<pseudorapidity(η)<4.0. This dissertation will describe the calorimeter upgrade as well as the measurement of the π^0 TSSA as a function of Feynman-x (x_F). The result is consistent with previous measurements and highlights the first success of the upgrade to produce a physics observable. The data for this measurement was taken in 2022-2023 which had the largest luminosity of polarized proton proton collisions at 510 GeV compared to previous years and is expected to reduce the errors on the TSSA from those previous measurements.

Contents

List of Figures

List of Tables

List of Acronyms

RHIC	Relativistic Heavy Ion Collider
BNL	Brookhaven National Laboratory
STAR	Solenodial Tracker at RHIC
fSTAR	Forward STAR Upgrade
FCS	Forward Calorimeter System
EM	Electromagnetic
Ecal	FCS Electromagnetic Calorimeter
Hcal	FCS Hadronic Calorimeter
fPre	FCS Preshower
DEP	Detector Electronics Platform
LINAC	Linear Accelerator
AGS	Alternating Gradient Synchotron
ADC	Analog to Digital Conversion in most contexts it means the digital value itself
TAC	Time Analog Conversion which is the digital value that represents a time ADC
TB	Time Bin

pC	Proton Carbaon Polarimeter
HJet	Hydrogen Jet Polarimeter
TPC	Time Projection Chamber
BBC	Beam Beam Counter
VPD	Vertex Position Detector
EPD	Event Plane Detector
SiPM	Silicon Photomultiplier
Pb	Lead (the element)
Sc	Scintillator
WLS	Wavelength Shifting
FEE	Front End Electronics (board)
PCB	Printed Circuit Board
LED	Light Emitting Diode
MIP	Minimum Ionizing Particle
Fe	Iron
Au	Gold
TSSA	Transverse Single Spin Asymmetry
QA	Quality Assurance

Chapter 1

Introduction

I have always been fascinated by atomic theory. In particular, thinking about and trying to understand how the fundamental constituents of matter behave and how that behavior gives rise to larger scale systems that we observe. As history shows, this fascination is not unique and has lead to some of the most interesting scientific advancements in the last two centuries. The discovery of the atomic structure of matter and the subsequent subatomic matter of electrons, protons, and neutrons has changed our understanding of the universe. However, there is still much we don't understand about their behavior. In the case of protons and neutrons we have discovered a rich substructure that is thousands of times smaller than the atomic. It is in trying to understand this substructure that is the focus of this dissertation.

1.1 Foundations of the Modern Particle Experiments

Cathode rays, studied by J.J. Thomson, gave evidence of a new particle, namely the electron. Later, Milikan and Fletcher performed the oil drop experiment which more accurately measured the charge of the electron. Concurrently, Rutherford using the electron developed an atomic theory to rival the plum pudding model which placed a dense positively charged nucleus at the center of atoms [38]. This theory was confirmed by measuring the scattering angle of α particles off a thin gold film [23]. Their results showed that alpha particles back scatter which is only possible if Rutherford's theory was correct. This was led to the initial model of the atom of a positive dense nucleus surrounded by light negatively charged particles.

Further developments into this atomic model came from Bohr and Sommerfeld who were able to calculate the energy spectrum of hydrogen by quantizing angular momentum. The idea of quantization was not new and was used earlier by Planck to explain the blackbody spectrum of heated objects by quantizing energy. The quantization of angular momentum was confirmed by Stern and Gerlach whose experiment was designed to see if silver atoms would be split in an inhomogeneous magnetic field. Their results were consistent with the predication that the beam would split.

As the atomic model was coming together there was one last thing needed to complete the picture. Scientists had observed a fine structure in spectroscopy experiments with atoms when the atoms were exposed to magnetic fields. This fine structure was due to the coupling of the magnetic field generated by the electron orbit to the external one. However, there was an additional hyperfine splitting that was observed and dubbed the

Anomalous Zeeman effect. This effect was explained when you add a fourth quantum number to the existing atomic model, namely spin. So named because it represents another component of the total angular momentum and couples to the magnetic field. It is the coupling of the electron spin to the external magnetic field that explained the hyperfine splitting.

This completed the atomic model as it is known today. However, the importance of this story is how experiments utilizing spectroscopy, scattering, and radiation led to the development of this theory. These are the same kinds of experiments we still use today to probe even deeper into the atomic and even the subatomic.

1.2 Probing Subatomic Matter

This section will present a brief overview of the two models that came out as a result of high energy physics experiments with nuclei. One is the parton model and the other is the quark model. Both were useful in describing different experimental observables, which will be discussed. The unification of both models (through experiments) is the foundations of our current understanding of nucleon structure.

1.2.1 Development of the Parton Model

The discovery of the proton and neutron were the first indications that the atomic nucleus is made up of more fundamental particles. The first evidence of an internal structure of nucleons like protons came from colliding electrons with protons and measuring the outgoing electrons energy and momentum. This particular process is called Deep Inelastic

Scattering (DIS) and a diagram with some of the relevant variables can be found in 1.1. The differential cross section for scattering electrons from a point charge is given by eq. 1.1. Where $\left(\frac{d_\sigma}{d_\Omega}\right)_{point}$ is the differential cross section ($d\sigma$) for scattering electrons from a point charge into some solid angle $d\Omega$ and $F(q)$ is the form factor. $q = k - k'$ is the four momentum transfer as shown in fig. 1.1. In fact, $\left(\frac{d_\sigma}{d_\Omega}\right)_{point}$ is equal to $\left(\frac{d_\sigma}{d_\Omega}\right)_{Mott}$ for a structureless target [27].

$$\frac{d_\sigma}{d_\Omega} = \left(\frac{d_\sigma}{d_\Omega}\right)_{point} |F(q)|^2 \tag{1.1}$$

The results of measuring this cross section in DIS experiments is shown in fig. 1.2, it shows that the measured cross section does not match the Mott cross section. Therefore the proton must contain a substructure [19]. This is where the form factor in eq. 1.1 becomes useful because we can write the unpolarized inelastic $ep \to eX$ differential scattering cross section, shown in eq. 1.1, which contains the structure functions W_1 and W_2, which are related to the form factors in eq. 1.3 [12].

$$\frac{d^2\sigma}{d\Omega dE'} = \frac{4\alpha^2 E'^2}{q^4}\left(2W_1 sin^2\frac{\theta}{2} + W_2 cos^2\frac{\theta}{2}\right) \tag{1.2}$$

Here α is the fine structure constant, E' is the energy of outgoing electron $k' = (E', \overrightarrow{k}')$, θ is the scattering angle in the lab frame, and W_1 and W_2 are the structure functions and are related to the form factors in the Bjorken limit (deep inelastic regime or "free" particles) $-q^2 = Q^2 \to \infty$ $\nu = E - E' \to \infty$ by eq. 1.3 [12][27].

$$\lim_{Q^2 \to \infty} \nu W_2 = F_2$$
$$\lim_{Q^2 \to \infty} M W_1 = F_1 \tag{1.3}$$

Measurements of F_2 as a function of Bjorken-x (x_B or just x) and various Q^2 is shown in fig. 1.3. They show that for a fixed x, F_2 does not vary strongly with Q^2. This was first described by Bjorken and is thus called Bjorken Scaling and the variable is thusly named for him as well. The presence of Bjorken scaling indicates that the proton is in fact made up of much smaller constituents which were (and still) called "partons" by Bjorken [27]. Furthermore, it can be shown that quantity x is identical to the momentum fraction of the struck parton and one can write a Parton Distribution Function (PDF) to describe the probability of finding a parton with a given momentum x. In this sense, the form factors $F_{1,2}$ now only depend on x and are independent of Q^2 as evidenced by the data. However, as can be seen at smaller x this dependence changes, but the overall idea and the scaling variables are still relevant.

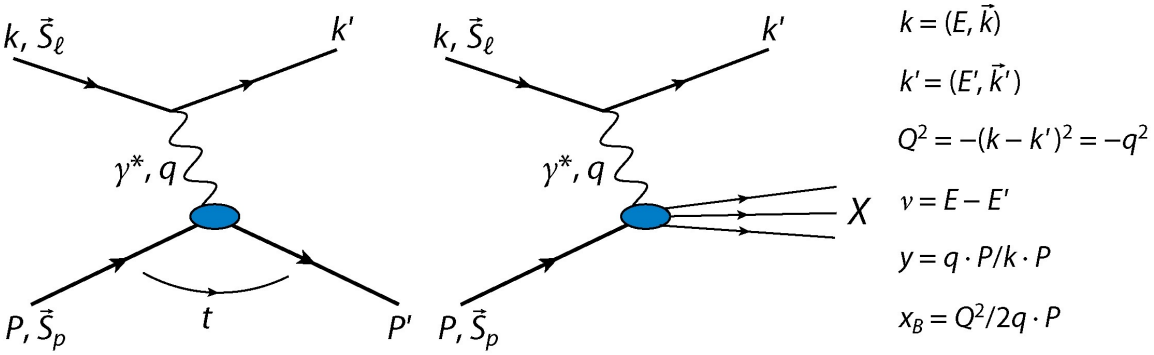

Predekamp MG, Yuan F. 2015.
Annu. Rev. Nucl. Part. Sci. 65:429–56

Figure 1.1: A schematic showing deep inelastic process with its relevant kinematic quantities.[25]

1.2.2 Quark Model

The quark model was developed by Murray and Gell-Mann to explain the large amount of particles observed in the 1960's. However, before talking about the quark model it is important to note preceding its development a similar theory using a quantity called "isospin" was developed.

Isospin was developed after noticing, by Heisenberg, that the proton and neutron have a similar mass and therefore could be two states of the same particle, the "nucleon". In this theory, the nucleon can be written as a two component column matrix such that the basis of this space is is the proton ($p = \begin{pmatrix} 1 & 0 \end{pmatrix}^T$) and the neutron ($n = \begin{pmatrix} 0 & 1 \end{pmatrix}^T$). The isospin formalism written this way is reminiscent of the spin formalism used in quantum mechanics and thus follows the same formulation. However, isospin is not related to the

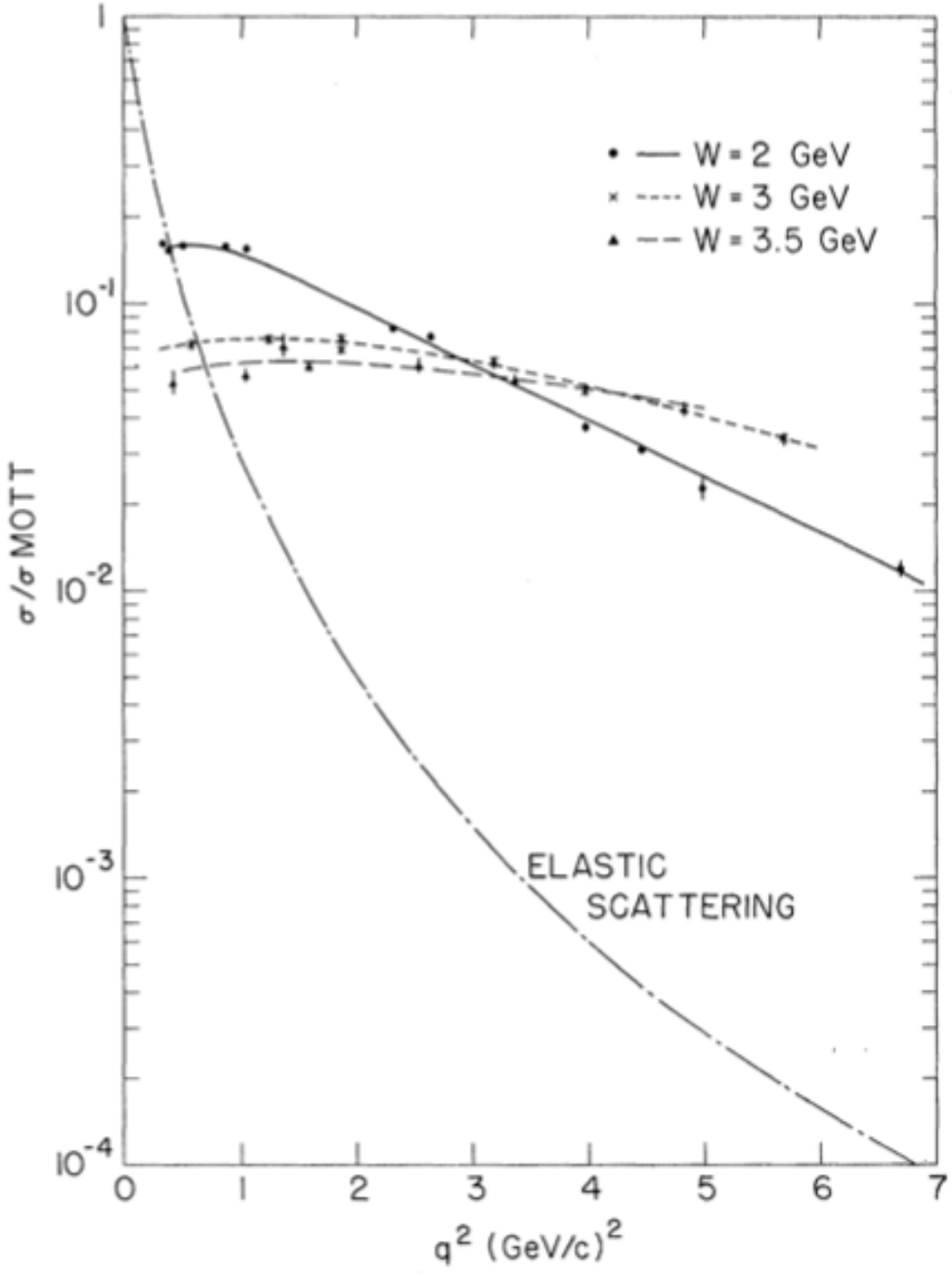

Figure 1.2: Measurement of the differential cross section in ep scattering vs. q^2 for various W, where W is the recoil mass ($W^2 = (P+q)^2$). Also shown is the expected elastic scattering curve. There is slow variation with q^2 which suggests the proton has substructure [19].

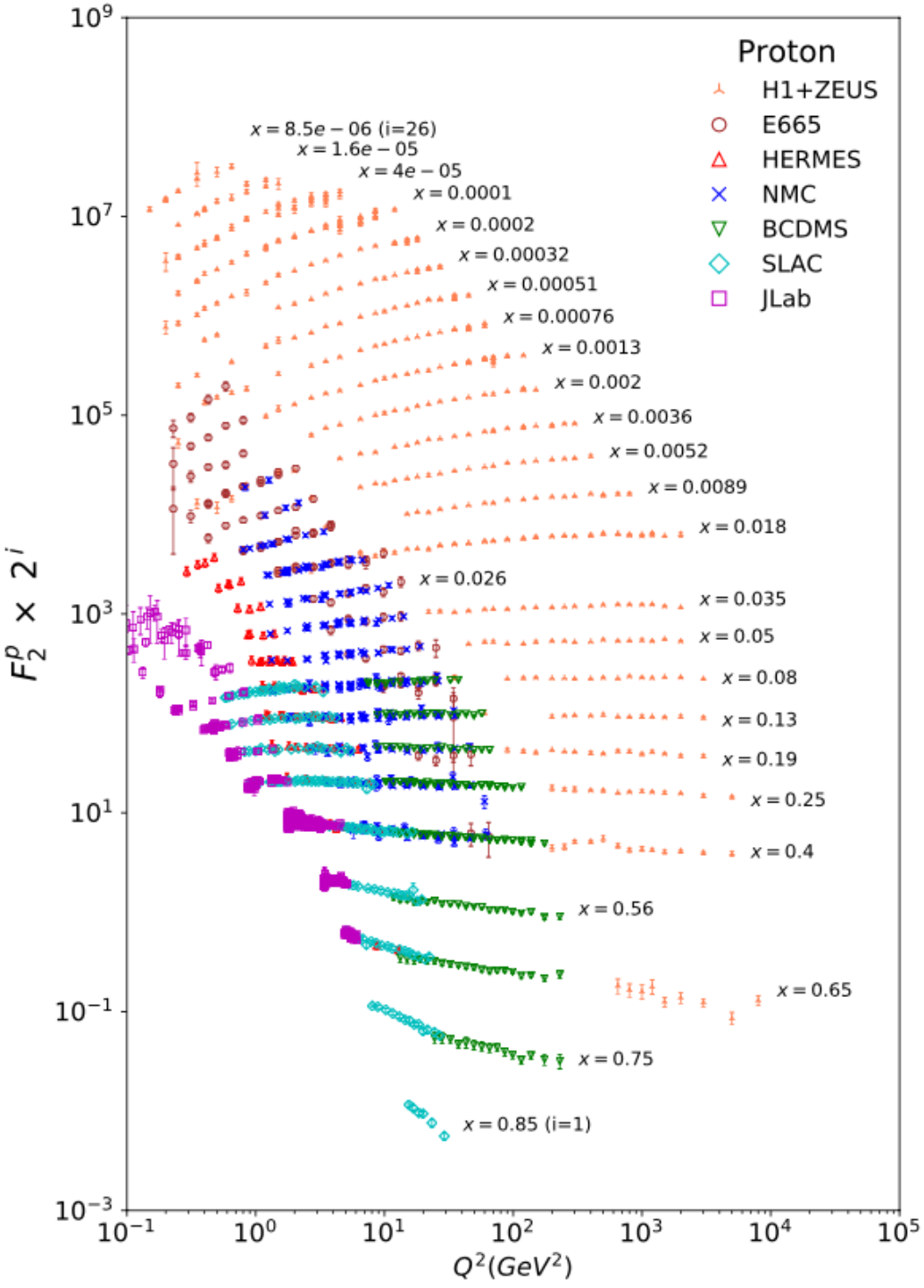

Figure 1.3: The proton structure function F_2 measured in electromagnetic scattering of electrons and positrons on protons, and electrons/positrons and muons on a fixed target from various experiments. At high x, there is very little dependence on Q^2 which suggests that protons are made up of smaller particles. At lower x the dependence is stronger however, the overall idea of partons is still reinforced. [34].

angular momentum but is merely a convenient and analogous space to understand the strong force. Just like spin in quantum mechanics isospin (I) has components I_1, I_2, I_3 and thus we can use these to make connections between the spin theory and isospin, where I_3 takes the role of S_z. The proton then has isospin state $p = \left|\frac{1}{2}\,\frac{1}{2}\right\rangle$ and the neutron $n = \left|\frac{1}{2}\,-\frac{1}{2}\right\rangle$. Using this formalism one can make different states to represent different particles that were being discovered at the time like π's, Δ's, Σ's, and Ξ's and isospin could be used to understand their production and decays. However, it was becoming clear that there was a larger structure at play. In addition, looking at production of Kaons suggested the existence of another quantum number, namely strangeness S. This new quantum number would be incorporated into a new theory of quarks where rather than using the p and n as a basis the quarks u, d, and s would serve as the basis of the representation in SU(3). [24] [27].

Using the quark model one can construct the baryon octet (baryons now being a combination of 3 quarks) which contains the proton and neutron as shown in fig. 1.4. The diagram also shows where the particles sit on the quantum numbers of isospin I_3 and strangeness S. These 3 quarks (and anti-quarks) can be used to form the meson nonet, where a meson is a combination of a quark and anti-quark; it contains the π's, K's, η's. Most notably, the quark theory predicated a new as of yet undiscovered Ω^- particle that was made up of 3 strange quarks, it can be seen in the baryon decuplet in fig. 1.5 [14].

The discovery of more exotic particles like the J/ψ led to the addition of the charm, bottom, and top quarks into the model extending the quark flavors from 3 to 6. Furthermore, there was evidence of another quantum number, color, to overcome the Pauli exclusion principle for particles like the Δ^{++} which has all its quarks in the same spin up

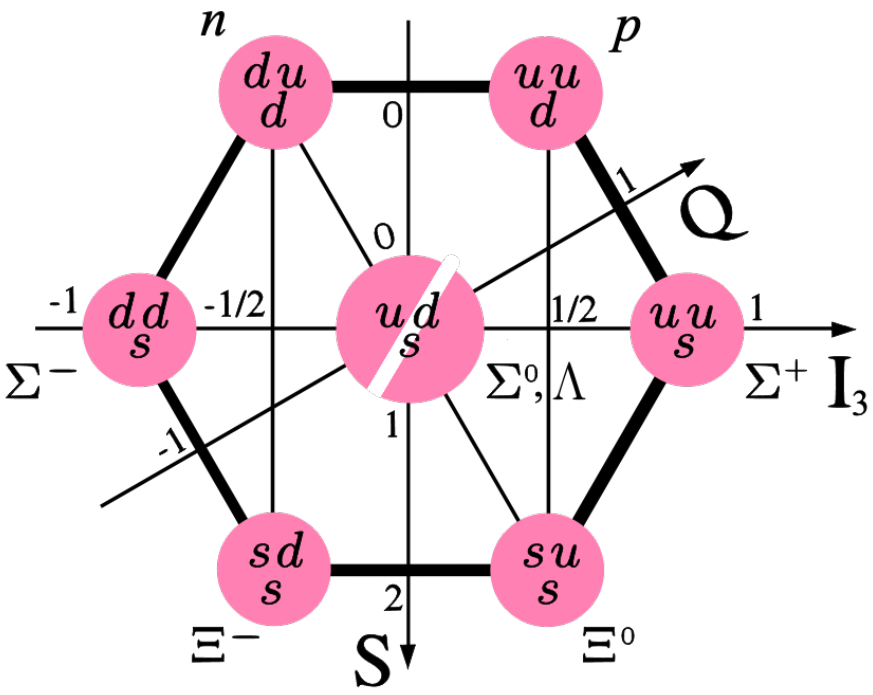

Figure 1.4: A diagram showing the baryon octet in the quark model. The structure of the proton as being made of uud and the neutron as being udd is clearly seen.

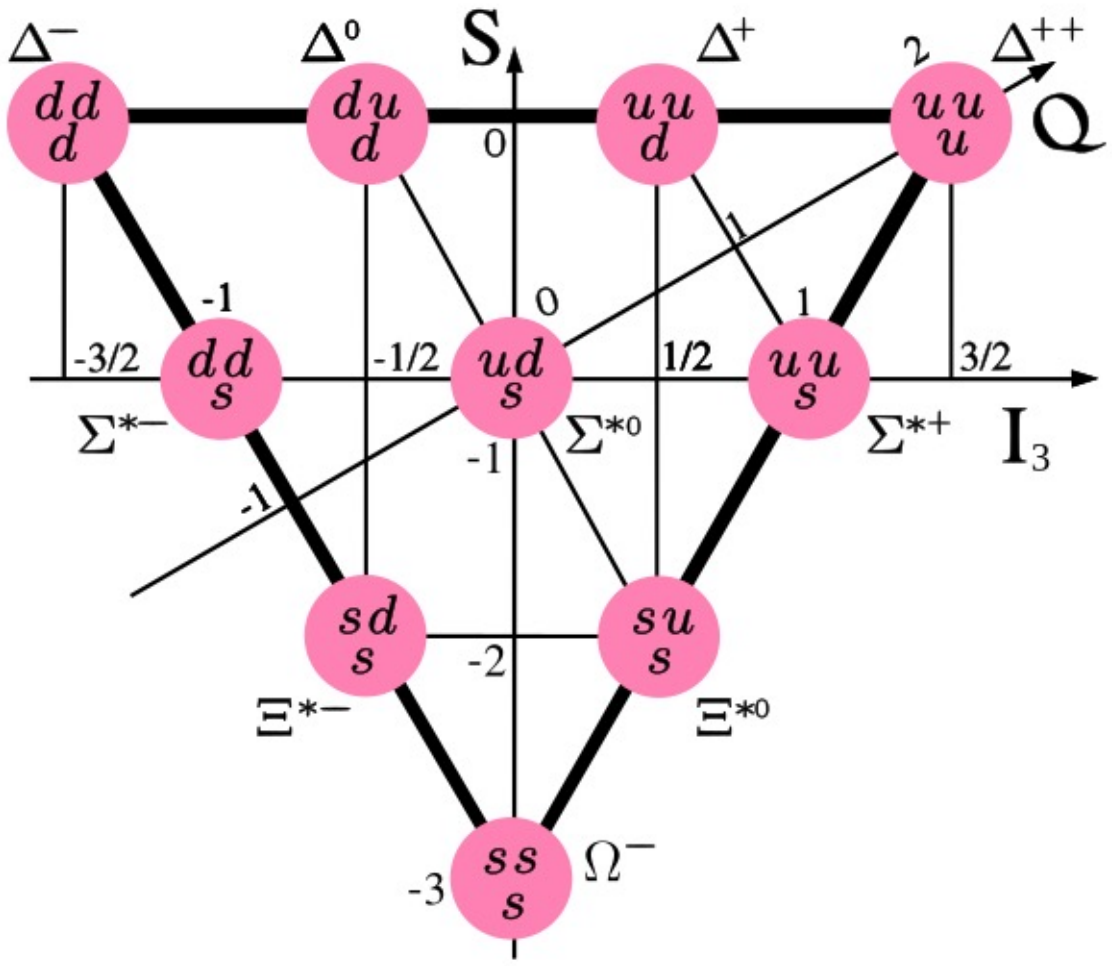

Figure 1.5: A diagram showing the baryon decuplet. This quark model predicts the existence of a particle with strangeness -3, the Ω^-.

state; this meant another quantum number must be present to avoid violating the exclusion principle. Color was able to explain why the quarks bind together to form particles. There are 3 colors red, green, and blue (along with the corresponding anti-colors) and gluons mediate the color force between quarks and all particles must have net zero color. This explained why quarks and glouns could not be observed directly [27].

1.2.3 Putting it all together

The quark theory predicted small constituents of matter inside protons and neutrons based on particle productions observed in the 1960's. The parton theory also predicted small constituents of matter to help explain the cross section in ep collisions. The verification that partons are indeed quarks and glouns came from the observation that in e^+e^- collisions you get a collimated stream of particles which are called jets [28]. If quarks did not make up the proton then you would expect a more homogeneous distribution of particles. The existence of jets verified the quark model and later the observation of a three jet event verified the existence of the gloun [41] [17]. The picture was now complete and partons were recognized as being quarks and glouns and the theory of Quantum Chromodynamics (QCD) became the theory governing the strong force.

One of the most interesting results to come out of the theory of QCD is the running coupling constant of the strong interaction. This means that the interaction of quarks is strongest when they are far apart and weak when they are closest. This means that a quark or gluon can be considered free at short distances. This also becomes important in pp collisions which is what will be discussed next.

1.3 pp collisions

This section will go over the quantities relevant in proton proton (pp) collisions as well as introducing polarized proton collisions and the Transverse Single Spin Asymmetry (TSSA) observable. It will talk about the relevance of TSSA in proton structure, previous measurements and the improvements this work will provide on those previous measurements.

1.3.1 Unpolarized pp collisions

The cross section of unpolarized pp collision where the process is $A + B \to C + X$ is given in eq. 1.4 [20]. This process is shown diagrammatically in fig. 1.6.

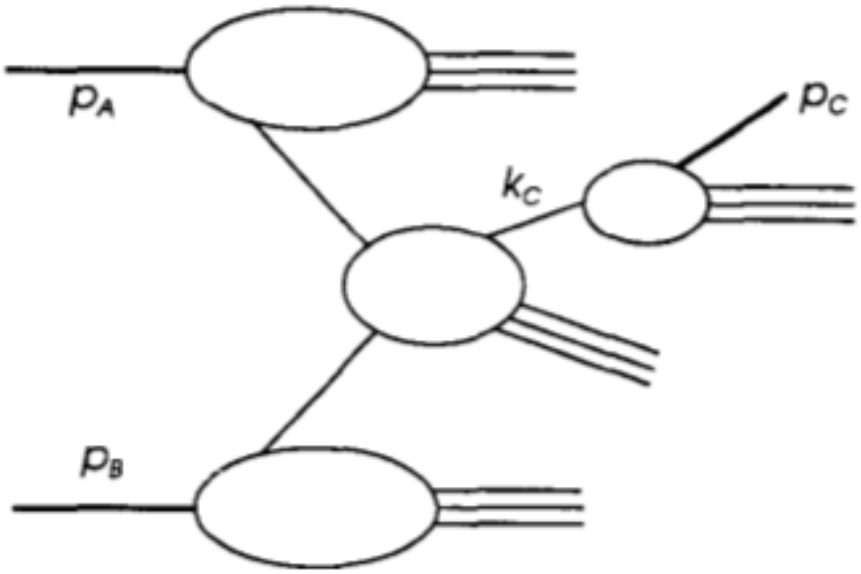

Figure 1.6: Diagram showing unpolarized pp scattering. Here p_A and p_B are the initial momentum of the protons and p_C is the momentum of the scattering parton [20].

$$E_C \frac{d\sigma}{d^3\overrightarrow{p}_C} = \sum_{abc} \int d\xi_A d\xi_B \frac{dz}{z} f_{a/A}(\xi_A) f_{b/B}(\xi_B) |\overrightarrow{k}_C| \frac{d\hat{\sigma}}{d^3\overrightarrow{k}_C} D_{C/c}(z) \tag{1.4}$$

The sum is taken over all flavors of quarks, antiquarks and glouns. The $f_{a/A}$ and $f_{b/B}$ are the PDFs for the initial hadrons. $D_{C/c}(z)$ is the fragmentation function. The hard scattering function $|\overrightarrow{k}_C| \frac{d\hat{\sigma}}{d^3\overrightarrow{k}_C}$ is for the scattering $a + b \to c + X$ at the parton level. The variable z represents the fractional momentum of the measured hadron relative to its parent quark. The ability to write the cross section as a product of the PDF, the hard scattering cross section, and the fragmentation function is known as factorization. This factorization allows one to treat each part of the collision separately. The initial state is the PDF, the hard scattering can be calculated perturbatively, and the fragmentation function describes a parton c turning into a hadron C. This unpolarized case can be extended to include polarization [20].

1.3.2 Polarized $p^{\uparrow}p$ collisions

The cross section of polarized pp collision for the process $A^{\uparrow} + B \to C + X$ is given by eq. 1.5

$$E_C \frac{d\sigma}{d^3\overrightarrow{p}_C} = \sum_{abc} \int d\xi_A d\xi_B \frac{dz}{z} \rho_{\alpha\alpha'} f_{a/A}(\xi_A) f_{b/B}(\xi_B) \times H_{\alpha\alpha'\beta\beta'}(a+b \to c+X) D_{C/c}(z) \tag{1.5}$$

Here H is the hard scattering cross section with the density and decay matrices factored out. $\rho_{\alpha\alpha'}$ is the helicity density matrix of the incoming hadron A [20].

1.3.3 Transverse Single Spin Asymmetry (TSSA)

The TSSA (A_N) is defined as in eq. 1.6. It is a measure of the asymmetry of particle production with respect to the left and right of a transversely polarized proton (see fig. 1.7).

$$A_N = \frac{d\sigma^{\uparrow} - d\sigma^{\downarrow}}{d\sigma^{\uparrow} + d\sigma^{\downarrow}} \tag{1.6}$$

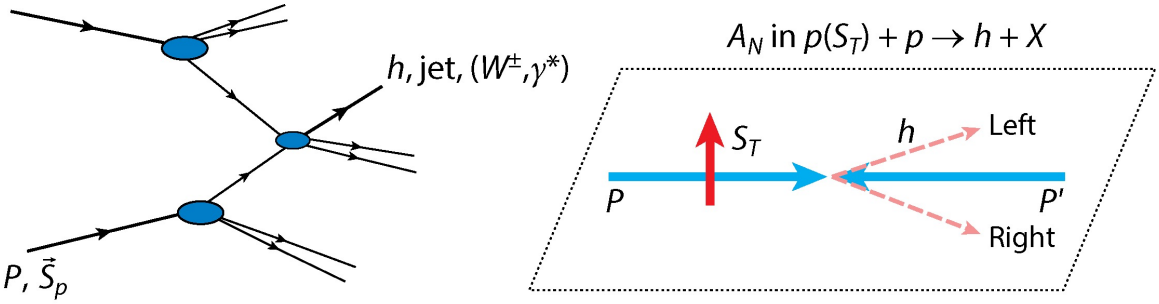

AR Predekamp MG, Yuan F. 2015.
Annu. Rev. Nucl. Part. Sci. 65:429–56

Figure 1.7: Diagram showing nucleon nucleon scattering as well as the meaning of A_N for the case of a transversely polarized nucleon [25].

Calculations in pQCD predict that A_N should disappear as a $\sqrt{s}$ increases for any hadron production [40]. However, this was not the case as can be seen in fig. 1.8, which shows A_N as a function of Feynman-x ($x_F = p_L/p_L^{max}$) for various $\sqrt{s}$ and it is clear that there is no dependence on $\sqrt{s}$. A more recent result for π^0 production at $\sqrt{s} =$ 200 GeV and 500 GeV can be seen in 1.9. Where there is still no $\sqrt{s}$ dependence. This mystery has challenged our understanding of proton structure. One purposed mechanism to explain the large A_N seen in experiments is to add a parton transverse momentum to the

initial PDF for a transversely polarized nucleon. These are called Transverse Momentum Distributions (TMD).

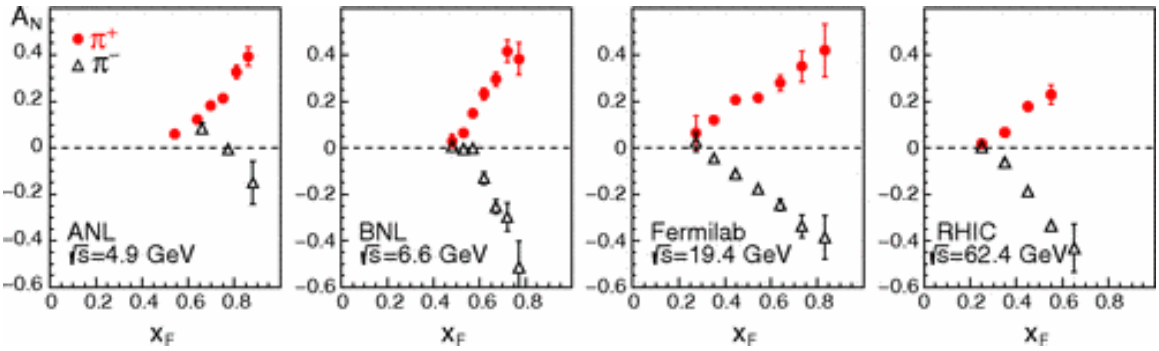

Figure 1.8: TSSA for forward $\pi^{\pm}$ production at various $\sqrt{s}$ [8].

1.4 Outline of this Dissertation

This dissertation has discussed the importance of polarized *pp* collisions and why measuring the TSSA of π^0's are important. The rest of the work for this dissertation was building, testing, commissioning, and running a brand new detector system that will allow us to make much more precise measurements of the TSSA of π^0's than presented before. It will begin with a description of the polarized beam facility at Brookhaven National Lab (BNL). It will then describe the new detector system, how it works and its functionality. Lastly, it will discuss the analysis of the π^0 signal itself and present the results.

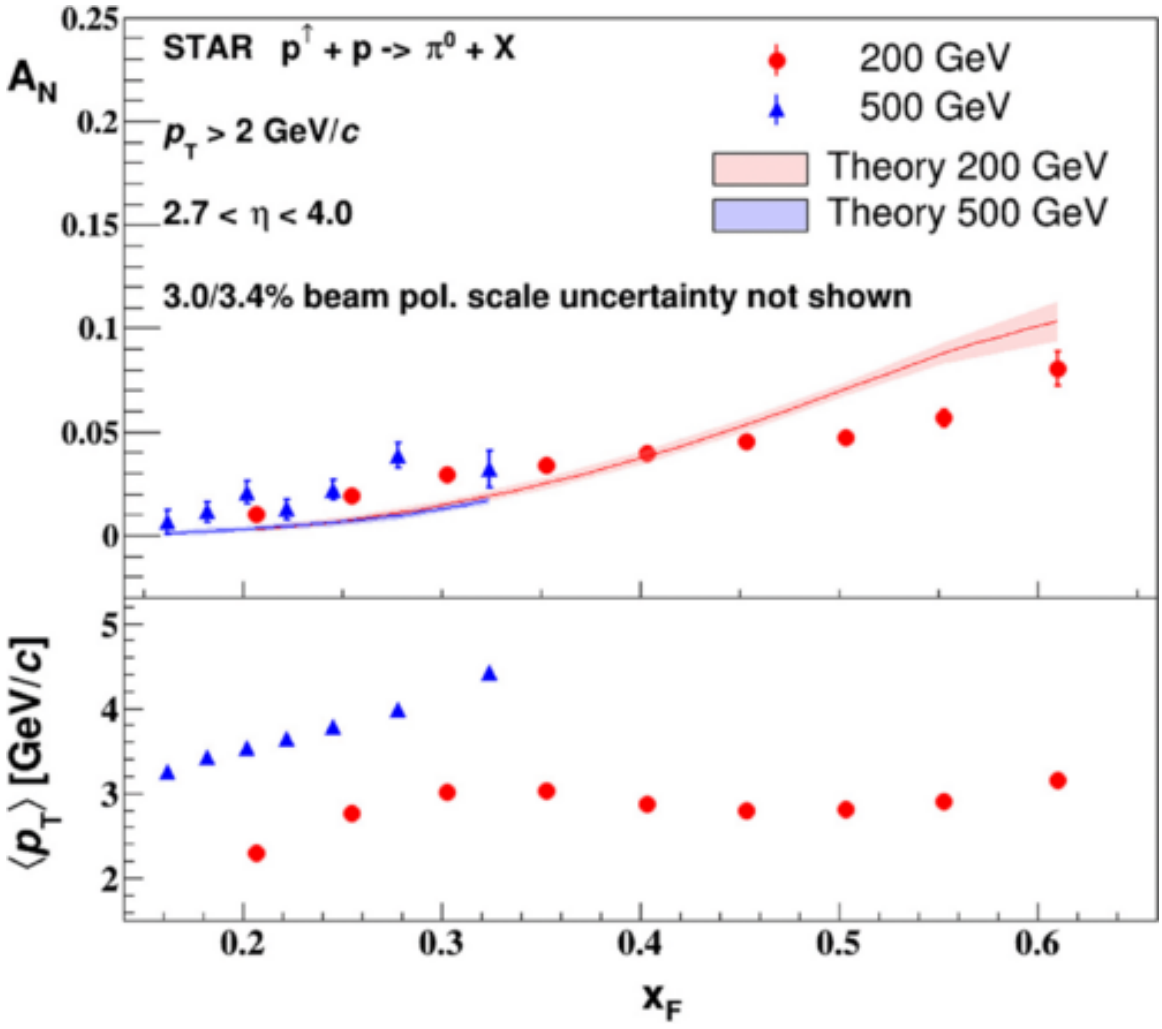

Figure 1.9: TSSA for forward π^0 production at various $\sqrt{s} = 200\ GeV$ and $500\ GeV$ [5].

Chapter 2

Experimental Setup

This work was performed at Brookhaven National Lab (BNL) using the Relativistic Heavy Ion Collider (RHIC)[26] with the Solenoidal Tracker at RHIC (STAR) detector system [4]. Specifically, the Forward Calorimeter System (FCS) system which is a part of the larger STAR forward upgrade (fSTAR)[44][43]. The STAR forward upgrade consists of the FCS and two tracking systems: a silicon strip design called the Forward Silicon Tracker (FST)[18], and a gas chamber design known as small-strip Thin Gap Chamber (sTGC) based on the ATLAS experiment [3]. The FST and sTGC trackers will not be discussed as they were not used in this work. The FCS consists of an electromagnetic calorimeter (Ecal), a Hadronic Calorimeter (Hcal) and a preshower detector (fPRE). This chapter will discuss the RHIC collider, give a brief overview of the STAR detector system, and will end with a description of the FCS subsystem.

2.1 Relativistic Heavy Ion Collider

RHIC is located at BNL and it is currently the only polarized proton proton collider in the world[36]. It is used to generate, maintain, and collide beams of polarized protons used in this analysis. A schematic of RHIC can be found in Fig 2.1. The RHIC collider consists of two polarized proton beams. The polarization of the beams needs to be preserved as they are being accelerated by using Siberian Snakes and is further discussed in Sec. 2.1.4. The polarization is measured using a hydrogen jet target (HJET) and a carbon target (pC). These polarimeters are discussed more in 2.1.5. Figure 2.1 shows the RHIC complex from above with the top of the diagram being North, with the northernmost point of the circle referred to as the 12 o'clock position and is where the polarimeters are located; The 6° clock position is where the STAR detector used in this analysis is located and is discussed more in 2.2. The beam rotating counterclockwise is designated as the yellow beam and the clockwise going beam is designated as the blue beam. The beam is generated from a polarized hydrogen source (OPPIS) and then boosted through a LINAC more in 2.1.1. The LINAC then leads to a booster which further accelerates the beams. The booster leads to the Alternating Gradient Synchrotron (AGS) where there is partial Siberian Snakes to maintain polarization and further accelerate the beams; the booster and AGS are discussed more in 2.1.2. These beams are then passed into the RHIC rings themselves which contains a pair of Siberian Snakes; its design, operation, and performance is described further in 2.1.3.

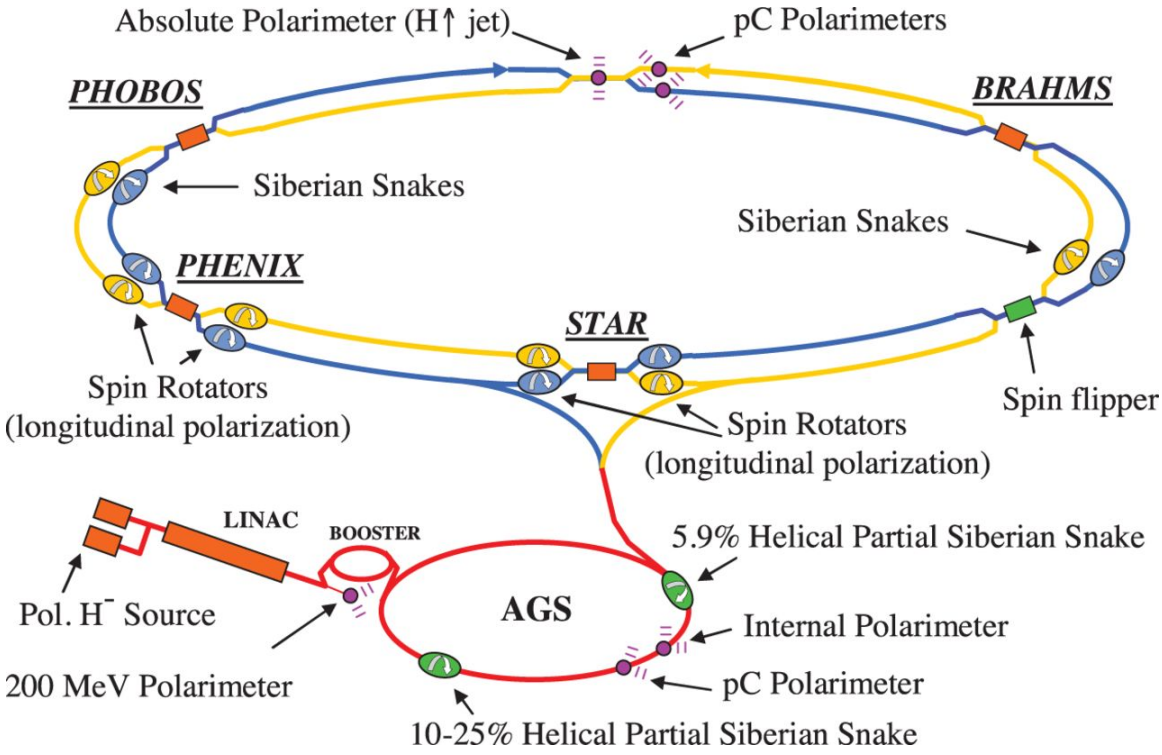

Figure 2.1: This is a diagram showing the various components of RHIC and the relevant components for the generating and maintaining the polarized beams. The protons start about 95% polarized and accelerated in the LINAC. Then they are further accelerated in the Booster and AGS. From the AGS the beams are moved to the RHIC rings and accelerated to the final energy. One beam, designated blue, goes clockwise and the other, designated yellow, goes counterclockwise. The Siberian Snakes are responsible are maintaining the polarization throughout. There are two polarimeters, H↑ jet and pC, which are used to measure the polarization [36].

2.1.1 Polarized Proton Source (OPPIS), LINAC and Booster

To generate a polarized beam of protons RHIC utilizes a technique known as Optically Pumped Polarized Ion Source (OPPIS). This system was constructed at TRIUMF from the KEK OPPIS source. The goal was to provide 0.5 mA of H^- ion current at 80% polarization. In order to achieve a bunch intensity in RHIC of 2×10^{11}, the injection needs to take into account for losses of the beam for transfer to the RHIC line and AGS. This means a bunch intensity of 9×10^{11} is initially injected into the LINAC. The polarized H^- ions are accelerated to 200 MeV in the LINAC and strip-injected and captured into a single bunch in the AGS Booster. The booster will then accelerate the bunches to 1.5 GeV before transferring the beam to the AGS [9] [49][50] [10].

2.1.2 Alternating Gradient Synchrotron (AGS)

The AGS accelerates the polarized protons to 25 GeV. It contains partial Siberian snakes to preserve the polarization in the acceleration process. The snakes are placed strategically to minimize the polarization losses without the need for full Siberian Snakes [45] [9].

2.1.3 RHIC Design

The beams prepared from the LINAC to the AGS are transferred to the RHIC rings. This process of injecting beams into RHIC is what is referred to as a "fill". It varies from fill to fill whether the beams are injected first into yellow beam or the blue beam. However, the procedure is usually to fill one beam and bring it to the collision energy and inject the other beam. Note that this means both beams are polarized. After the beams are

brought to collision energy a polarization measurement is taken with the pC polarimeter and then they are steered into the Interaction Points (IP) located along the RHIC rings. The IP's are where the detectors are located. STAR is sitting at the IP located at the 6 o'clock position on the RHIC rings. In polarized *pp* collisions a fill lasts about 8 hours and a polarization measurement with the pC polarimeters are taken every 4 hours and before the beam is dumped. This constitutes one fill at RHIC [9].

2.1.4 Spin Dynamics and Siberian Snakes

A polarized proton beam will undergo precession of its spin as it is being accelerated. The equation for the decay of the polarization is governed by the Thomas-BMT equation and is shown in eq. 2.1 [9][29].

$$\frac{d\overrightarrow{P}}{dt} = -\left(\frac{e}{\gamma m}\right)\left[G\gamma\overrightarrow{B}_{\perp} + (1+G)\overrightarrow{B}_{\parallel}\right] \times \overrightarrow{P} \tag{2.1}$$

The polarization vector $\overrightarrow{P}$ is expressed in the frame that moves with the particle. $G = 1.7928$ is the anomalous magnetic moment of the proton and $\gamma = E/m$. Furthermore, we can define a quantity called the spin tune $\nu_{sp} = G\gamma$. There are two main sources of depolarizing resonances: imperfect resonances, and intrinsic resonances. The imperfect resonances are coming from magnet errors and misalignments and resonance condition is such that $\nu_{sp} = n$ where n is an integer. Intrinsic resonances occur when $\nu_{sp} = kP \pm v_y$, where k is an integer, and v_y is the vertical betatron tune and P is the periodicity. At the AGS, $P = 12$ and $v_y = 8.8$ [9].

It is in overcoming the effects of these depolarizing resonances that RHIC uses Siberian Snakes [42] [21] [29]. The Siberian Snakes are a set of four superconducting helical dipole magnets which will flip the direction of the spin of the beams in a helical path that looks like a snake. Figure 2.2 shows this path. Constantly flipping the spin in this way helps to get rid of the depolarization resonances because the spin tune ν_{sp} becomes $1/2$ so the condition $\Delta v_y \neq 1/2$ can no longer be met and spins would not decay. However, the presence of strong depolarization resonances over many turns leads to the condition $\Delta v_y = \frac{\nu_{sp} \pm k}{n}$ and are called the snake resonances, where n is the number of turns [9]. This will cause the polarization of the beams to decay over time as you hit these resonances. However by using the Siberian Snakes, over the lifetime of a fill, the polarization will hold.

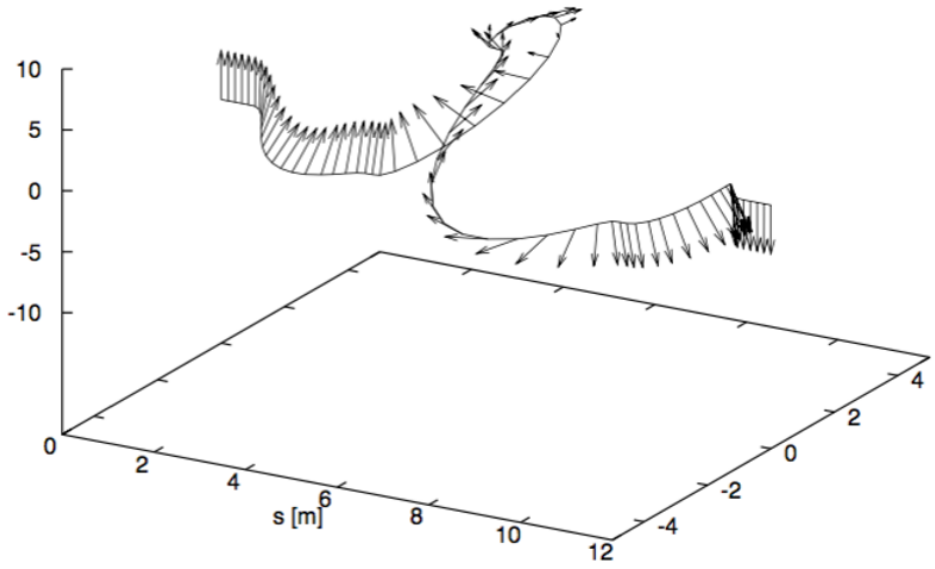

Figure 2.2: This shows the path a polarized proton beam takes in the Siberian Snakes [9].

2.1.5 Measuring the Polarization

The polarization is measured throughout the fill using two polarimeters: a hydrogen jet target (HJet) and a proton carbon target (pC) [33] [9]. The HJet is an absolute polarimeter and takes a long time to measure the polarization. This means that these measurements are taken consistently during the fill. The pC polarimeter takes much faster measurements and measures the profile and lifetime and it also disturbs the beam and thus data taking is halted when the pC makes a measurement. The pC measurement is done at the beginning, middle, and end of a fill and together with the HJet measurement throughout the fill the polarization percentage can be tracked. Fig 2.3 shows the average polarization measurement of the blue and yellow beams over the lifetime of RHIC.

The polarimeters utilize the same TSSA calculation described in section 1.3.3 to measure the beam polarization. The pC polarimeters use a silicon strip setup surrounding a carbon target to count the number of particles scattered left and right of the beams [33]. The HJet polarimeters also utilize an array of silicon detectors placed to the left and right of the beams [35]. Both systems will count the recoil protons to measure A_N and from there extract the polarization.

2.2 STAR Detector

The STAR detector is located at the 6 o'clock position on the RHIC ring. It stands for Solenoidal Tracker At RHIC and is named mostly for the Time Projection Chamber (TPC) [11] that was at the time of the starting of RHIC a brand new way to get 3-D particle

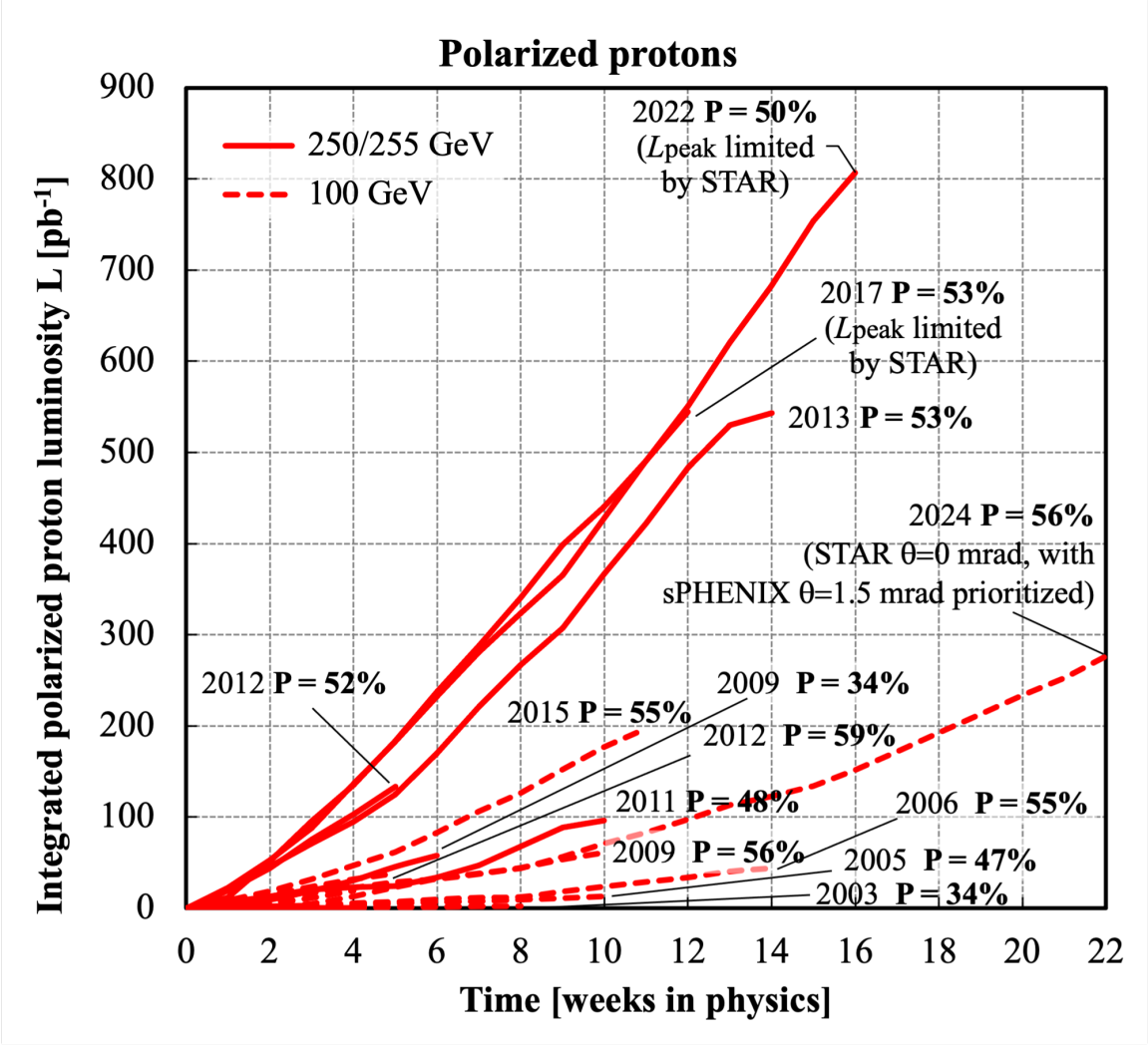

Figure 2.3: Polarization and luminosity measurements for RHIC polarized *pp* running over the years [2].

tracking information. Over the years several more detector systems have been added around the TPC to complement the STAR detector. The TPC covers a pseudorapidity (defined in eq. 2.2, where θ is the polar angle) of $-1.0 \leq \eta \leq 1.0$. The detectors used in this analysis does not include the TPC as this analysis is focused on measuring π^0's in $-2.5 \leq \eta \leq 4.0$, however since the TPC was built around the collision center it helps to know it as a point of reference. The detectors in this region that were used in this analysis include the Beam Beam Counter (BBC) [48], Vertex Position Detector (VPD) [32], Event Plane Detector (EPD) [7], and the Forward Calorimeter System (FCS) [43]. Figure 2.4 shows the relevant STAR detectors and location of where the FCS will go in relation to the rest of STAR.

$$\eta = -ln\left(tan\frac{\theta}{2}\right) \tag{2.2}$$

The BBC, VPD, and EPD are fast trigger detectors on both sides of the TPC and are used for vertex position determination in this analysis, their details can be found in 2.2.1. The FCS consists of a scintillator hodoscope preshower (fPre), an electromagnetic calorimeter (Ecal), and a hadronic calorimeter (Hcal), the details of which are discussed in 2.2.2. The FCS was part of a larger forward upgrade to STAR which consists of silicon strip sensors, and small-strip thin gap chambers for tracking. However, since they were not used in this analysis and they will not be discussed.

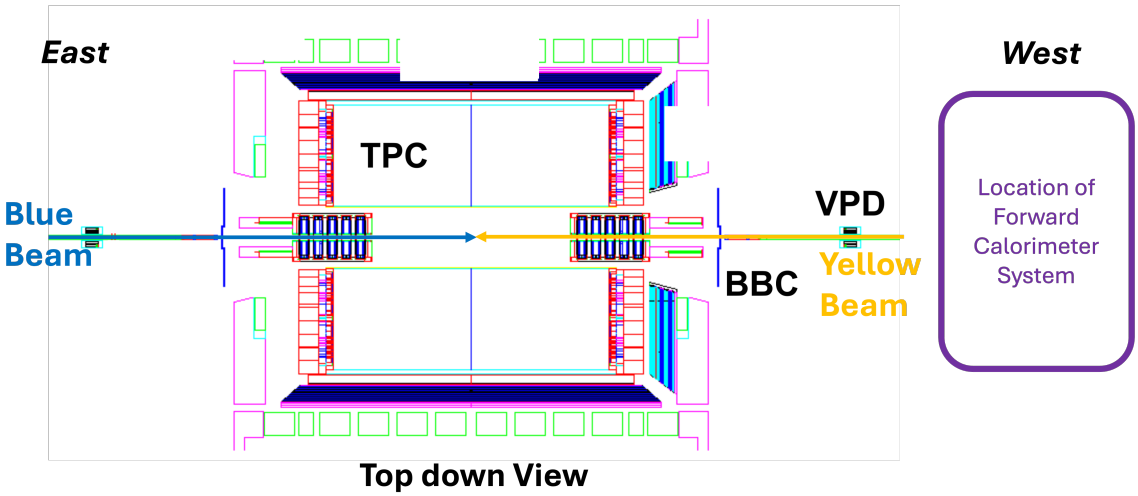

Figure 2.4: Top down view of STAR detector showing the TPC, BBC, and VPD as well the RHIC beam directions and location of FCS.

2.2.1 Global Detectors

- The Beam-Beam Counter (BBC) is a scintillator hodoscope that consists of hexagonal tiles which covered a region $3 \leq |\eta| \leq 5$ in Run-22 [1]. It used PMTs for readout. They were located at $\pm$ 200 cm of the STAR main collision point [48].

- The Vertex Position Detector (VPD) is a PMT based scintillator counter detector located further out in STAR. It covers a pseudorapidity range $4.24 \leq |\eta| \leq 5.1$ [32].

- The Event Plane Detector (EPD) is a scintillator hodoscope with SiPM readout. It is located near the BBC [7]. More details on this will be covered in section 2.2.2.3 as it was also integrated into the FCS as a preshower detector.

[1] After the EPD was installed in Run 19 the coverage of the BBC shrank as its outer tiles were replaced by the EPD

2.2.2 Forward Calorimeter System

The FCS consists of a scintillator hodoscope preshower detector (fPre – discussed in section 2.2.2.3), an electromagnetic calorimeter (Ecal – discussed in section 2.2.2.1), and a hadronic calorimeter (Hcal – discussed in section 2.2.2.2).

2.2.2.1 FCS Electromagnetic Calorimter (Ecal)

An electromagnetic calorimeter is designed to ensure that photons, electrons, and positrons deposit all or most of their energy by inducing what are called electromagnetic showers. Electromagnetic showers induced by these particles have very similar characteristics and so are oftentimes called electromagnetic particles. In fact, it is this kind of similarity that makes them hard to distinguish in an electromagnetic calorimeter.

The electromagnetic calorimeter in the FCS is the repurposed PHENIX lead (Pb) scintilator (Sc) sampling (Shashlyk) calorimeter [13]. The FCS Ecal can be seen Fig 2.5. It is located about 7 m away from the main STAR IP. A single tower module consists of 66 layers of PbSc pairings where the Pb has a thickness of 0.015 cm and the Sc a thickness of 0.4 cm making up for a total length of about 31 cm or 18 radiation lengths (X_0). Additionally, each tower has a transverse size of 5.25 cm by 5.25 cm. WaveLenghth Shifting (WLS) fibers are embedded into the layers of a tower and are used for light collection; they are of type BCF-99-29a and 0.1 cm in diameter. The PHENIX design used a PhotoMultiplier Tube (PMT) readout so the design had to be modified to use a Silicon Photomultiplier (SiPM) readout because they are insensitive to magnetic fields made relevant by the fact that the FCS is placed near one of the RHIC magnets, use low voltage which simplifies

operation, somewhat "radiation hard", and as technology improves cheaper than PMTs; for these reasons the design was chosen to be modified to use SiPMs. The modification was accomplished by gluing small rectangular acrylic light guides to the bundled WLS fibers for each tower. Four SiPMs (type Hamamtsu S12572-015P) and a thermistor to keep track of temperature of SiPMs are attached to a printed circuit board (PCB) and glued to each light guide. The signal from one a single tower from these four SiPMs are also referred to as a channel and towers and channels are used interchangeably in this document. There are 1496 channels in total.

The towers are further organized into supersectors where one supersector is a 2 by 2 grouping of towers; one supersector can be seen in Fig 2.6. Each supersector has a Front End Electronics (FEE) board attached to the SiPMs using pogo pins on the front side of the tower (facing towards the STAR interaction point). This results in each FEE processing signals from 4 towers. The signal from each FEE is routed to a DEP board which handles digitization and triggering. This process is discussed in more detail in 3.2.

The Ecal is placed on the West platform at STAR which is also the blue beam going direction. The platform and thus the detector is separated into two halves, one on each side of the beam pipe; note that this means that the region above and below the beam pipe is not covered however the asymmetry is expected to be zero in this region. One half is designated North and the other designated South; the designation chosen because it is where the detectors are located in accordance with the 4 cardinal directions. The designation of West platform is used for the same reason. The two halves are tilted at an angle of 1.73° with respect to the beam direction; this was done to make them face the interaction point

at the center of STAR more directly. There are 34 rows and 22 columns of towers in each half. They are placed on movable rails on the platform so that it can be moved to access its components for maintenance reasons.

In addition a Light Emitting Diode (LED) system was installed on the back side of each half of the Ecal, which can be seen in 2.7. The LEDs were placed on PCBs (as shown in 2.8) and distributed at regular intervals on the back side of the Ecal. A tower by tower LED system was not needed because the LEDs were shone on an aluminum backing which would reflect and disperse the light evenly to all the loops of WLS fibers at the back of the towers. The LEDs are blue MULTICOMP OVL-5523 LEDs. The LED system was used to test the integrity of the system. In addition, the LEDs are used to check the gain of the channels over time as well as determine the performance of the channels. If a channel is not behaving as expected it is easily seen in the LED data. The LED data is typically taken once a day. In addition to LED data, the FEE boards can read the current in the SiPMs. The current is monitored to understand the channel health as well as used to adjust the gains to compensate for radiation damage.

2.2.2.2 FCS Hadronic Calorimeter (Hcal)

A hadronic calorimeter works on the same principle as an electromagnetic calorimeter in that it induces electromagnetic showers but because its purpose is to make hadrons shower, the shower development works differently. In order for a shower to develop the hadron needs to have a nuclear interaction with the calorimeter material. This nuclear

Figure 2.5: A picture of the front view of the FCS Ecal.

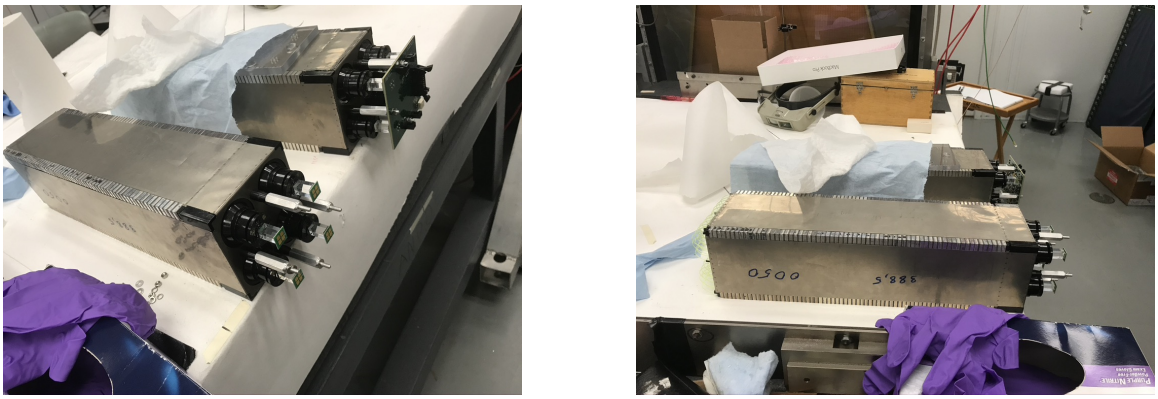

(a) Front View (b) Side View

Figure 2.6: An image of a super sector in the Ecal (2x2 grouping of towers).

interaction will then create the photons needed for an electromagnetic shower to occur. For this reason hadronic calorimeters are typically denser and longer than electromagnetic ones because it takes nuclear interactions to stop hadrons, which given the size of nuclei requires lots of dense material where atomic nuclei are much closer together.

The Hcal is also a sampling calorimeter placed downstream (i.e. behind) from the Ecal. It is also made up of towers that consist of steel (Fe – symbol for iron but used to represent steel) and scintillator (Sc) plates. There are 36 pairings of FeSc. The transverse size of Fe and Sc plates are 10 cm by 10 cm. Note that this means one Hcal tower covers roughly one supersector of the Ecal and chosen by design since showers in the Hcal will cover more area than in the Ecal. The steel plates are 2 cm thick and the scintillators are 0.3 cm thick. Additionally there is an air gap of 0.34 cm between the Sc and Fe absorber. This results in a total length of about 84.2 cm or 4.5 hadronic interaction lengths (λ). There are a total of 520 channels split into a North half and a South half – like the Ecal – and

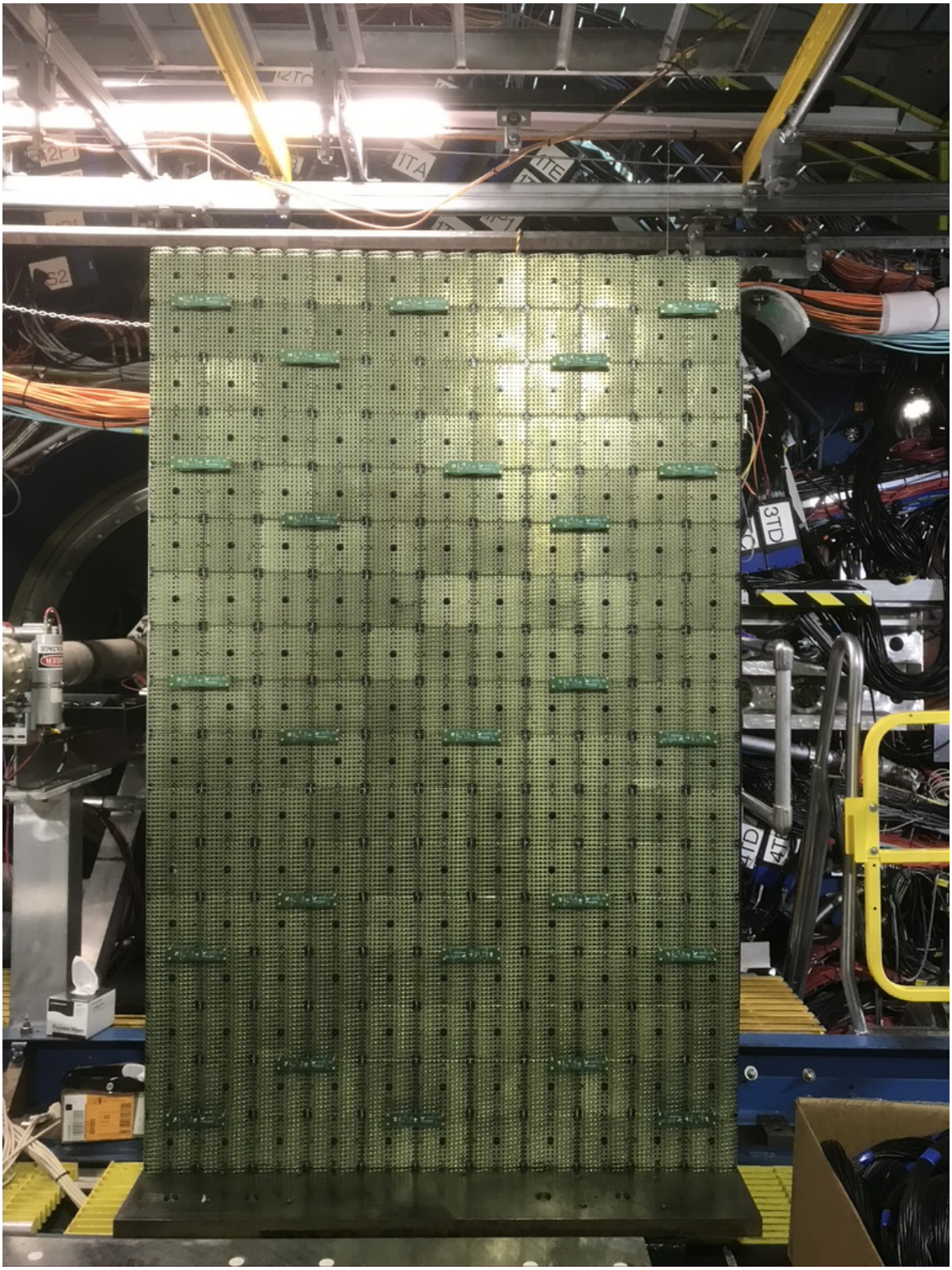

Figure 2.7: An image of the backside of the Ecal showing the LED system.

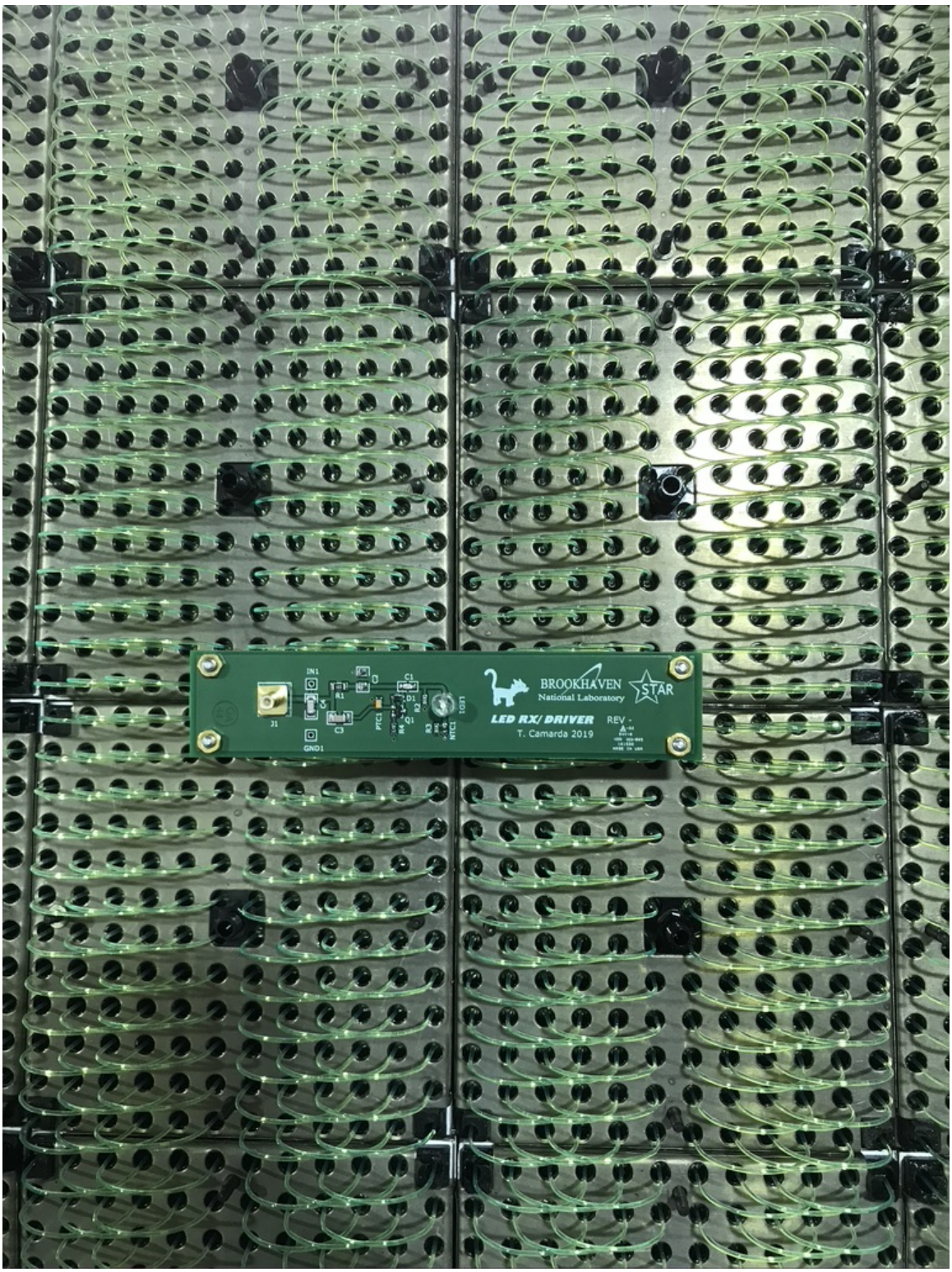

Figure 2.8: An image of the Ecal LED board.

angled in the same way so that it is parallel to the back of the Ecal. Each half consists of 20 rows and 13 columns of towers so 260 channels per half.

The Sc tiles were painted on the top and bottom edges with white diffusive paint and polished on the other two edges. The light from the scintillation tiles for a single tower was collected by tapered 0.29 cm thick WLS bar (EJ-280). It was placed along the length of the tower with a small air gap between the Sc plates and itself. One end of the WLS bar is tapered to better concentrate light on the SiPMs, because there was no space for an additional light guide and to help with uniformity of light collection along the tower. The other end of the WLS bar was painted with white diffusive paint to prevent light leakage. A graduated reflector made of Tyvek is placed between subsequent towers and acts as both an optical and physical separator between them; additionally it helped to improve uniformity of light collection along the tile. The light from the WLS bar was collected by gluing a PCB, containing six SiPMs (same ones as Ecal) and a thermistor, onto the WLS bar. Additionally the PCBs have a short cable ($\sim$3 cm) that is used to attach the PCB to the FEE board. A single FEE board was connected to two PCBs; i.e. two towers. The design of the Hcal FEE boards are identical to the Ecal ones except for this difference between number of channels.

Hcal also had an LED system in place like the Ecal and was used in the same manner and for the same reasons.

2.2.2.3 FCS Preshower (fPre)

A preshower detector is intended to register signals for particles before they begin to generate electromagnetic showers. The preshower is a scintillator hodoscope. A hodoscope is a detector that is used to get charged particle position information. Scintillators

are ideal for this scenario as they produce scintillation light when charged particles pass through it. Note that this means neutral particles e.g. photons don't produce scintillation light. For this reason, preshowers are installed to distinguish the charged particle showers from neutral particle showers in the electromagnetic calorimeter. The process by which charged particles deposit this energy is called ionization and this energy loss mechanism has a minimum. Particles that exhibit this minimum energy loss are called Minimum Ionizing Particles (MIP)s. MIPs can also occur in the Ecal and Hcal if the charged particle does not shower. The MIP is a fixed amount of energy loss by any charged particle and is determined by the detector material only. The fixed energy loss generates a very specific amount of light by the scintillator material. This results in a peak in the signal distribution above the noise level. This MIP peak position above the noise is determined by the gain in the electronics. Therefore the more charged particles that pass through the scintillator the greater the light output and therefore the greater the signal. See Fig 2.11. Since the energy deposition of MIPs are so consistent they will form multiple peaks at distances equal to the gain. In the EPD a quantity called "nMIP" signifies the energy loss of a "n" particles, meaning if $nMIP = 1$ a single MIP energy deposition happened i.e. one particle; $nMIP = 2$ means two particles, etc. An nMIP near zero signifies noise.

Sampling calorimeters – like the Ecal and Hcal – work will use this principle; so EM showers, initiated by the absorber plates, will generate many charged particles. The higher the energy of the particle showering the more charged particles and therefore more light. However, because not all light is captured by the scintillators sampling calorimeters have a sampling fraction to compensate for this energy loss to light yield output. This

scintillation light can be collected using photodetectors. Typical photodetectors in particle physics today are PhotoMultiplier Tubes (PMT) or Silicon Photomultipliers (SiPM).

The preshower used in the FCS system is the EPD detector refitted with new electronics to split the SiPM signal from the EPD. However, since the FCS is on the West platform only the West EPD was used. The overall EPD geometry can be seen in 2.9 and this is on both the East and West sides of STAR. The EPD is broken up into supersectors that contain 15 tiles each and can be seen in 2.10. The supersectors contain a bundle of fiber optic cables to carry the light from the tiles to a light tight box with SiPMs and FEEs. This was done to reduce the radiation damage to the SiPMs. It is the output of this box that was redirected to the FCS DEP system.

In addition, because the Ecal and Hcal do not cover above and below the beam pipe, these corresponding EPD supersectors were excluded from the signal; for more details see 2.2.2.1 and 2.2.2.2. This splitter was necessary to match the rest of the electronics system of the Ecal and Hcal, which differed from the existing EPD electronics; for more details on the electronics of the FCS see 2.2.3.

2.2.3 FCS Electronics

A whole new electronics scheme was developed to collect, store, and analyze the signals from the FCS detectors. The following sections explain this scheme from the source of the signal (the SiPMs) to the data collection, analysis, and trigger modules (DEP boards).

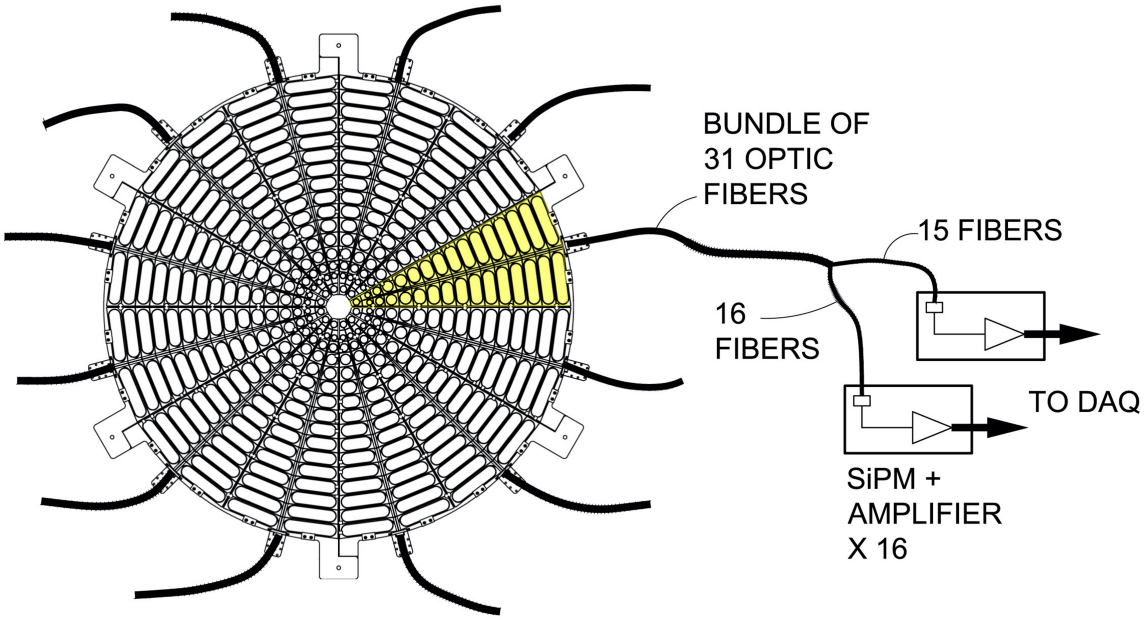

Figure 2.9: A diagram showing the full EPD detector on one side of STAR. It is a scintillator hodoscope utilizing SiPM readout [7].

2.2.3.1 Signal from SiPM

SiPMs are becoming more common in nuclear physics today because of their low voltage, low cost (compared to PMTs), and size, as well as their imperviousness to magnetic fields; which is important as the FCS system was in close proximity to stray magnetic fields from RHIC and STAR magnets. They do however suffer from radiation damage. A PMT operates using the same principle behind the photoelectric effect. Light emitted from the calorimeter material will hit a photosensitive material on the front of a PMT which releases an electron. The electron is pulled towards a high voltage plate (dynode) and upon contact will release more electrons which will be pulled by the next dynode. After many dynodes the single electron signal is amplified and read out the back of the PMT. In order to accelerate the electrons to sufficient speeds to create these cascades a PMT needs

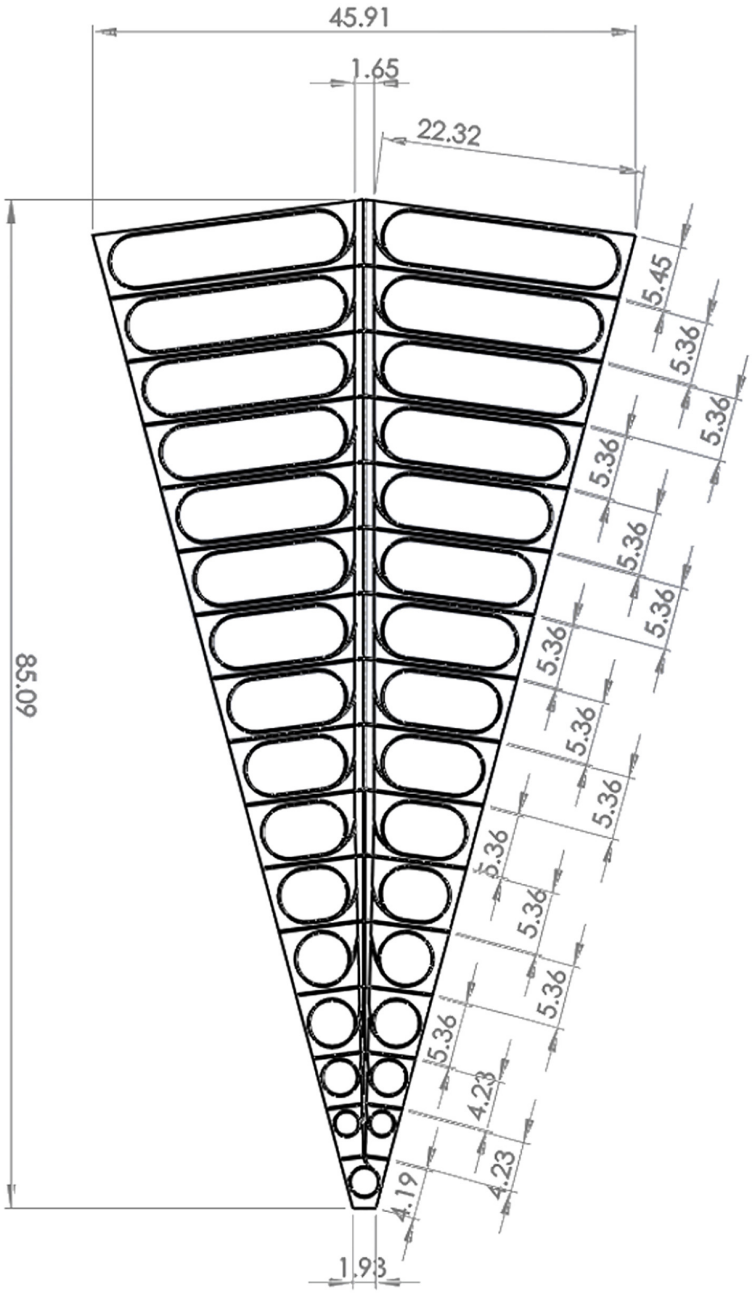

Figure 2.10: A diagram showing one supersector of the EPD detector. It contains 15 scintillator tiles whose light output is carried out with a single fiber optic cable.[7].

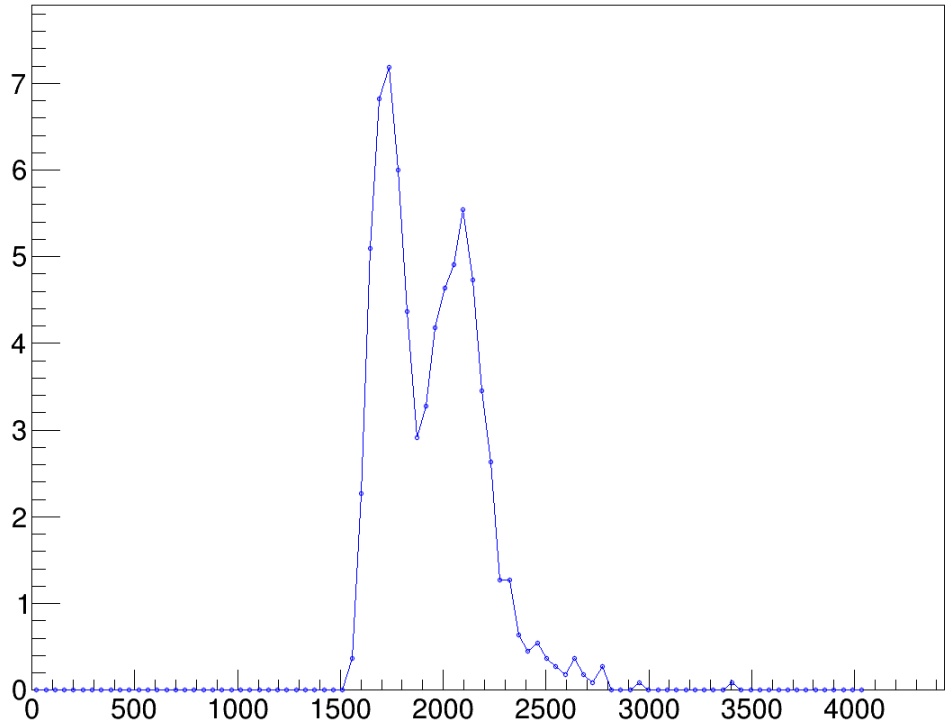

Figure 2.11: A histogram showing the pedestal and MIP peak from some data. The pedestal is the peak located at 1700 ADC and the MIP peak is located at 2150 ADC. The separation between the MIP peak and pedestal is the gain.

to operate at hundreds of Volts. The operating principle of the SiPM is slightly different but understanding the PMT mechanism is useful in understanding the goal and working principle of a SiPM.

The SiPM also works via a cascade of electrons utilizing an effect similar to the photoelectric effect. In this case, when a photon strikes the semi-conductor material, the electrons are excited from the valence band to the conduction band of a semi-conductor material, causing a similar avalanche. The resulting avalanche is results in a measurable current in the device.

To understand how this works we start with a discussion of diodes because a SiPM when no light is present acts like a diode as can be seen in the fig. 2.12. Semi-conductor diodes are made by combining P-type semiconductors with N-type semiconductors. The P-type and N-type semiconductors have different Fermi levels based on their manufacturing. The combination of the P- and N-type semiconductors, at equilibrium, is such that there is no exchange of electron-hole pairs in the material (i.e. no current flow). This means that the Fermi level is situated at a constant level between the Fermi levels of the P- and N-type semiconductors, furthermore this creates a step in the energy band of the resulting material. Applying a voltage on this PN junction such that the positive terminal is connected to the P-type material (negative terminal on N-type) allows current to flow by reducing the energy required for holes to flow from the P-type to the N-type (electrons to flow from the N-type to the P-type). This is called forward bias. Reverse bias is the opposite of this when the negative terminal is connected to the P-type semiconductor. In this case the energy required for holes to flow is increased thus preventing current from flowing. This behavior

only works within a set voltage range because at some point the voltage applied (either forward or reverse bias) becomes so great that the PN junction breaks down and current flows anyway. In forward bias, this is positive current; in reverse bias this is negative current. This behavior can be seen in fig. 2.12 where the middle region is the normal functioning of a diode and as the voltage becomes too great (at either end) current begins to flow and the diode breaks down [46] [31].

The SiPM voltage is set to operate in the forward region where current is expected to be small. The minimum voltage at which current flows is called the breakdown voltage (V_{BD}). In this way when the photon strikes the SiPM it causes the formation of electron hole pairs allowing current to flow; just like a switch closing as shown in fig. 2.13, this device is also called an avalanche photodiode (APD). A SiPM is made up of many APDs as is shown in fig. 2.14 which form the "microcells". Once the photon hits the SiPM the current has a distinct response as shown in fig. 2.15. It is this current which is processed and shaped by front end electronics attached to the SiPM [37].

The SiPMs on the FCS are attached to the PCBs which we call the SiPM board. These SiPM boards also contain a thermistor for reading the temperature. In the case of the Ecal there are 4 SiPMs per board and they are arranged in a 2x2 pattern to capture as much of the light as possible and to match the shape of the light guides. The Hcal SiPM boards also have a thermistor and 6 SiPMs per board to maximize the amount of light captured. These boards can be seen in 2.16 for the Ecal and 2.17. The SiPM boards for the preshower are the same ones as used for the EPD and are described in this paper [7].

2.2.3.2 Front End Electronics (FEE)

The Front End Electronics (FEE) boards are next in line for the signal collection. The FEE boards are responsible for setting the bias voltage on the SiPMs, reading the current and voltage from the SiPM boards, and shaping the signal from the SiPM to fit inside of the time window for a RHIC beam crossing.

Signal processing on the FEE boards consists of a 16 Ω load resistor, a passive pulse shaper, a programmable (CMOS-switched) attenuator for gain control, and a 50 Ω input amplifier, shaper, and cable driver circuit. The signal from the FEE board is carried with differential pair cables to match the interface of the DEP boards. This design saves a lot of cable tray space and makes installation and maintenance efforts much easier.

The programmable gain control in the FCS FEE boards are a feature to relate precisely the normal operating gain of the readout (with full scale 180 GeV) to an approximately 5$\times$ higher gain that suffices to measure the response to vertical cosmic rays in the installed detector for calibration purposes. It is expected to provide less than 1% uncertainty on relative gain, after calibration.

The SiPM bias voltage is regulated independently on each channel using an on-board precision regulator with a 14-bit control Digital to Analog Converter (DAC) that has a voltage range of 0 to 70 V. The regulator sharply limits current to about 800 μA to protect the SiPMs, but below the current limit the output impedance is less than 150 Ω over all relevant frequencies. The noise of the regulated bias voltage is less than 1 mV.

Temperature compensation is provided for each channel, based on that channel's thermistor on the SiPM board; the temperature compensation slope is set in common for

all channels by a 12-bit DAC with a range of 0 to 66 mV/°C. The bias voltage regulator works from an external 80 V input that does not require precision regulation.

The current to each SiPM board is monitored and multiplexed to a 16-bit ADC, with a range of 0 to 410 μA (in the HCAL, 0 to 614 μA). Without calibration, the absolute accuracy of the bias voltage and current monitor are each 1-2%. This was calibrated in a production test so that it could be used in online controls and monitoring in the FCS.

The design for the Ecal and Hcal FEE boards are identical except for two main features. One is that the Ecal FEE boards attach to 4 towers in a 2x2 pattern and use spring-loaded contact pogo pins to attach to the SiPM board. The Hcal FEE board is a two-tower board and connects to its pair of SiPMs by short ($\sim$3 cm) cables. The second is that the gain is set slightly differently between the two boards. The Ecal FEE board can be seen in fig. 2.16 and the Hcal FEE board is shown in fig. 2.18. The FEE boards for the preshower are the same ones as used for the EPD and are described in this paper [7].

The slow controls interface to the FEE board utilizes I^2C, an industry standard, though one which is usually deployed only within a single board or box. It's feasibility at large scale was tested in the 2017 ECAL FEE board and proven to work in the EPD. This design allows 16 FEE boards to share a common control bus, which is just another PCB (see fig. 2.19), using an addressable bridge chip on the FEE. The controls master is integrated into the DEP board, and the connections are made using the same cables that were already needed for signals to the DEP and to power the FEE board. The master interface on the DEP is opto-isolated to avoid problems from electromagnetic interference or ground voltage differences. Each FEE board has a serial number chip which can be

read and used for calibration lookup, although it is not used for addressing; such "1-wire" controls proved to be too slow.

This signal from the FEE board can be seen in fig. 2.22. It is a plot of the response vs. time (ns) from a SiPM using LED pulses. The signal is about 100 ns wide and follows a Gaussian distribution with a distinct tail. The tail is an artifact of the electronics and is not part of the light signal output; integrating this tail will alter the measured energy of the particle. It is one of the sources that need to be eliminated when computing the energy. This signal is time integrated and analyzed by the DEP boards and will lose some of the fine structure due to the sampling of the DEP boards (discussed in section 2.2.4) but the tail will remain and needs to be corrected for when looking at the digitized data from the DEP boards. The next step in the chain.

2.2.4 Detector Electronics Platform (DEP) boards

The Detector Electronics Platform (DEP) board (or DEP32ADC) is a custom multi-channel waveform digitizer designed by the STAR electronics group at BNL in 2019. It's purpose was to provide a reliable multi-channel fast digitizer for calorimeters used in nuclear particle experiments. It's purpose was to replace the VME style crates (commonly used at STAR) to have similar features and be expandable like NIM and CAMAC standards. The FCS marks the first use of such boards at STAR as they were a part of the fSTAR upgrade.

The crate for the DEP boards has a custom backplane with a form factor of 7 rack units (RU) with a PCIe connector and supports 20 DEP boards. The DEP boards are 6 RU high and 220 mm wide and contain digitizers for up to 32 channels. Thus each crate can

Table 2.1: Table detailing the properties of the DEP boards.

Parameter	Value	Comments
ADC	12 bit Sampling ADC	AD9637, 8 channel
Input Range	0-1.8 V peak-peak	full range
Bandwidth	40 MHz	
Sampling Rate	80 MS/s	
Dynamic Range	72 dB	
Conversion Non-linearity	<1 least significant bit	covers full conversion range
Signal to Noise Ratio	>80 dB	signal to noise with low pass filter
Input vs. Output Non-Linearity Gain	<0.1%	
Form Factor	6 RU x 220 mm	

handle a total of 640 channels. Figure 2.20 shows some DEP boards installed in the crate. The DEP input requires differential signaling, which was used to reduce the cable bulk and mitigate ground referenced noise. More details about the DEP boards can be seen in table 2.1 and a functional block diagram that outlines the signal path can be seen in fig. 2.21. The DEP boards versatility allow them to be used for digitization and triggering by taking the output of one DEP board and connecting it to the input of another.

One important aspect of the DEP board in table 2.1 is that it is an 8 channel digitizer. This means that the input signal is digitized into 8 ADC values over one clock tick (one clock tick at RHIC is 127 ns). These 8 samples in time (timebin (tb)) make it possible to more effectively reconstruct the energy by disentangling effects coming from overlapping signals earlier and later in time than the triggered RHIC crossing. This is discussed more in appendix A.

An actual sample LED signal from the whole detector system is shown fig. 2.23. The LED data is taken such that the tb for the pulse resides at approximately 211. In

physics data, the tb that corresponds to the triggered crossing resides at 50 during normal data taking. However, in real physics data, the DEP boards will ultimately keep information from 0-100 tb. This is what allows us to disentangle the effect of the tail on the energy calculation in post-processing of the data. All data recorded is pedestal subtracted. The details of how the tail is excluded from the energy calculations is discussed in appendix A.

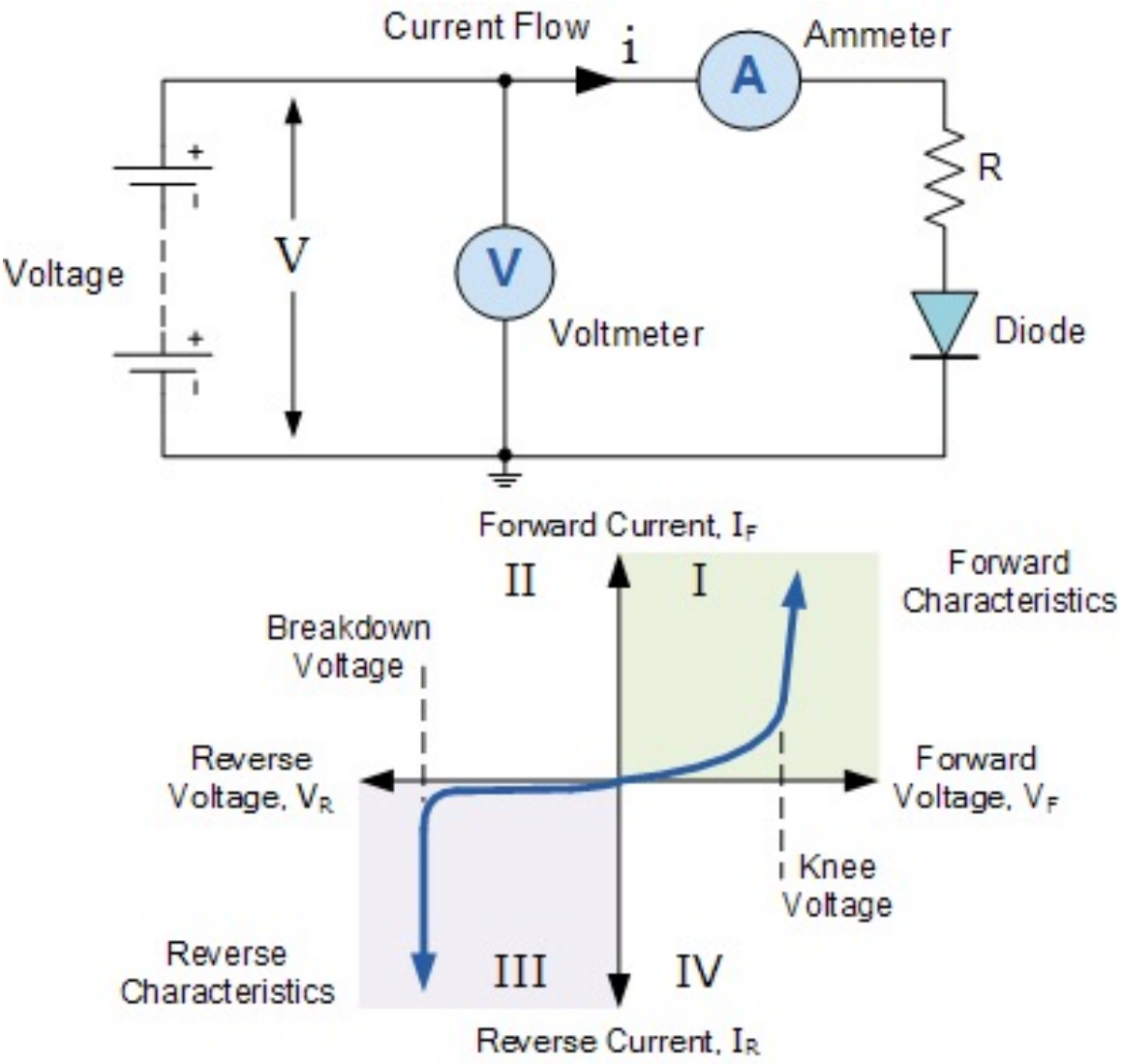

Figure 2.12: A plot showing the characteristic IV regions of a diode as well as a circuit diagram showing a diode as a circuit element how the IV curve is measured. When no light hits the SiPM it acts like a diode. [1]

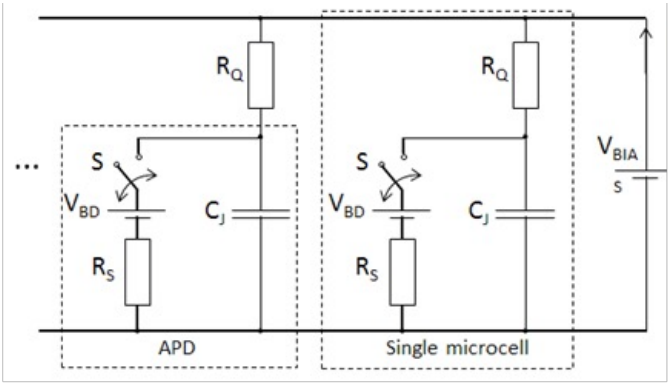

Figure 2.13: A schematic showing the circuit diagram of a SiPM. The APD and microcell components of the circuit are shown. When a photon strikes the SiPM surface the switch closes this creates an avalanche of electrons thus current begins to flow [37].

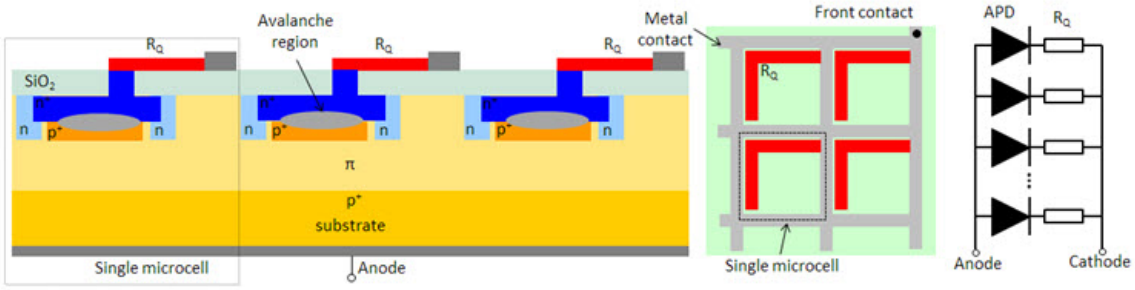

Figure 2.14: A diagram showing the internal components of a SiPM and the PN junctions therein from the top and side. Also shown is how they translate to the APD sites and diode functionality [37].

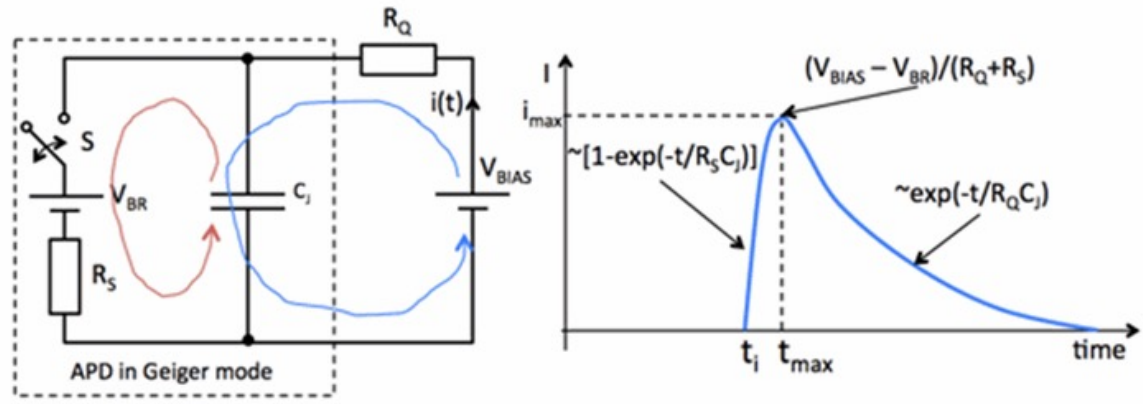

Figure 2.15: A schematic showing how the response of the circuit correlates to the current generated from a single microcell over time. It begins with a large spike followed by an exponential decay [37].

(a) A picture of the SiPM board attached to the FCS Ecal light guides. Each light guide has 4 SiPMs.

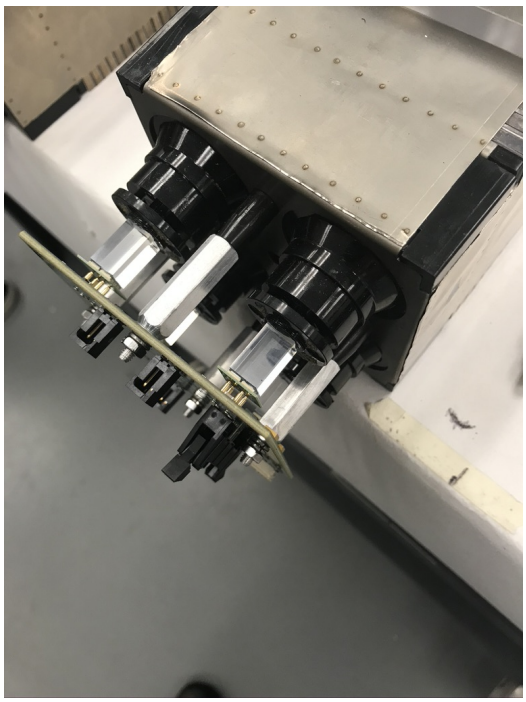

(b) Top view showing how SiPM board connects to FEE card with pogo pins.

Figure 2.16: Various views of the FCS Ecal SiPM boards.

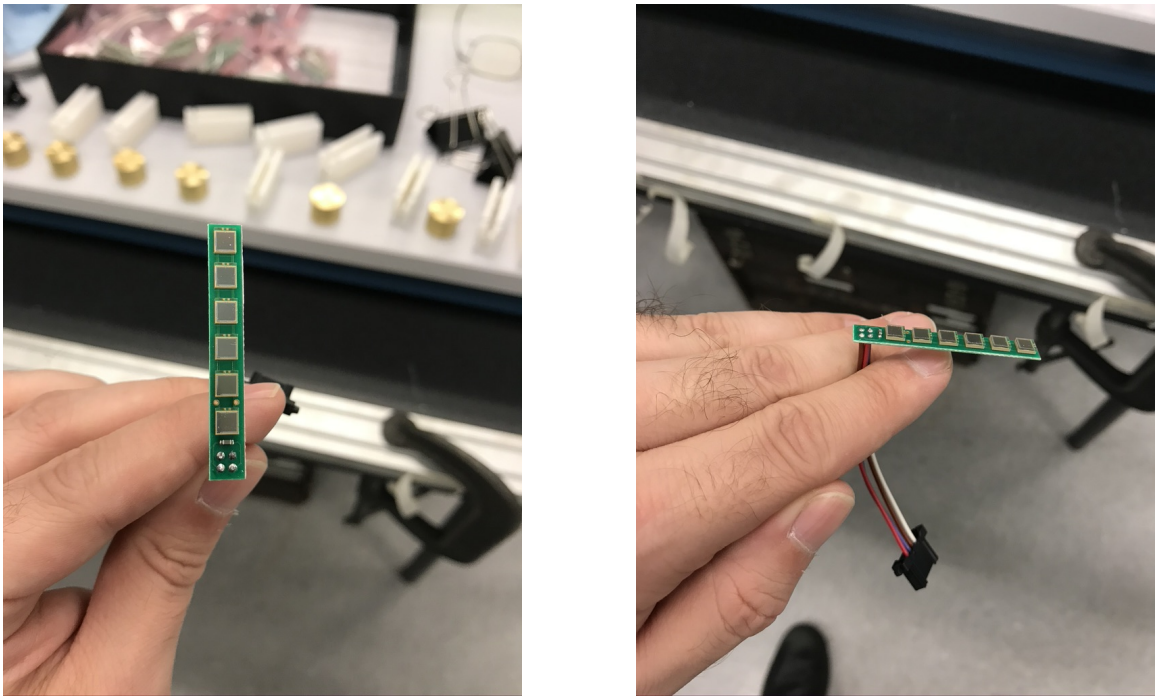

(a) Front View (b) Side View

Figure 2.17: A picture of the SiPM board for the FCS Hcal with SiPMs attached. There are 6 SiPMs and a thermistor on the board. You can also see the short cable that will be used to attach it to the FEE board.

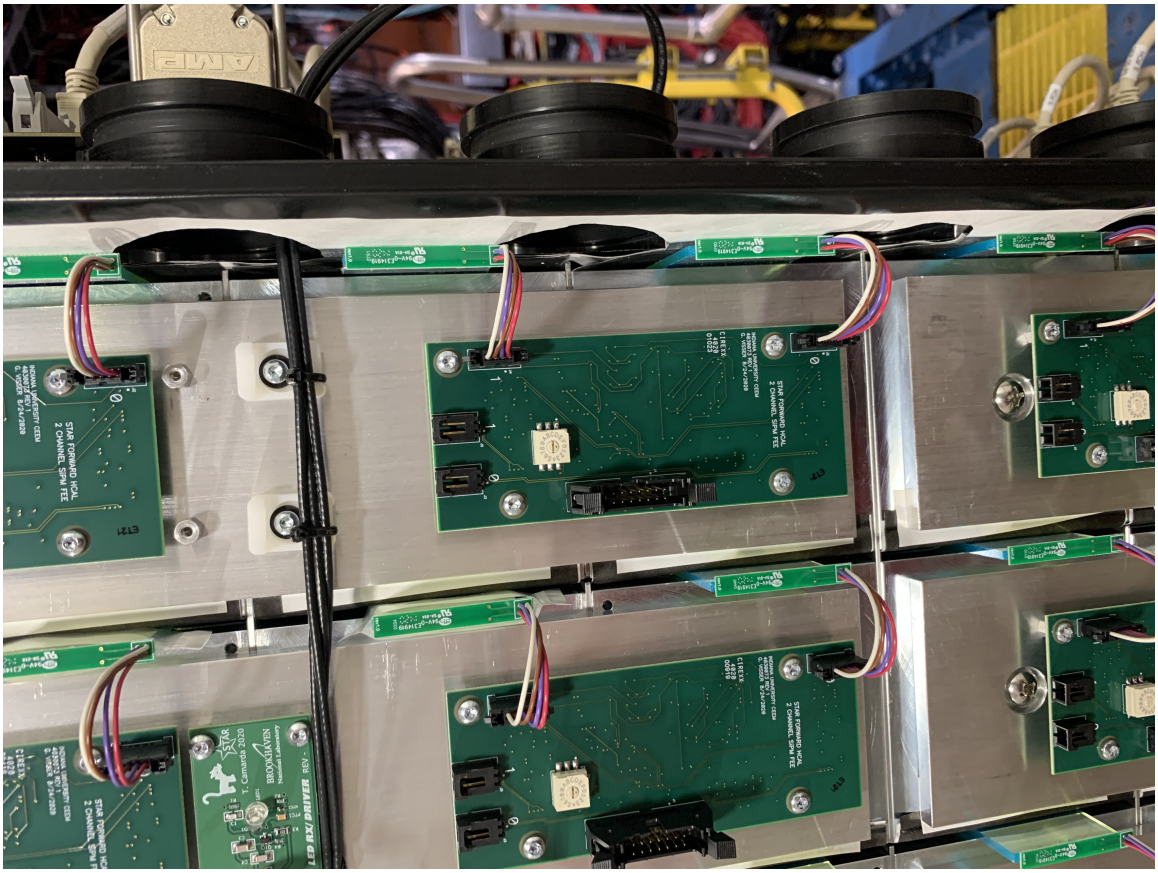

Figure 2.18: A picture of the FCS Hcal FEE board. *Image Courtesy of Akio Ogawa*

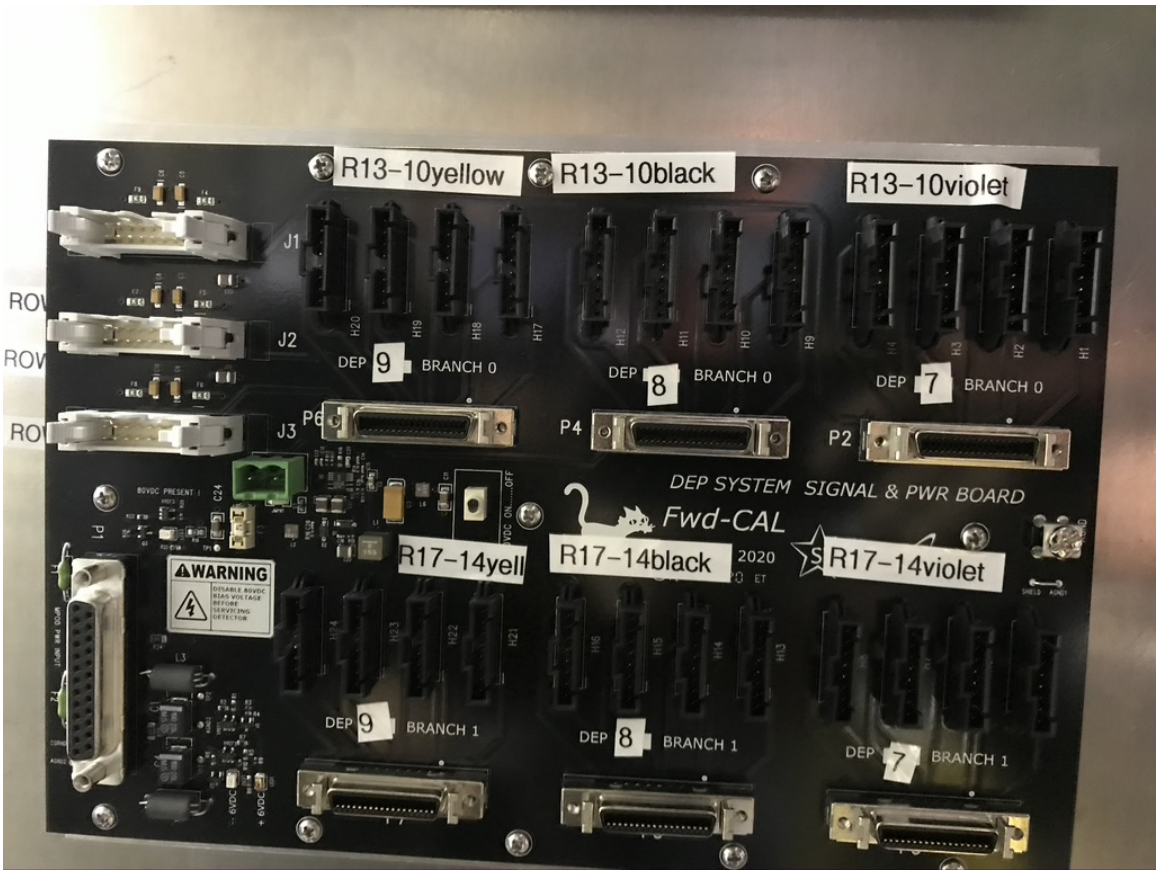

Figure 2.19: A picture of the PCB board that gathers the signals from up to 16 FEE boards using I^2C cables which are then directed to the DEP boards using similar cables.

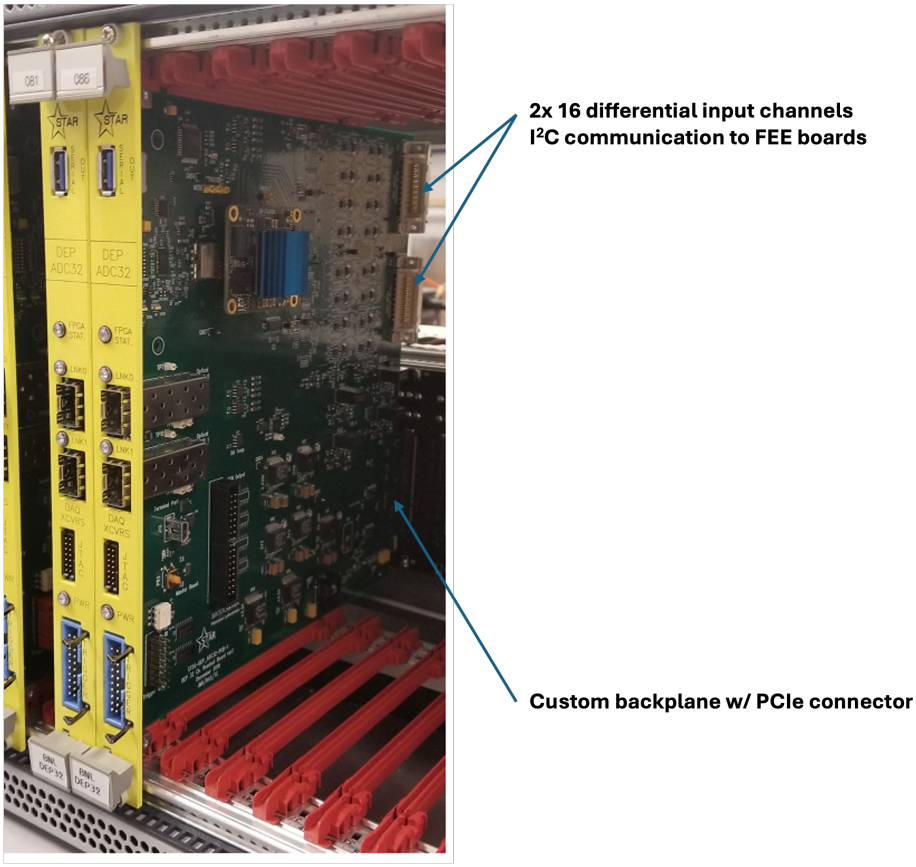

Figure 2.20: A picture of two DEP boards installed in a crate showing its various components. *Image Courtesy of Tim Camarada*

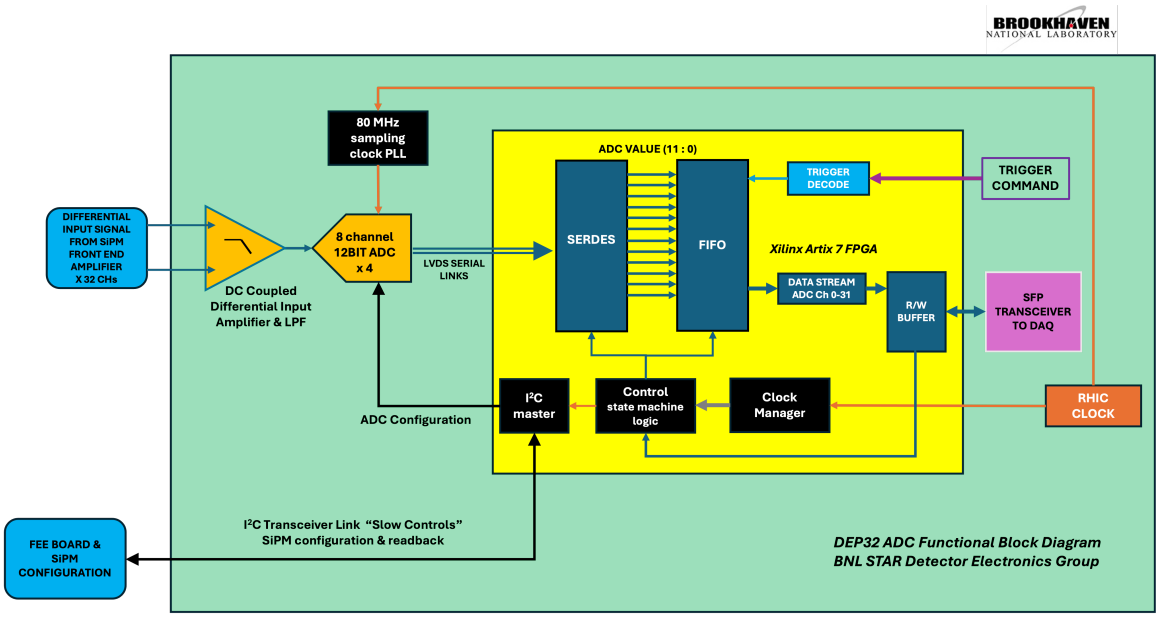

Figure 2.21: A block diagram showing the functional components of an FCS DEP board. *Image Courtesy of Tim Camarada*

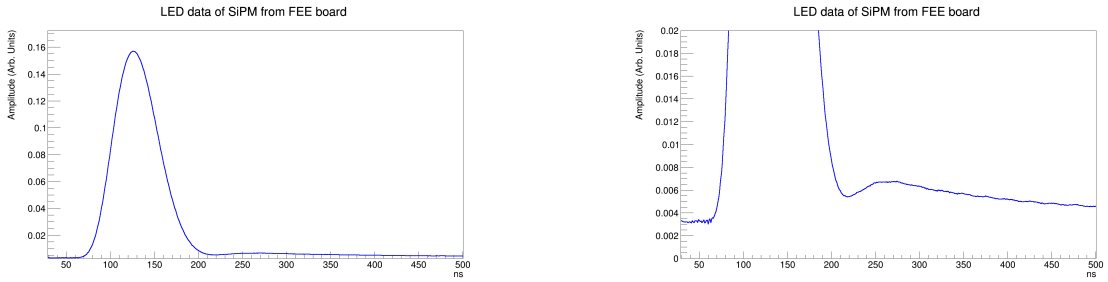

(a) Signal from LED data

(b) Zoomed in to show tail region

Figure 2.22: A plot of the response vs. time from a FEE board using LED pulses to generate the signal on the SiPM. The signal is about 100 ns wide with a distinct tail. After digitization the sharp valley will be integrated over but the overall feature of the tail will remain. The tail is an artifact of the electronics and is not part of the light signal output (thus the energy of the particle) it is one of the sources that need to be eliminated when computing the energy.

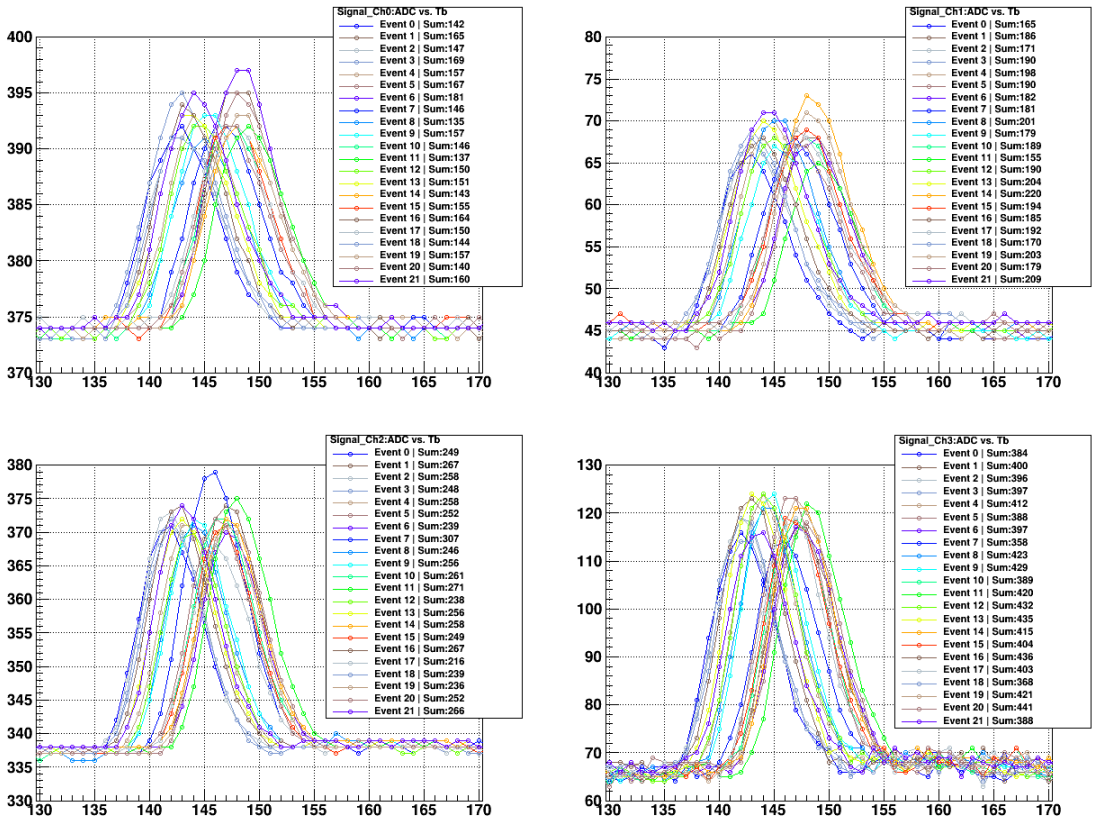

Figure 2.23: A plot of the ADC vs. tb from the DEP boards for many different LED events for four different Ecal channels. The important thing to notice is that the width and shape is consistent between events and channels. They are about 8 tb wide. The baseline varies due to differences in electronics for this test setup.

Chapter 3

Dataset and Quality Assurance

This work was performed using the STAR detector at RHIC. The data was taken in 2021 and 2022 otherwise known as RHIC Run-22. This chapter will discuss the performance of RHIC. The trigger logic and data collection. The reconstruction algorithm.

3.1 RHIC Performance in Run 22

RHIC collided transversely polarized proton beams at $\sqrt{s} = 510$ GeV during the years of 2021-2022 and designated as RHIC run 22. The total delivered luminosity was 807 pb^{-1} with an average polarization of 50% [2]. Figure 2.3 shows the RHIC delivered luminosity along with the average polarization over RHIC's operational period. The performance of Run 22 was similar to Run 17 (the last time RHIC ran transversely polarized protons at $\sqrt{s} = 510$ GeV) in terms of luminosity but the polarization was slightly lower due to an issue with the AGS primary motor generators and two failed helical dipole magnets (Siberian Snakes) [39]. The RHIC operation team was able to readjust the Siberian Snakes

in order to restore their functionality to some extent. However, this issue led to an overall lower polarization than in previous years.

3.2 FCS Trigger

The FCS trigger logic was handled by the DEP boards in four stages, i.e. each stage is handled by a different DEP board. The zeroth and first stage is the lowest level and deals with the raw information coming from the detector. The second stage applies some rudimentary cuts on the data from the first stage. The last stage has the highest level logic combining the information from the second stage triggers to create a high level trigger. The following will describe how all triggers in the FCS work however this work only used a trigger that fired on electromagnetic particles.

3.2.1 Trigger Stage 0

The stage 0 trigger algorithm is responsible for generating the adc sum and using the gain to compute E_T, so that the trigger thresholds are on E_T, for each tower of the Ecal (Hcal) that is connected to a single DEP board. A single DEP board has 32 channels and is able to digitize the signal for each channel into a 12 bit ADC for 8 timebins (counting starts at 0) in a single clock cycle (RHIC clock ticks every 107 ns so 13.5 ns per tb). The algorithm begins by summing the ADC from the 8 timebins and subtracting the pedestal. If the sum is less than zero then it gets set to zero. Next, it will multiply by the E_T gain, which is 10 bits with 4.6 fixed point. The E_T gain is 1 near the beam and 6 for the far right corner so removing the lower 6 bits is to remove the decimal point so that the E_T's GeV/ch

does not change near the beam. This helps to reduce the overall data volume. Finally it will do a rudimentary peak finding where it checks if there is a rising edge and then checking for falling edge after the rise. If the peak condition passes and if the gain corrected ADC sum is larger than zero, then it will truncate the last 6 bits of this sum and send this gain corrected ADC sum (which is now 19 bits) to the stage 1 DEP board.

This process of bit manipulation helps to reduce the data volume and doesn't effect the overall performance of the trigger logic as these lower bits only provide increased precision and won't effect the trigger decision noticeably.

The data collected, however, will be the raw tb and pedestal subtracted ADC values.

3.2.2 Trigger Stage 1

The stage 1 trigger algorithm will now take the 32 ch gain corrected ADC sum (19 bit) and make 8 sums such that each sum corresponds to a 2x2 arrangement (array) of towers in the Ecal (Hcal). In order to compensate and reduce this extra data volume the top 6 bits and lower 7 bits of this sum are cut off to make the final sum of the 2x2 array into an 8 bit number. These eight 8 bit numbers are sent to the stage 2 algorithm. The fPRE does not have such an arrangement of 2x2 arrays and thus this stage 1 grouping is not relevant. The fPRE threshold (FCS_PHTTHR) determines whether an fPRE hit will be true or false in the hit pattern bit vector. This 31 bit vector of the hit pattern will go to the stage 2 algorithm. There are 31 bits because there are 31 channels in a supersector of the EPD.

3.2.3 Trigger Stage 2

The stage 2 algorithm will take the 64 bit sums from each DEP board in stage 1 where there are 24 DEPs for Ecal and 9 DEPs for Hcal. This is combined with the 31 bit hit information from the fPRE to make the first set of physics level triggers. All DEP sums described at this stage have both a "North" (N) and "South" (S) counterpart to account for the different halves of the detector. However, before any logic is applied, it computes several quantities first. One of these is to combine the 64 bit sums of the 2x2 array into overlapping 4x4 sums for both Ecal ($Ecal4x4$) and Hcal ($Hcal4x4$). Overlapping in this way means that if there are 4 2x2 sums then you get 3 4x4 sums. Figure 3.1. This overlap is done to account for cases where the energy of an electromagnetic shower is split between two different 2x2 array of towers. It also computes the overall sum of the Ecal and Hcal 4x4 $Sum4x4 = Ecal4x4 + Hcal4x4$. The $Sum4x4$ is computed from the geometrically matched $Ecal4x4$ and $Hcal4x4$ using bit tables to speed up computation. There is an additional bit mapping of fPRE channels to $Ecal4x4$ to geometrically match the Ecal sum to the fPRE hit data. Using these quantities we can describe the logic of the FCS stage 2 triggers.

There were initially 3 "fcsEM" triggers that are aimed at triggering on any electromagnetic shower; these are fcsEM0, fcsEM1, fcsEM2 where increasing numbers mean increasing thresholds. Later in Run 22 a fourth fcsEM3 trigger was added. These thresholds are shown in table 3.1. In the table the digital value to E_T conversion is $1 \approx 0.0316\ GeV$. The values in parenthesis indicate a change in the trigger threshold during Run 22 starting after and including run number 23027049. E_T values are close approximates. The fcsEM trigger logic is as follows $(Ecal4x4 > Hcal4x4 * FCS\_EM\text{-}HERATIO\text{-}THR) \wedge$

($Sum4x4 > FCS\_EMTHR0/1/2/3$). The FCS_EM-HERATIO-THR is a digital value that represents a fraction of the $Hcal4x4$. This ensures that most of the energy is deposited in the Ecal and that the energy is above some minimum value given in table 3.1.

There are 3 "fcsELE" triggers whose aim is to combine the fcsEM triggers and the fPRE hit pattern to select electron electromagnetic showers over photon ones; these are "fcsELE1, fcsELE2, fcsELE3" where increasing numbers once again mean increasing thresholds which can be seen in table 3.1. The fcsELE trigger has the same logic as the fcsEM trigger but uses different thresholds for the $Sum4x4$ and is the numbers shown in table 3.1.

There are 3 "fcsHAD" triggers that is used to trigger on hadrons and are numbered from fcsHAD0, fcsHAD1, fcsHAD2 where increasing numbers again mean increasing thresholds and are given in table 3.1. The fcsHAD trigger logic is similar to the fcsEM one except to select on more energy in the Hcal. The fcsHAD logic is: $(Ecal4x4 < Hcal4x4 * FCS\_HAD\text{-}HERATIO\text{-}THR \wedge Sum4x4 > FCS\_HADTHR0/1/2$. The FCS_HAD-HERATIO-THR is, once again, a digital value that represents a fraction of the $Hcal4x4$ and ensures that most of the energy was deposited in the Hcal.

A series of jet patch (JP) triggers also exist in order to trigger on jets. Jets, in general, cover a much wider area than a simple 4x4 region of the Ecal or Hcal. To form the JP regions we start with the Ecal and Hcal 4x4 regions because that is the information we will have from the DEP boards. These 4x4 regions are then split into 5 semi-overlapping regions: A, B, C, D, E and can be seen in . The regions are chosen such that A is a central one, B and C are symmetric with respect to the top and bottom and share the same

threshold, D and E also have a top and bottom symmetry (but offset from B/C) and use the same threshold. The thresholds can be seen in table 3.1.

Lastly, there are Ecal and Hcal cosmic triggers (also used in debugging) that fire on the Ecal total energy (ETOT) or the Hcal total energy (HTOT). There is also a high tower trigger for both the Ecal (EHT) and Hcal (HHT) which are also used for debugging. These thresholds are shown in table 3.1.

Certain stage 2 triggers form the final physics level triggers. However, these stage 2 triggers can be combined to form higher level triggers. The various triggers discussed here are used to form bit vectors which are then sent to another DEP board which will be the basis of the stage 3 triggers.

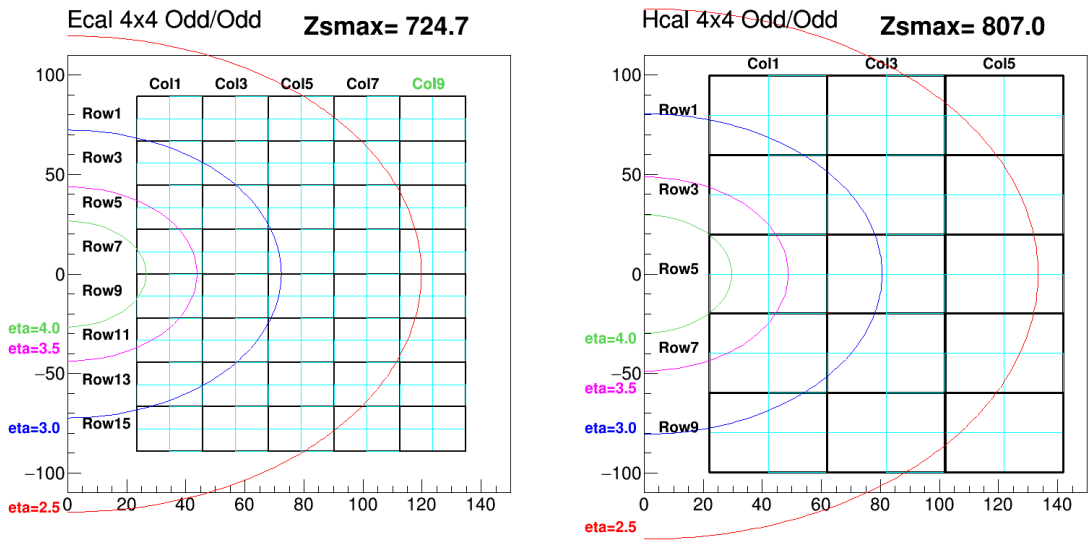

Figure 3.1: A diagram showing the overlapping 2x2 and 4x4 regions in the Ecal and Hcal. The black lines indicate odd numbered rows and columns and are labeled. The cyan ones are the even numbered ones and unlabeled.

Table 3.1: Table of FCS trigger threshold names and values with prefix "FCS_" removed.

Threshold Name	Digital Value	Physics E_T	Description
PHTTHR	200(250)	-	fPRE hit threshold
EM-HERATIO-THR	32	-	Hcal to Ecal energy ratio (32 = 0.25)
HAD-HERATIO-THR	32	-	Hcal to Ecal energy ratio (32 = 0.25)
EMTHR2	160	5 GeV	EM particle (γ,$e^{\pm}$) high
EMTHR1	112	3.5 GeV	EM particle (γ,$e^{\pm}$) mid
EMTHR0	64	2 GeV	EM particle (γ,$e^{\pm}$) low
ELETHR2	40(32)	1.1 GeV	$e^{\pm}$ high
ELETHR1	32(25)	0.9 GeV	$e^{\pm}$ mid
ELETHR0	25	0.8 GeV	$e^{\pm}$ low
HADTHR2	192	6 GeV	Hadron ($h^{\pm}$) high
HADTHR1	128	4 GeV	Hadron ($h^{\pm}$) mid
HADTHR0	64	2 GeV	Hadron ($h^{\pm}$) low
JPATHR2	254	8.0 GeV	JP region A High
JPATHR1	192	6.0 GeV	JP region B Mid
JPATHR0	128	4.0 GeV	JP region A Low
JPBCTHR2	254	8.0 GeV	JP regions B & C High

JPBCTHR1	192	6.0 GeV	JP regions B & C Mid
JPBCTHR0	128	4.0 GeV	JP regions B & C Low
JPBCTHRD	160	5.0 GeV	JP regions B & C asymmetry
JPDETHR2	254	8.0 GeV	JP regions D & E High
JPDETHR1	192	6.0 GeV	JP regions D & E Mid
JPDETHR0	128	4.0 GeV	JP regions D & E Low
JPDETHRD	160	5.0 GeV	JP regions D & E for asymmetry
EHTTHR	32	-	High tower Ecal (Debug)
HHTTHR	32	-	High tower Hcal (Debug)
ETOTTHR	50	-	Total Ecal energy (Debug)
HTOTTHR	50	-	Total Hcal energy (Debug)

3.2.4 Trigger Stage 3

The stage 3 triggers are formed using logical combinations from stage 2. The bit vectors from stage 2 are sent from both N and S to a single DEP board which will perform the logical operations that give the final set of high level triggers. The high level triggers in Run 22 were aimed at measuring jets, and the Drell-Yan (DY) process. The final list of physics triggers and their logic can be seen in table 3.2. The prefix "fcs" has been removed for readability. There were two more triggers not listed in the table: the "upcJpsiNS" and the "upcJpsiSN" as they are not a part of the data stream analyzed. Also, not listed are the "fcsEM0_tpc", "fcsEM1_tpc", "fcsEM2_tpc", and the "fcsEM3_tpc" as they had the exact same logic as the corresponding fcsEM0/1/2/3 triggers except there was an additional requirement that the TPC be live.

Table 3.2: List of FCS physics level triggers and their logic from stage 2 to stage 3.

Name	Logic	Physics/Description
JP2	$\forall$JP-N $\vee$ $\forall$JP-S	Highest threshold jets
JPA1	JPA1-N $\vee$ JPA1-S	Mid threshold JP-A
JPA0	JPA0-N $\vee$ JPA0-S	Low threshold JP-A
JPBC1	JPBC1-N $\vee$ JPBC1-S	Mid threshold JP-BC
JPBC0	JPBC0-N $\vee$ JPBC0-S	Low threshold JP-BC
JPDE1	JPDE1-N $\vee$ JPDE1-S	Mid threshold JP-DE
JPDE0	JPDE0-N $\vee$ JPDE0-S	Low threshold JP-DE
DiJP	$\forall_{0(1)}$JP-N $\wedge$ $\forall_{0(1)}$JP-S	Dijet

DiJPAsy	$(\forall_{0(1)}$JP-N $\wedge$ $\forall_{1(0)}$JP-S) $\vee$ $(\forall_{1(0)}$JP-N $\wedge$ $\forall_{0(1)}$JP-S)	DiJet asymmetric threshold
DY	ELE2-N $\wedge$ ELE2-S	Main DY at threshold=1 GeV
JPsi	ELE1-N $\wedge$ ELE1-S	J/ψ at threshold=0.8 GeV
DYNoEpd	EM3-N $\wedge$ EM3-S	DY monitor without EPD
DYAsy	(ELE2-N $\wedge$ ELE1-S) $\vee$ (ELE1-N $\wedge$ ELE2-S)	DY monitor with asymmetric threshold
Had2	HAD2-N $\vee$ HAD2-S	Hadron high threshold
Had1	HAD1-N $\vee$ HAD1-S	Hadron mid threshold
Had0	HAD0-N $\vee$ HAD0-S	Hadron low threshold
EM2	EM2-N $\vee$ EM2-S	π^0/γ high threshold
EM1	EM1-N $\vee$ EM1-S	π^0/γ mid threshold
EM0	EM0-N $\vee$ EM0-S	π^0/γ low threshold
EM3	EM3-N $\vee$ EM3-S	π^0/γ very low threshold
ELE2	ELE2-N $\vee$ ELE2-S	$e^{\pm}$ high threshold
ELE0	ELE1-N $\vee$ ELE1-S	$e^{\pm}$ mid threshold
ELE1	ELE0-N $\vee$ ELE0-S	$e^{\pm}$ low threshold
EHT-N	-	debug
EHT-S	-	debug
HHT-N	-	debug
HHT-S	-	debug

ETOT-N	-	cosmic
ETOT-S	-	cosmic
HTOT-N	-	cosmic
HTOT-S	-	cosmic

3.3 Reconstruction

The reconstruction of the particle candidates in the Ecal and Hcal happen in two levels. The first level forms clusters and does a moment analysis to determine how wide the cluster is. The next level is doing a shower shape fit to the clusters in order to better determine the particle positions and energies.

3.3.1 Clustering Algorithm

The clustering algorithm in the FCS is similar to the one used for a previous STAR detector the Forward Meson Spectrometer (FMS) [5] [6]. The clustering algorithm starts with the highest energy hit and then checks if any adjacent towers in a cross pattern also have a hit. If not, then finished otherwise add the adjacent tower to the cluster. Keep adding adjacent towers until there are none left. A cluster is then just all contiguous towers that have a hit. The minimum threshold for a seed tower is 1 GeV to avoid the MIP region and the minimum threshold for a tower to considered in the clustering algorithm is 0.01 GeV. A logarithmic weight of the towers is computed according to eq. 3.1 [51]. This serves as a new centroid of the shower. Furthermore a log weighted moment analysis is performed by constructing a moment matrix $\sigma = \begin{pmatrix} \sigma_x & \sigma_{xy} \\ \sigma_{yx} & \sigma_y \end{pmatrix}$ where the elements are given by eq. 3.2. The largest of two eigenvalues of σ is called σ_{max} and smallest eigenvalue is called σ_{min} and it is used to determine whether the cluster contains one or two photons [47] [51]. This moment analysis is necessary as the energy of the π^0 increases the opening angle of the two photons decreases. This moment analysis will be important in the next step when the cluster is fit to the profile of an electromagnetic shower.

$$x_{clu} = \frac{\sum_{i \in clus} ln(E_i + 0.5) x_i}{\sum_{i \in clus} ln(E_i + 0.5)}$$
$$y_{clu} = \frac{\sum_{i \in clus} ln(E_i + 0.5) y_i}{\sum_{i \in clus} ln(E_i + 0.5)} \tag{3.1}$$

$$\sigma_x^2 = \frac{\sum_i ln(E_i + 0.5)(x_i - x_{clu})^2}{\sum_i ln(E_i + 0.5)}$$
$$\sigma_y^2 = \frac{\sum_i ln(E_i + 0.5)(y_i - y_{clu})^2}{\sum_i ln(E_i + 0.5)} \tag{3.2}$$
$$\sigma_{xy}^2 = \sigma_{yx}^2 = \frac{\sum_{i \in clus} ln(E_i + 0.5)(x_i - x_{clu})(y_i - y_{clu})}{\sum_{i \in clus} ln(E_i + 0.5)}$$

3.3.2 Point Reconstruction

The next step in the reconstruction is to fit the clusters to a known shower shape profile. The transverse profile of electromagnetic showers has been well studied over the years [15] [30] [16] [47] [51] [22]. The form of the shower shape is given by eq.

The points are fitted to the cluster based on the moment analysis. The moment analysis determines whether a single particle or two particles generated the shower. The shower is then fit to a shower shape. The moment analysis may have ambiguities and in those cases it will fit the cluster to 1 and 2 particles and then take the best fit.

Chapter 4

Analysis Details and Results

This chapter will detail how the measurement was done like: event selection criteria, vertex reconstruction, beam polarization, signal and background analysis as well as the final measured value of A_N vs. x_F for the π^0.

4.1 Overview of Analysis

4.1.1 π^0 reconstruction

The π^0 has a very short lifetime. It is 10^{-17} seconds and decays two photons(γ) with a branching ratio of 98.8% [34]. This means that we need to separate the $e^{\pm}$ showers from the γ showers in the Ecal. A schematic showing the π^0 decay kinematics can be seen fig. 4.1. The Ecal will measure the energy of the two photons, E_1 and E_2, and the reconstructed point position information along with the z-vertex will be used to reconstruct the opening angle (α) [1]. The invariant mass of the π^0 is then given by eq. 4.1, where a

[1] In *pp* collisions the x, and y values of the vertex are much smaller than the z-vertex and therefore assumed to be zero.

quantity $Z_{\gamma\gamma} = \frac{|E_1 - E_2}{E_1 + E_2}$ has been introduced and is the energy asymmetry of the two photon pairs.

$$M^2_{(inv)ariant} = (E_1 + E_2)^2(1 - Z^2_{\gamma\gamma})sin^2\frac{\alpha}{2} \tag{4.1}$$

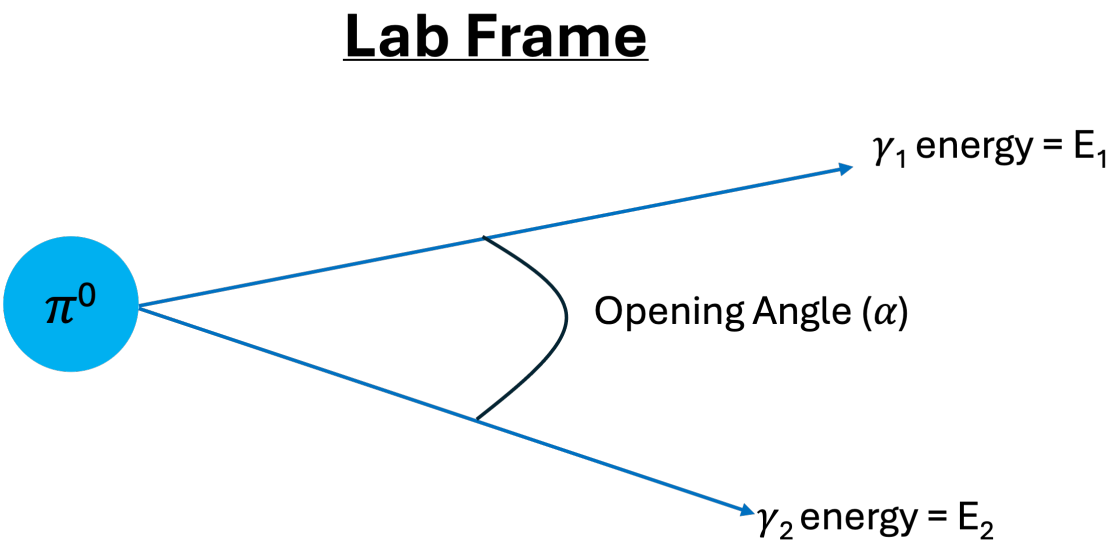

Figure 4.1: Diagram showing π^0 decay.

To reconstruct the π^0 we start by grabbing all the points (described in section 3.3.2). The point represents a photon candidate. A minimum energy cut of 1 GeV is applied to the point and all points that reside on the edge towers of the Ecal are rejected (inner and outer rows and columns). This is done to avoid edge effects of the electromagnetic shower and ensure that the measured energy is of the whole shower and not part of it. The point is projected back to the collision z-vertex (see section 4.1.2) and the x,y intersection of that line at the z value of the EPD is used to find the corresponding EPD tile. The nMIP value of the EPD tile is checked and if both points satisfy the requirement that the

$nMIP < 0.7$ for the tile [2] then those points are taken as the photon candidates to use in reconstructing the π^0.

4.1.2 Vertex Reconstruction

The z-vertex was reconstructed using the timing information from the VPD, BBC, or EPD. The timing information is a digital value referred to as the TAC (Time to Analog Converter). For instance, the TAC difference multiplied by 0.2475 gives the z-vertex in cm for the BBC and EPD. The VPD had the highest priority as it had the best resolution of the three [51], next priority is the EPD with slightly worse resolution, and lastly the BBC. The z-vertex distributions from the VPD, EPD, and BBC can be seen in fig. 4.2. The correlation between the EPD with the VPD clearly shows how well the EPD is performing. The BBC is not as well correlated which is why it had the lowest priority.

4.2 Event Selection

The event selection begins by selecting on those events that pass the following criteria

- Event must have spin information
- This avoids analyzing events when the bunch is empty
- Trigger must be an FCSEM trigger
- di-photon pair p_T must pass trigger threshold

[2] Note: This also includes potential non-existent tiles (because they would have an nMIP of 0) from the projection. However, almost all points had a valid projection and this expected to be rare.

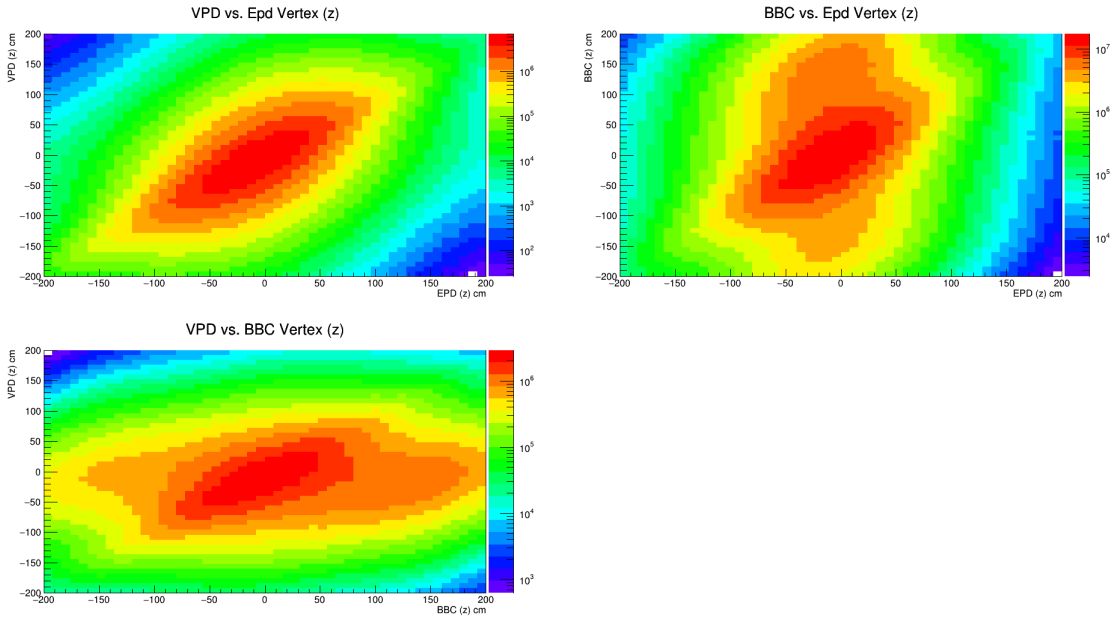

Figure 4.2: Z-vertex cross correlation distributions from VPD, EPD, and BBC.

- Collision z-vertex is ± 150 cm

There is an additional constraint on the di-photon candidate that $Z_{\gamma\gamma} < 0.7$. This ensures that the second photon contains at least some of the energy and helps clean up potential single photon candidates. The resulting points after applying these cuts is shown in fig. 4.3. The energy of the pi^0 was split into 8 bins: 0-15 GeV, 15-20 GeV, 20-25 GeV, 25-30 GeV, 30-40 GeV, 40-55 GeV, 55-70 GeV, 70-100 GeV. The uneven splitting is to account for the fact that there are less π^0's reconstructed at the higher energies and this splitting will balance out the number of events in each bin much better, this can be seen in fig. 4.4. Figure 4.4 also shows the di-photon candidate QA after all cuts have been applied. The overal; distribution in ϕ-pseudorapidity(η) space as well in xy space is consistent with the geometry of the FCS. The invariant mass distribution also shows a clear peak at the π^0 mass of 0.135 GeV/c^2 [34]. There is also an indication of an η meson peak at its mass

of 0.548 GeV/c^2 [34]. The energy distribution has spikes in the high energy region which could potentially affect our results in that highest bin from 70-100 GeV. The other thing to note is how the energy is peaked at around 25 GeV and falls steeply after that, which is the reason for choosing such uneven energy bins. The $Z_{\gamma\gamma}$ distribution also looks reasonable as the most asymmetric photons have been ruled out and and the choice of 0.7 does not significantly impact the statistics. Lastly, the effect of applying the nMIP cut is shown. There is an enhancement of the π^0 peak when looking at the normalized distribution. The $nMIP \geq 0.7$ cut is also shown to highlight how such a choice is affecting the result. The low mass region is enhanced and the η meson peak goes away as is expected.

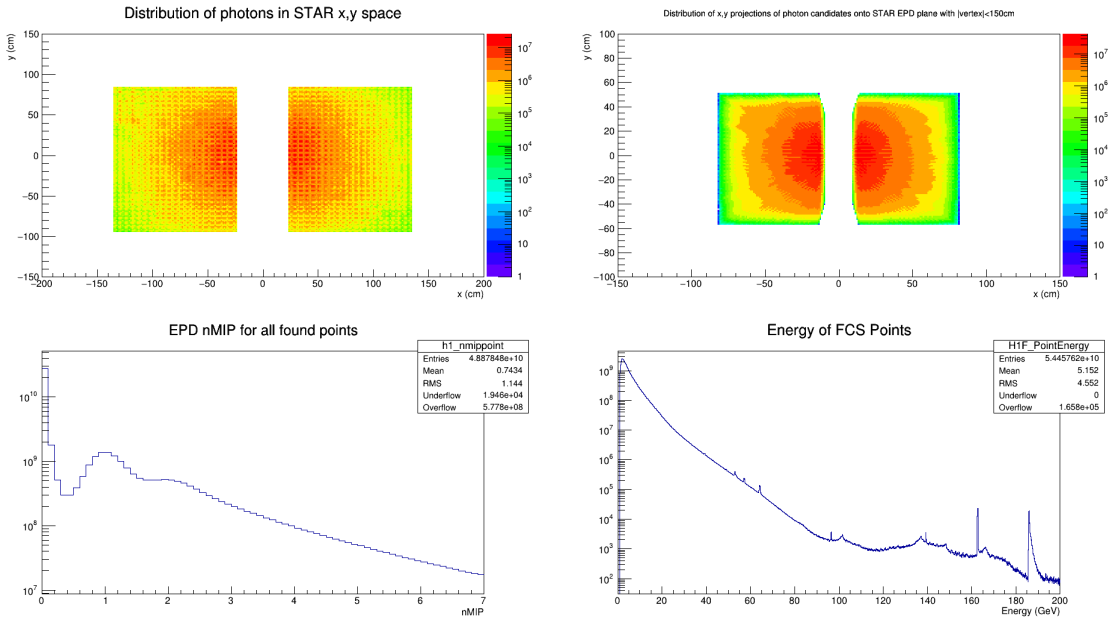

Figure 4.3: Point QA after applying cuts described in the text. The points are well distributed and the projections to the EPD are reasonable. The energy distribution has some spikes but this could be due to some bad runs. The EPD nMIP distribution is showing a nice peak at 1 as it is expected.

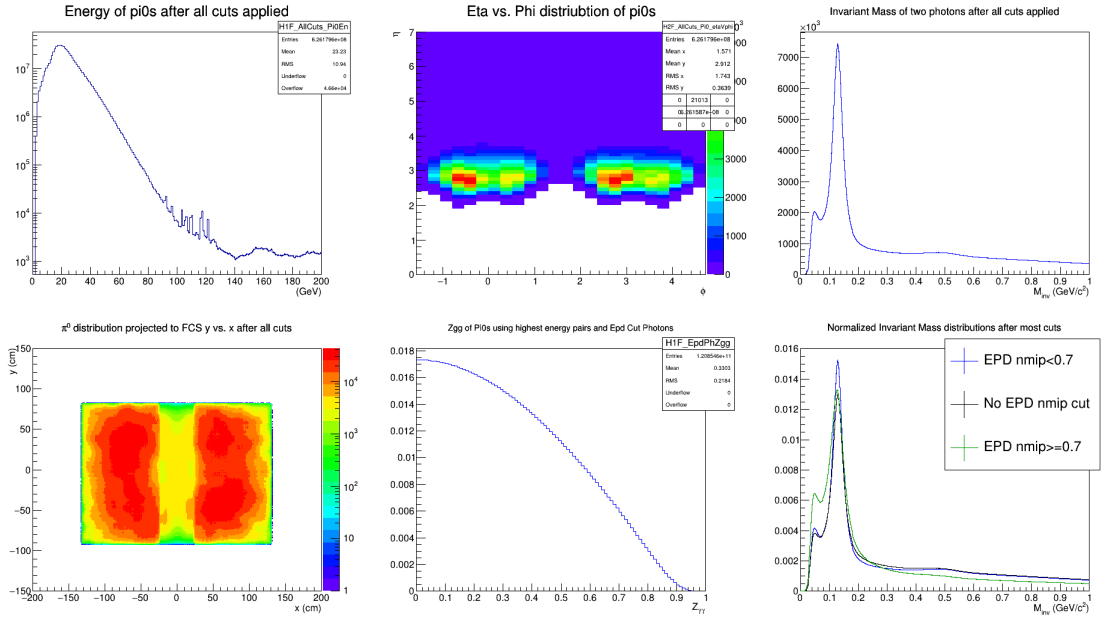

Figure 4.4: Di-photon pair QA plots after applying cuts described in the text.

4.3 A_N Calculation

To calculate A_N we use the cross ratio formula to help reduce systematics [51]. The cross ratio formula is given by eq. 4.2 and is used to compute the raw asymmetry (ϵ). The formula requires that you count the number of particles N for the various spin orientations and whether it is going to the left or right of the plane formed by the spin and momentum of the proton. The diagram in fig. 4.5 helps to illustrate the values in eq. 4.2. ϵ is related to the A_N by eq. 4.3, where P is the polarization and ϕ is the azimuthal angle. The data in this analysis was split into 24 bins of equal size from $0 - 2\pi$ for the angle ϕ, however as we care about a left right asymmetry this leaves 12 ϕ values in calculation of ϵ. To compute x_F the formula is $x_F = p_L/p_L^{max}$ where $p_L = |\overrightarrow{p}|tanh(\eta)$ and p_L^{max} is the beam energy of 255 GeV. The approximation $|\overrightarrow{p}|tanh(\eta) = E_{\pi^0}$ is used, which is a good approximation for the energies of the π^0 that we use; furthermore $tanh(\eta) \approx 1$ for the FCS

geometry. Therefore $x_F \approx E_{\pi^0}/255$. This means that the x_F bins match the energy bins and the error on the x_F will encompass the entire energy (now x_F) bin.

The final A_N will be combination of ϵ in the signal region (ϵ_{sig}) and the background region (ϵ_{bkg}). The signal region is defined as $0.1 \leq M_{inv} \leq 0.2$ and the background region as $0.3 \leq M_{inv} \leq 0.4$. This is done to subtract the effects of the background from the final A_N. The signal region was chosen as the peak at the π^0 mass of M_{inv} distribution of the di-photon pairs (fig. 4.4). The background region was chosen to be far enough outside of the π^0 mass peak region and to exclude the peak from the η meson. Figure 4.6 shows the number of π^0s at the various ϕ and energy bins for the spin up and down states of the blue and yellow beam for the signal region. Figure 4.7 is the same as fig. 4.6 except for the background region. These histogram can be used to compute ϵ for for blue beam in the signal region (fig. 4.8), the yellow beam in the signal region (fig. 4.9), the blue beam in the background region (fig. 4.10), and the yellow beam in the background region (4.11). In addition, those figures do a fit to the function $A * cos(\phi + \phi_0)$ where the phase ϕ_0 is just a cross check to ensure it is consistent with zero. The fitted value of A along with the polarization measurements shown in fig. 4.12 will be used to compute A_N^{sig} and A_N^{bkg} for the signal and background regions respectively. The polarization used to compute A_N will be the mean of the histogram shown in fig. 4.12 for blue and yellow beam data respectively. The mean is $\approx 56\%$, which is consistent with the RHIC performance shown in fig. 2.3. The final results for A_N^{sig} and A_N^{bkg} can be seen in fig. 4.13 and fig. 4.14 respectively. A_N^{sig} is increasing with $x_F > 0$ and is consistent with zero when $x_F < 0$ as expected. A_N^{bkg} is consistent with zero whether $x_F > 0$, or $x_F < 0$ as expected.

The final background corrected A_N is computed using eq 4.4 where r is the background ratio defined as $r = N_{bkg}/N_{sig}$ where N_{bkg} is the integral of the background function in the signal region and the N_{sig} is total integral under signal region in the invariant mass distribution for every energy bin. We only care about the energy bins because we are assuming, and as the data shows, the π^0 distribution overall is not dependent on ϕ. The fit function chosen for the signal (peak) region is a skewed Gaussian as has been used before in a previous analysis [51]. The background function is a 4^{th} order polynomial. It was chosen because it was able to best capture the high and low mass regions for all the different energies. The overall fit function then is a sum of the skewed Gaussian and the 4^th order polynomial. This fit is performed on every energy bin and the results can be seen in fig. 4.15. The fitting region excluded the $0.4 \leq M_{inv} \leq 0.6$ to avoid the η meson in the background function fit. Also, the fitted region began at 0.045 GeV to avoid the sharp rise at the very low M_{inv} region in some of the histograms. N_{bkg} is computed from the integral of only the 4^th order polynomial using the parameters from the overall fit function. All but the highest energy bin has a fit that matches the distribution; there the π^0 peak is harder to distinguish from the background. The final background corrected A_N is shown in fig. 4.16. It is increasing with x_F as expected for $x_F > 0$ and is consistent with zero for $x_F < 0$. The figure only shows statistical errors. A comparison of A_N with [5] is shown in fig. 4.17 where it can clearly be seen that this measurement has much lower statistical errors but follows the same trend.

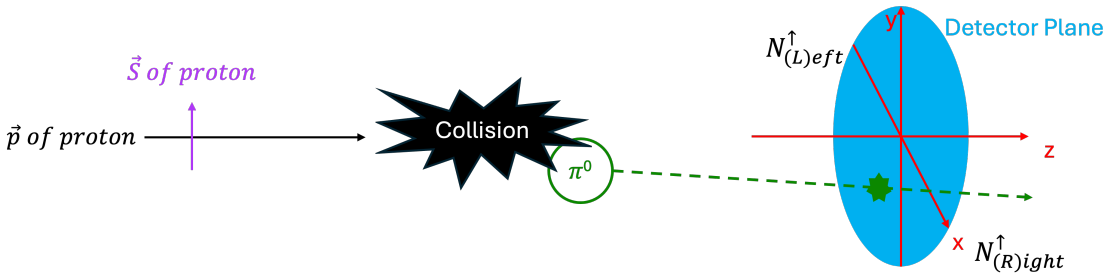

Figure 4.5: Illustration showing how the ϵ is computed from counting the π^0's. The illustration shows one count for $N_L^{\uparrow}$. The analogous proton down state is not shown can be inferred from the same diagram.

$$\text{Raw } A_N(\epsilon) = \frac{\sqrt{N_L^{\uparrow}N_R^{\downarrow}} - \sqrt{N_L^{\downarrow}N_R^{\uparrow}}}{\sqrt{N_L^{\uparrow}N_R^{\downarrow}} + \sqrt{N_L^{\downarrow}N_R^{\uparrow}}} \tag{4.2}$$

$$\epsilon = PA_N cos(\phi) \tag{4.3}$$

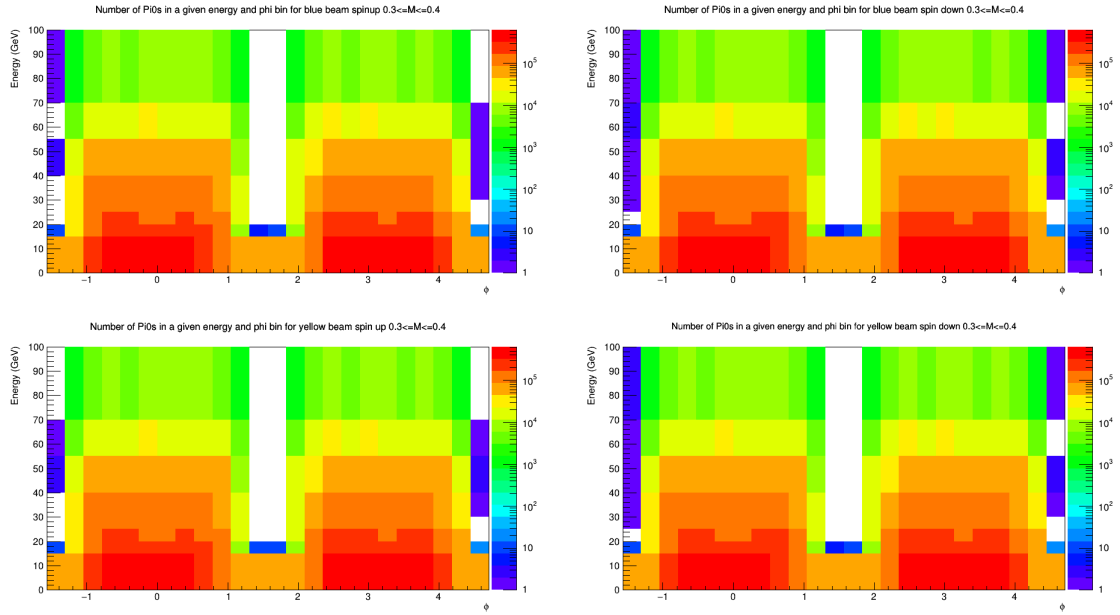

Figure 4.7: Number of π^0's in the background region binned in energy and ϕ.

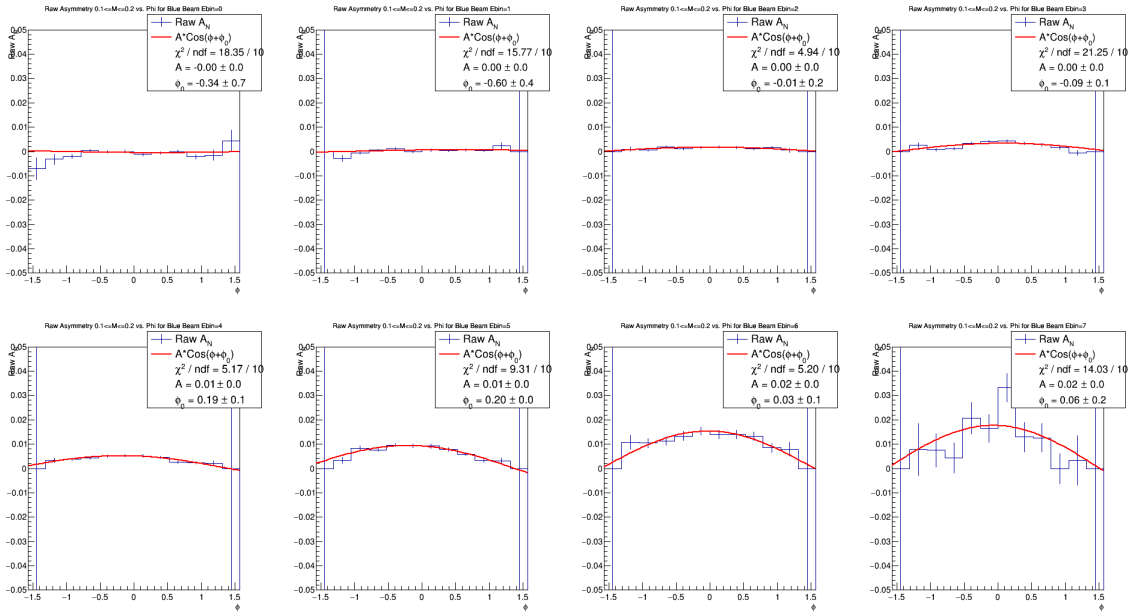

Figure 4.8: ϵ as a function of ϕ for the blue beam in the signal region for the different energy bins along with a fit to the function $A * cos(\phi + \phi_0)$. The extra phase ϕ_0 is just a cross check.

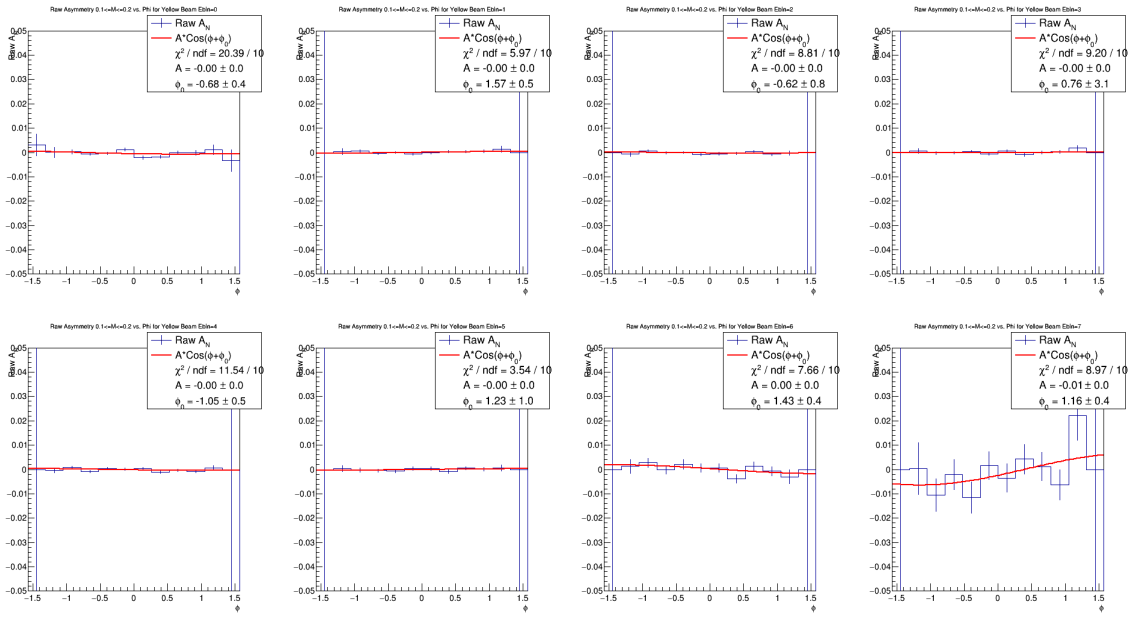

Figure 4.9: Same as fig. 4.8 except for yellow beam in the signal region.

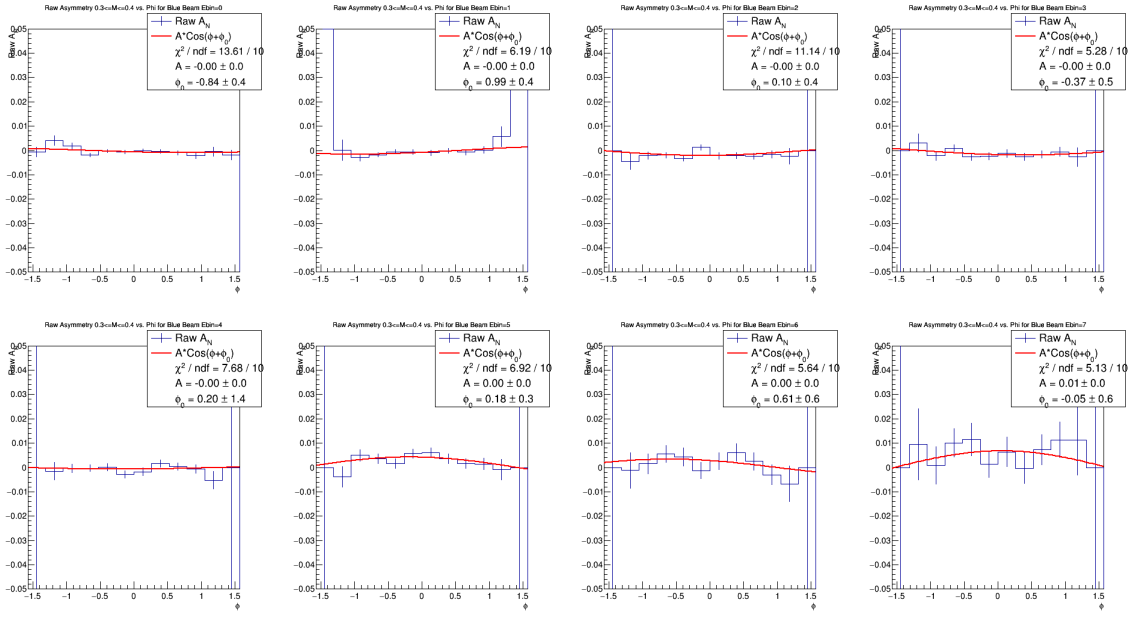

Figure 4.10: Same as fig. 4.8 except for blue beam in the background region.

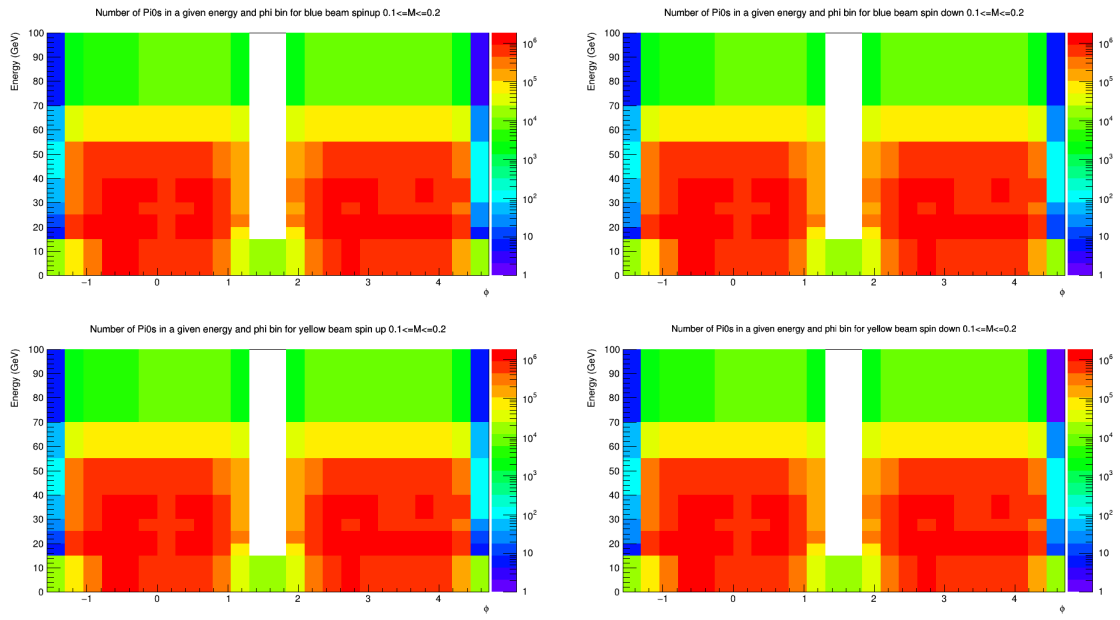

Figure 4.6: Number of π^0's in the signal region binned in energy and ϕ.

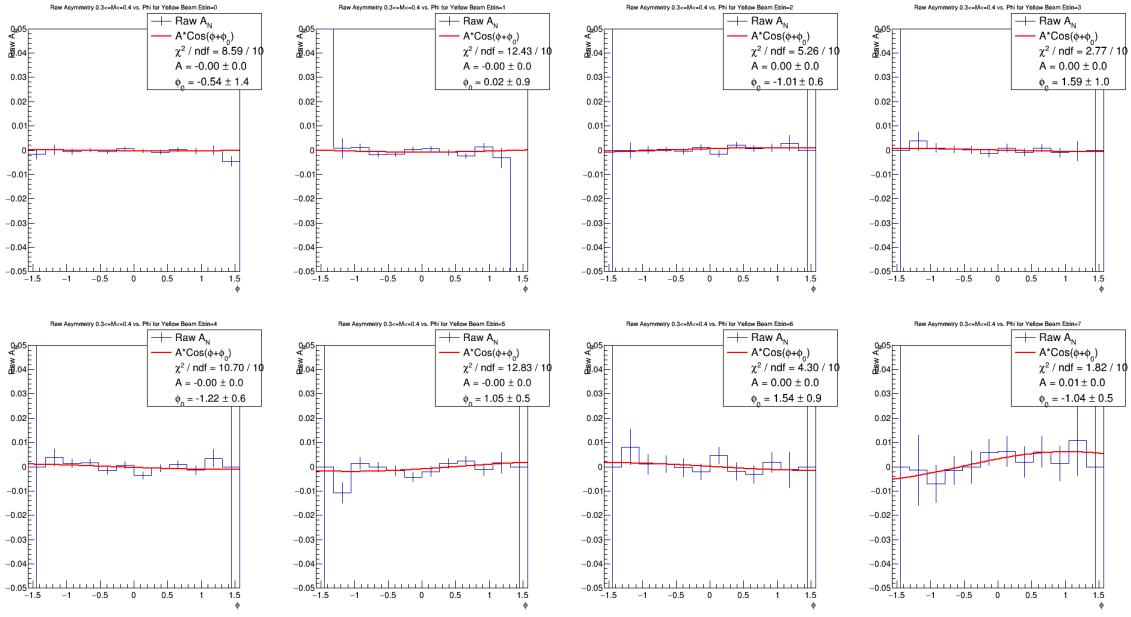

Figure 4.11: Same as fig. 4.8 except for yellow beam in the background region.

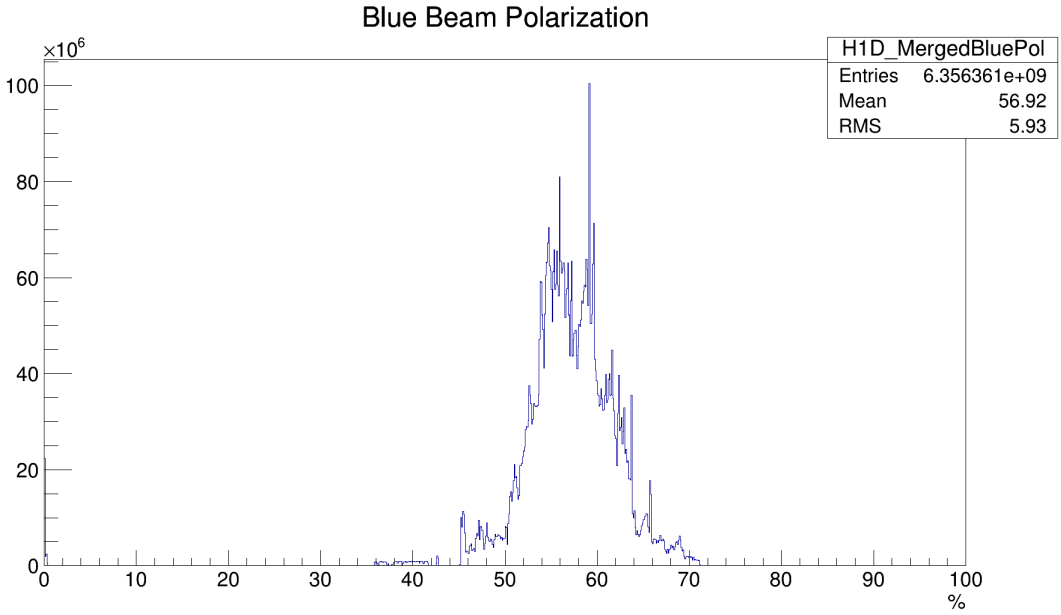

(a) Blue Beam

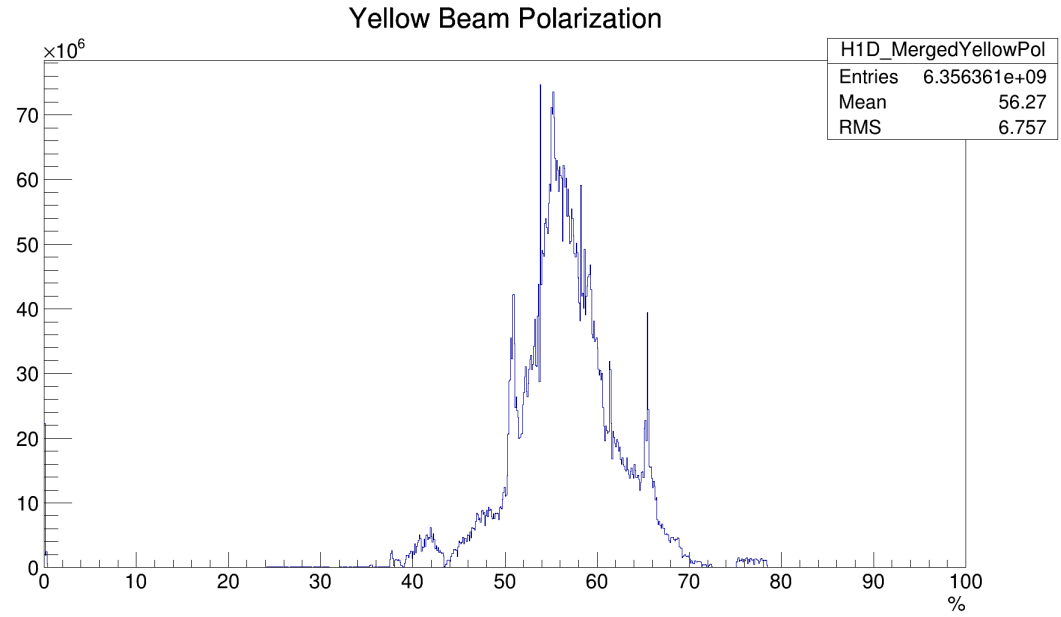

(b) Yellow Beam

Figure 4.12: Histogram of the blue and yellow beam polarization percentage for the data analyzed.

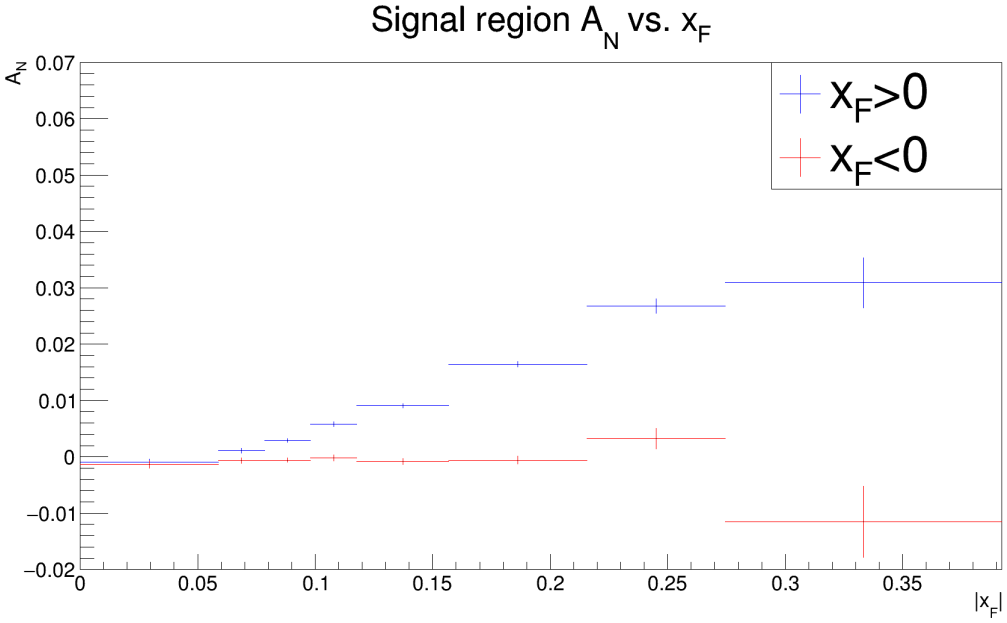

Figure 4.13: A_N as a function of x_F in the signal region. For $x_F > 0$ A_N is increasing and for $x_F < 0$ A_N is consistent with zero. Only statistical errors are shown.

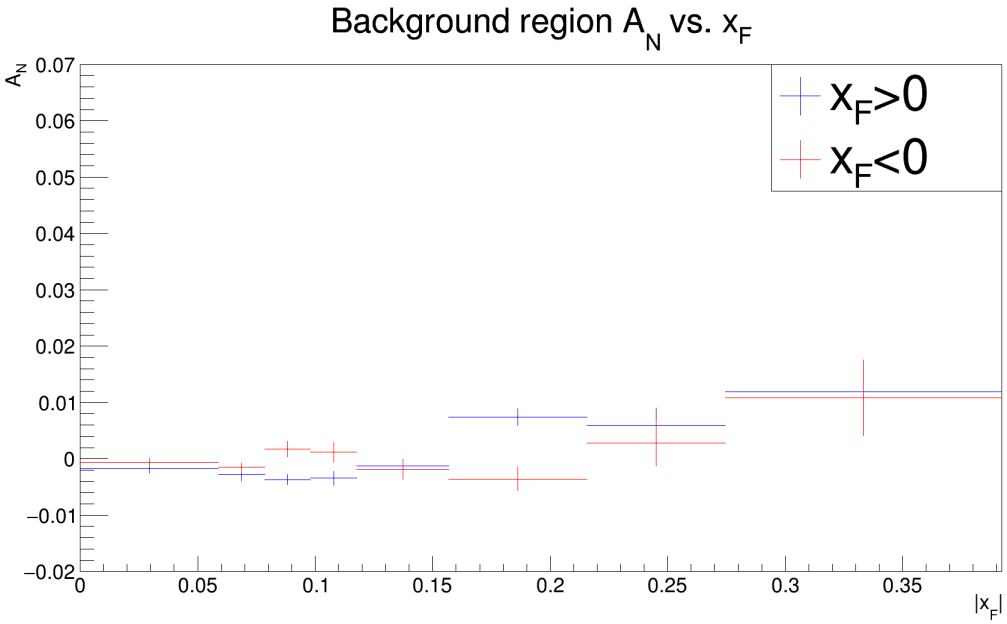

Figure 4.14: A_N as a function of x_F in the background region. For either $x_F > 0$, or $x_F < 0$ A_N is consistent with zero. Only statistical errors are shown.

$$A_N = \frac{A_N^{sig} - r * A_N^{bkg}}{1 - r} \tag{4.4}$$

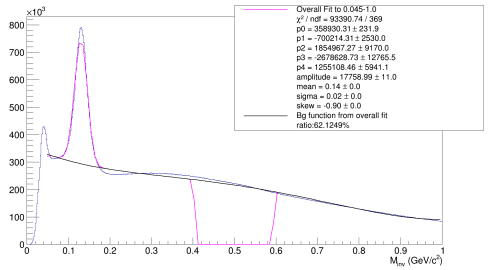

(a) Energy bin $0 - 15$ GeV

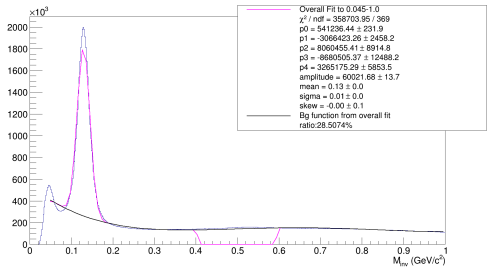

(b) Energy bin $15 - 20$ GeV

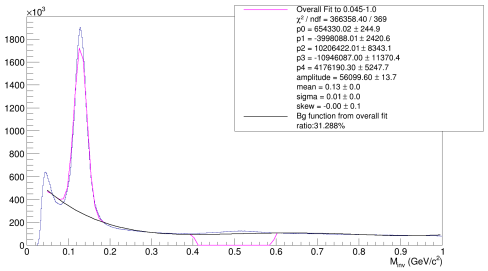

(c) Energy bin $20 - 25$ GeV

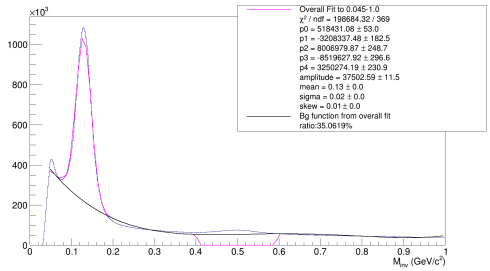

(d) Energy bin $25 - 30$ GeV

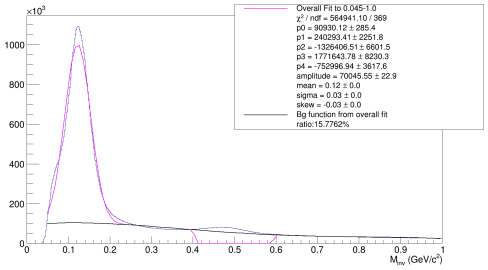

(e) Energy bin $30 - 40$ GeV

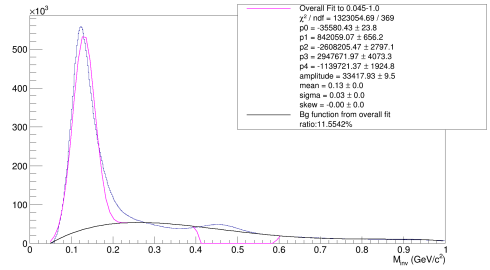

(f) Energy bin $40 - 55$ GeV

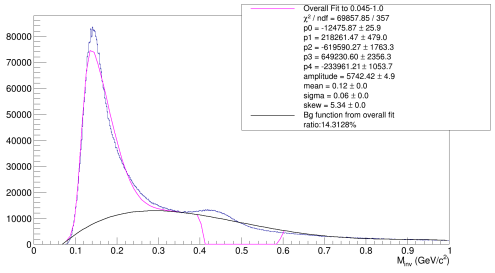

(g) Energy bin $55 - 70$ GeV

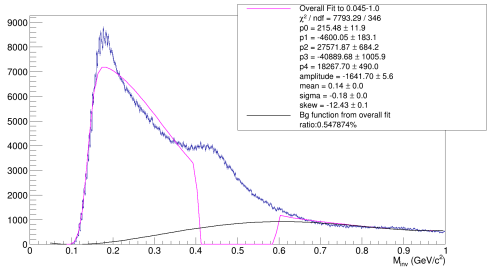

(h) Energy bin $70 - 100$ GeV

Figure 4.15: The invariant mass for the different energy bins along with the overall fit and background function. The ratio is also displayed. The magenta line is the overall fit and the black line is the background function.

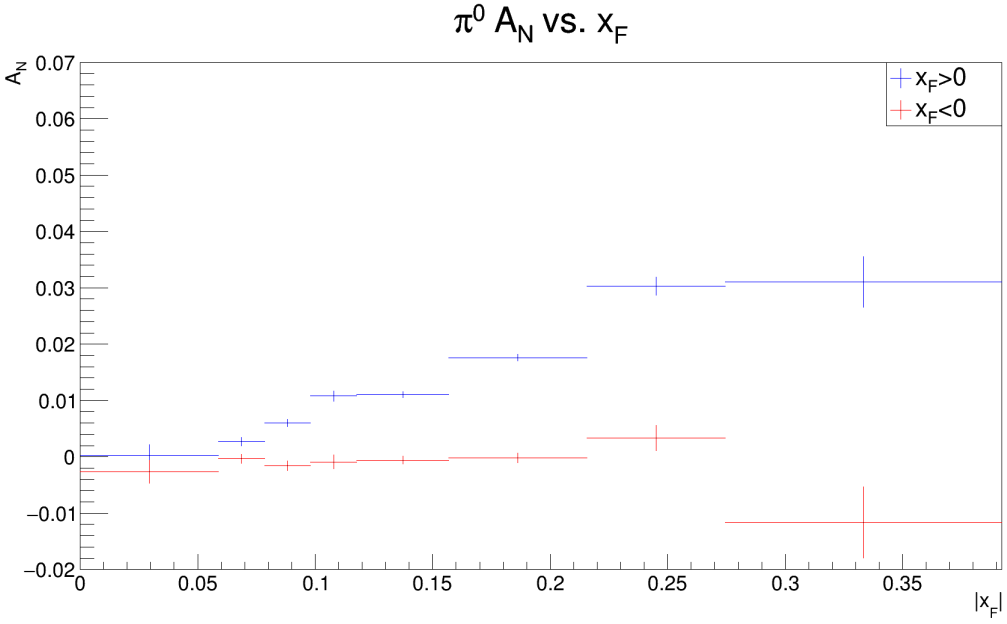

Figure 4.16: Background corrected A_N of π^0's as a function of x_F. For $x_F > 0$ A_N is increasing and for $x_F < 0$ A_N is consistent with zero. Only statistical errors are shown.

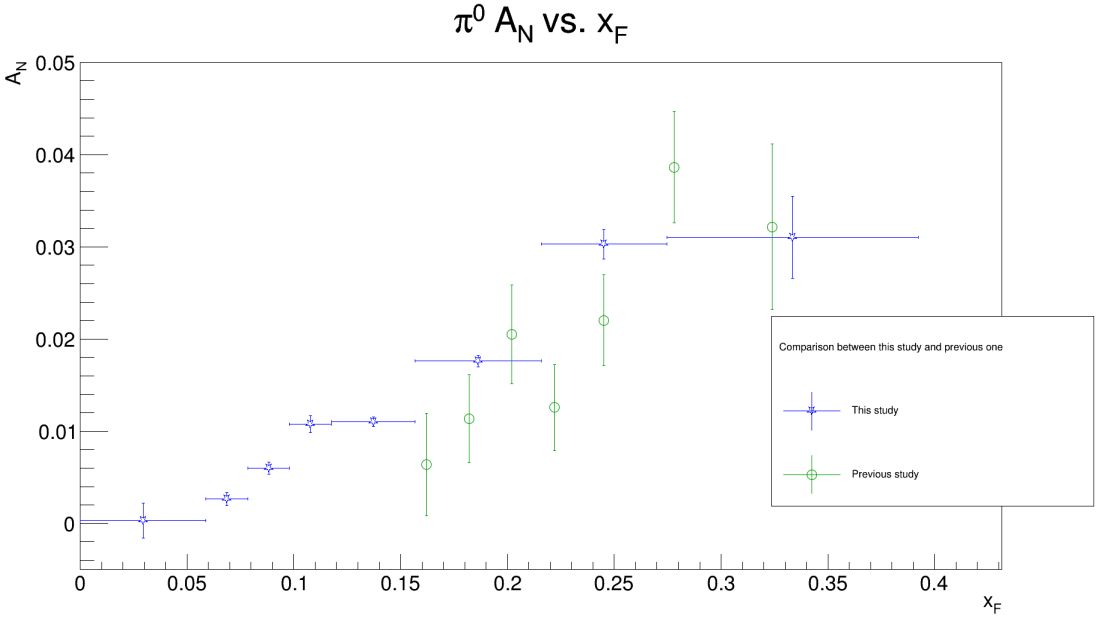

Figure 4.17: Background corrected A_N of π^0's from this study and a previously published result [5] as a function of x_F for only $x_F > 0$. The results are consistent and the statistical errors have been greatly reduced in this dataset.

Chapter 5

Conclusions

The internal structure of the proton and other nuclei is still an open area of research, often with more questions than answers. This new upgrade to STAR's forward capabilities greatly expands its ability to measure the internal properties of the proton. The upgrade which consisted of tracking and calorimetry makes it possible to add critical measurements needed by theory to describe the internal state of the proton. In particular, the calorimeter upgrade performed as expected and we were able to see results from it for the first time. The results are consistent with previous measurements with error bars greatly reduced. The work in this dissertation will be continued to further reduce backgrounds and study the systematics.

Bibliography

[1] I-V Characteristic Curves.

[2] RUN OVERVIEW OF THE RELATIVISTIC HEAVY ION COLLIDER.

[3] A. Abusleme, C. Bélanger-Champagne, A. Bellerive, Y. Benhammou, J. Botte, H. Cohen, M. Davies, Y. Du, L. Gauthier, T. Koffas, S. Kuleshov, B. Lefebvre, C. Li, N. Lupu, G. Mikenberg, D. Mori, J. P. Ochoa-Ricoux, E. Perez Codina, S. Rettie, A. Robichaud-Véronneau, R. Rojas, M. Shoa, V. Smakhtin, B. Stelzer, O. Stelzer-Chilton, A. Toro, H. Torres, P. Ulloa, B. Vachon, G. Vasquez, A. Vdovin, S. Viel, P. Walker, S. Weber, and C. Zhu. Performance of a full-size small-strip thin gap chamber prototype for the ATLAS new small wheel muon upgrade. *Nuclear Instruments and Methods in Physics Research, Section A: Accelerators, Spectrometers, Detectors and Associated Equipment*, 817:85–92, may 2016.

[4] K H Ackermann, N Adams, C Adler, Z Ahammed, S Ahmad, C Allgower, J Amonett, J Amsbaugh, B D Anderson, M Anderson, E Anderssen, H Arnesen, L Arnold, G S Averichev, A Baldwin, J Balewski, O Barannikova, L S Barnby, J Baudot, M Beddo, S Bekele, V V Belaga, R Bellwied, S Bennett, J Bercovitz, J Berger, W Betts, H Bichsel, F Bieser, L C Bland, M Bloomer, C O Blyth, J Boehm, B E Bonner, D Bonnet, R Bossingham, M Botlo, A Boucham, N Bouillo, S Bouvier, K Bradley, F P Brady, A Brandin, R L Brown, G Brugalette, M Burkes, R V Cadman, H Caines, M Calderón de la Barca Sánchez, A Cardenas, L Carr, J Carroll, J Castillo, M Castro, D Cebra, S Chattopadhyay, M L Chen, W Chen, Y Chen, S P Chernenko, M Cherney, A Chikanian, B Choi, J Chrin, W Christie, J P Coffin, L Conin, C Consiglio, T M Cormier, J G Cramer, H J Crawford, I Danilov, D Dayton, M DeMello, W S Deng, A A Derevschikov, M Dialinas, H Diaz, P A DeYoung, L Didenko, D Dimassimo, J Dioguardi, C Drancourt, T Dietel, J E Draper, V B Dunin, J C Dunlop, V Eckardt, W R Edwards, L G Efimov, T Eggert, V Emelianov, J Engelage, G Eppley, B Erazmus, A Etkin, P Fachini, V Faine, C Feliciano, D Ferenc, M I Ferguson, H Fessler, K Filimonov, E Finch, Y Fisyak, D Flierl, I Flores, K J Foley, D Fritz, J Fu, C A Gagliardi, N Gagunashvili, J Gans, L Gaudichet, M Gazdzicki, M Germain, F Geurts, V Ghazikhanian, C Gojak, J Grabski, O Grachov, M Grau, D Greiner, L Greiner, V Grigoriev, D Grosnick, J Gross, M Guedon, G Guilloux, E Gushin, J Hall, T J Hallman, D Hardtke, G Harper, J W Harris, M Heffner, S Heppelmann, T Herston, D Hill,

B Hippolyte, A Hirsch, E Hjort, G W Hoffmann, M Horsley, M Howe, H Z Huang, T J Humanic, H Hümmler, W Hunt, J Hunter, G Igo, A Ishihara, Yu.I. Ivanshin, P Jacobs, W W Jacobs, S Jacobson, M Janik, R Jared, P Jensen, I Johnson, P G Jones, E G Judd, M Kaneta, M Kaplan, D Keane, A Khodinov, J Kiryluk, A Kisiel, J Klay, S R Klein, A Klyachko, G Koehler, A S Konstantinov, I Kotov, M Kopytine, L Kotchenda, A D Kovalenko, M Kramer, P Kravtsov, K Krueger, T Krupien, P Kuczewski, C Kuhn, A I Kulikov, G J Kunde, C L Kunz, R Kh. Kutuev, A A Kuznetsov, L Lakehal-Ayat, M A C Lamont, J M Landgraf, S Lange, C P Lansdell, B Lasiuk, F Laue, A Lebedev, T LeCompte, R Lednický, W J Leonhardt, V M Leontiev, M J LeVine, Q Li, C.-J. Liaw, J Lin, S J Lindenbaum, V Lindenstruth, P J Lindstrom, M A Lisa, F Liu, L Liu, Z Liu, Q J Liu, T Ljubicic, W J Llope, G LoCurto, H Long, R S Longacre, M Lopez-Noriega, W A Love, D Lynn, R Maier, R Majka, S Margetis, C Markert, L Martin, J Marx, H S Matis, Yu.A. Matulenko, C McParland, T S McShane, J Meier, F Meissner, Yu. Melnick, A Meschanin, M Messer, P Middlekamp, B Miller, M L Miller, Z Milosevich, N G Minaev, B Minor, J Mitchell, E Mogavero, V A Moiseenko, D Moltz, C F Moore, V Morozov, M M de Moura, M G Munhoz, G S Mutchler, J M Nelson, P Nevski, M Nguyen, T Nguyen, V A Nikitin, L V Nogach, T Noggle, B Norman, S B Nurushev, T Nussbaum, J Nystrand, G Odyniec, A Ogawa, C A Ogilvie, V Okorokov, K Olchanski, M Oldenburg, D Olson, G Ott, D Padrazo, G Paic, S U Pandey, Y Panebratsev, S Y Panitkin, A I Pavlinov, T Pawlak, V Perevoztchikov, W Peryt, V A Petrov, W Pinganaud, S Pirogov, E Platner, J Pluta, I Polk, N Porile, J Porter, A M Poskanzer, E Potrebenikova, D Prindle, C Pruneau, J Puskar-Pasewicz, G Rai, J Rasson, O Ravel, R L Ray, S V Razin, D Reichhold, J G Reid, R E Renfordt, F Retiere, A Ridiger, J Riso, H G Ritter, J B Roberts, D Roehrich, O V Rogachevski, J L Romero, C Roy, D Russ, V Rykov, I Sakrejda, R Sanchez, Z Sandler, S Salur, J Sandweiss, A C Saulys, I Savin, J Schambach, R P Scharenberg, J Scheblien, R Scheetz, R Schlueter, N Schmitz, L S Schroeder, M Schulz, A Schüttauf, K Schweda, J Sedlmeir, J Seger, D Seliverstov, P Seyboth, R Seymour, E Shahaliev, K E Shestermanov, S S Shimanskii, D Shuman, V S Shvetcov, G Skoro, N Smirnov, L P Smykov, R Snellings, K Solberg, P Sorensen, J Sowinski, H M Spinka, B Srivastava, E J Stephenson, R Stock, A Stolpovsky, N Stone, M Strikhanov, B Stringfellow, H Stroebele, C Struck, A A P Suaide, E Sugarbaker, C Suire, M Šumbera, T J M Symons, A Szanto de Toledo, P Szarwas, A Tai, J Takahashi, A H Tang, A Tarchini, J Tarzian, J H Thomas, M Thompson, V Tikhomirov, M Tokarev, M B Tonjes, S Tonse, T A Trainor, S Trentalange, R E Tribble, V Trofimov, O Tsai, K Turner, T Ullrich, D G Underwood, I Vakula, G Van Buren, A M VanderMolen, A Vanyashin, I M Vasilevski, A N Vasiliev, S E Vigdor, G Visser, S A Voloshin, C Vu, F Wang, H Ward, J W Watson, D Weerasundara, R Weidenbach, R Wells, T Wenaus, G D Westfall, J P Whitfield, C Whitten, H Wieman, R Willson, K Wilson, J Wirth, J Wisdom, S W Wissink, R Witt, J Wolf, J Wood, N Xu, Z Xu, A E Yakutin, E Yamamoto, J Yang, P Yepes, A Yokosawa, V I Yurevich, Y V Zanevski, I Zborovský, H Zhang, W M Zhang, D Zimmerman, R Zoulkarneev, and A N Zubarev. STAR detector overview. *Nuclear Instruments and Methods in Physics Research Section A: Accelerators, Spectrometers, Detectors and Associated Equipment*, 499(2):624–632, 2003.

[5] J Adam, L Adamczyk, J R Adams, J K Adkins, G Agakishiev, M M Aggarwal, Z Ahammed, I Alekseev, D M Anderson, A Aparin, E C Aschenauer, M U Ashraf, F G Atetalla, A Attri, G S Averichev, V Bairathi, K Barish, A Behera, R Bellwied, A Bhasin, J Bielcik, J Bielcikova, L C Bland, I G Bordyuzhin, J D Brandenburg, A V Brandin, J Butterworth, H Caines, M de la Barca Sánchez, D Cebra, I Chakaberia, P Chaloupka, B K Chan, F-H. Chang, Z Chang, N Chankova-Bunzarova, A Chatterjee, D Chen, J Chen, J H Chen, X Chen, Z Chen, J Cheng, M Cherney, M Chevalier, S Choudhury, W Christie, X Chu, H J Crawford, M Csanád, M Daugherity, T G Dedovich, I M Deppner, A A Derevschikov, L Didenko, C Dilks, X Dong, J L Drachenberg, J C Dunlop, T Edmonds, N Elsey, J Engelage, G Eppley, S Esumi, O Evdokimov, A Ewigleben, O Eyser, R Fatemi, S Fazio, P Federic, J Fedorisin, C J Feng, Y Feng, P Filip, E Finch, Y Fisyak, A Francisco, L Fulek, C A Gagliardi, T Galatyuk, F Geurts, N Ghimire, A Gibson, K Gopal, X Gou, D Grosnick, W Guryn, A I Hamad, A Hamed, S Harabasz, J W Harris, S He, W He, X H He, Y He, S Heppelmann, S Heppelmann, N Herrmann, E Hoffman, L Holub, Y Hong, S Horvat, Y Hu, H Z Huang, S L Huang, T Huang, X Huang, T J Humanic, P Huo, G Igo, D Isenhower, W W Jacobs, C Jena, A Jentsch, Y Ji, J Jia, K Jiang, S Jowzaee, X Ju, E G Judd, S Kabana, M L Kabir, S Kagamaster, D Kalinkin, K Kang, D Kapukchyan, K Kauder, H W Ke, D Keane, A Kechechyan, M Kelsey, Y V Khyzhniak, D P Kiko\la, C Kim, B Kimelman, D Kincses, T A Kinghorn, I Kisel, A Kiselev, M Kocan, L Kochenda, L K Kosarzewski, L Kramarik, P Kravtsov, K Krueger, N Kulathunga Mudiyanselage, L Kumar, S Kumar, R Kunnawalkam Elayavalli, J H Kwasizur, R Lacey, S Lan, J M Landgraf, J Lauret, A Lebedev, R Lednicky, J H Lee, Y H Leung, C Li, C Li, W Li, W Li, X Li, Y Li, Y Liang, R Licenik, T Lin, Y Lin, M A Lisa, F Liu, H Liu, P Liu, P Liu, T Liu, X Liu, Y Liu, Z Liu, T Ljubicic, W J Llope, R S Longacre, N S Lukow, S Luo, X Luo, G L Ma, L Ma, R Ma, Y G Ma, N Magdy, R Majka, D Mallick, S Margetis, C Markert, H S Matis, J A Mazer, N G Minaev, S Mioduszewski, B Mohanty, M M Mondal, I Mooney, Z Moravcova, D A Morozov, M Nagy, J D Nam, Md. Nasim, K Nayak, D Neff, J M Nelson, D B Nemes, M Nie, G Nigmatkulov, T Niida, L V Nogach, T Nonaka, A S Nunes, G Odyniec, A Ogawa, S Oh, V A Okorokov, B S Page, R Pak, A Pandav, Y Panebratsev, B Pawlik, D Pawlowska, H Pei, C Perkins, L Pinsky, R L Pintér, J Pluta, B R Pokhrel, J Porter, M Posik, N K Pruthi, M Przybycien, J Putschke, H Qiu, A Quintero, S K Radhakrishnan, S Ramachandran, R L Ray, R Reed, H G Ritter, O V Rogachevskiy, J L Romero, L Ruan, J Rusnak, N R Sahoo, H Sako, S Salur, J Sandweiss, S Sato, W B Schmidke, N Schmitz, B R Schweid, F Seck, J Seger, M Sergeeva, R Seto, P Seyboth, N Shah, E Shahaliev, P V Shanmuganathan, M Shao, A I Sheikh, W Q Shen, S S Shi, Y Shi, Q Y Shou, E P Sichtermann, R Sikora, M Simko, J Singh, S Singha, N Smirnov, W Solyst, P Sorensen, H M Spinka, B Srivastava, T D S Stanislaus, M Stefaniak, D J Stewart, M Strikhanov, B Stringfellow, A A P Suaide, M Sumbera, B Summa, X M Sun, X Sun, Y Sun, Y Sun, B Surrow, D N Svirida, P Szymanski, A H Tang, Z Tang, A Taranenko, T Tarnowsky, J H Thomas, A R Timmins, D Tlusty, M Tokarev, C A Tomkiel, S Trentalange, R E Tribble, P Tribedy, S K Tripathy, O D Tsai, Z Tu, T Ullrich, D G Underwood, I Upsal, G Van Buren, J Vanek, A N Vasiliev, I Vassiliev, F Videb\aek, S Vokal, S A Voloshin,

F Wang, G Wang, J S Wang, P Wang, Y Wang, Y Wang, Z Wang, J C Webb, P C Weidenkaff, L Wen, G D Westfall, H Wieman, S W Wissink, R Witt, Y Wu, Z G Xiao, G Xie, W Xie, H Xu, N Xu, Q H Xu, Y F Xu, Y Xu, Z Xu, Z Xu, C Yang, Q Yang, S Yang, Y Yang, Z Yang, Z Ye, Z Ye, L Yi, K Yip, Y Yu, H Zbroszczyk, W Zha, C Zhang, D Zhang, S Zhang, S Zhang, X P Zhang, Y Zhang, Y Zhang, Z J Zhang, Z Zhang, Z Zhang, J Zhao, C Zhong, C Zhou, X Zhu, Z Zhu, M Zurek, and M Zyzak. Measurement of transverse single-spin asymmetries of π^0 and electromagnetic jets at forward rapidity in 200 and 500 GeV transversely polarized proton-proton collisions. *Phys. Rev. D*, 103(9):92009, may 2021.

[6] J Adam, L Adamczyk, J R Adams, J K Adkins, G Agakishiev, M M Aggarwal, Z Ahammed, I Alekseev, D M Anderson, A Aparin, E C Aschenauer, M U Ashraf, F G Atetalla, A Attri, G S Averichev, V Bairathi, K Barish, A Behera, R Bellwied, A Bhasin, J Bielcik, J Bielcikova, L C Bland, I G Bordyuzhin, J D Brandenburg, A V Brandin, J Butterworth, H Caines, M de la Barca Sánchez, D Cebra, I Chakaberia, P Chaloupka, B K Chan, F-H. Chang, Z Chang, N Chankova-Bunzarova, A Chatterjee, D Chen, J Chen, J H Chen, X Chen, Z Chen, J Cheng, M Cherney, M Chevalier, S Choudhury, W Christie, X Chu, H J Crawford, M Csanád, M Daugherity, T G Dedovich, I M Deppner, A A Derevschikov, L Didenko, C Dilks, X Dong, J L Drachenberg, J C Dunlop, T Edmonds, N Elsey, J Engelage, G Eppley, S Esumi, O Evdokimov, A Ewigleben, O Eyser, R Fatemi, S Fazio, P Federic, J Fedorisin, C J Feng, Y Feng, P Filip, E Finch, Y Fisyak, A Francisco, L Fulek, C A Gagliardi, T Galatyuk, F Geurts, A Gibson, K Gopal, X Gou, D Grosnick, W Guryn, A I Hamad, A Hamed, S Harabasz, J W Harris, S He, W He, X H He, Y He, S Heppelmann, S Heppelmann, N Herrmann, E Hoffman, L Holub, Y Hong, S Horvat, Y Hu, H Z Huang, S L Huang, T Huang, X Huang, T J Humanic, P Huo, G Igo, D Isenhower, W W Jacobs, C Jena, A Jentsch, Y Ji, J Jia, K Jiang, S Jowzaee, X Ju, E G Judd, S Kabana, M L Kabir, S Kagamaster, D Kalinkin, K Kang, D Kapukchyan, K Kauder, H W Ke, D Keane, A Kechechyan, M Kelsey, Y V Khyzhniak, D P Kiko\la, C Kim, B Kimelman, D Kincses, T A Kinghorn, I Kisel, A Kiselev, M Kocan, L Kochenda, D D Koetke, L K Kosarzewski, L Kramarik, P Kravtsov, K Krueger, N Kulathunga Mudiyanselage, L Kumar, S Kumar, R Kunnawalkam Elayavalli, J H Kwasizur, R Lacey, S Lan, J M Landgraf, J Lauret, A Lebedev, R Lednicky, J H Lee, Y H Leung, C Li, C Li, W Li, W Li, X Li, Y Li, Y Liang, R Licenik, T Lin, Y Lin, M A Lisa, F Liu, H Liu, P Liu, P Liu, T Liu, X Liu, Y Liu, Z Liu, T Ljubicic, W J Llope, R S Longacre, N S Lukow, S Luo, X Luo, G L Ma, L Ma, R Ma, Y G Ma, N Magdy, R Majka, D Mallick, S Margetis, C Markert, H S Matis, J A Mazer, N G Minaev, S Mioduszewski, B Mohanty, M M Mondal, I Mooney, Z Moravcova, D A Morozov, M Nagy, J D Nam, Md. Nasim, K Nayak, D Neff, J M Nelson, D B Nemes, M Nie, G Nigmatkulov, T Niida, L V Nogach, T Nonaka, A S Nunes, G Odyniec, A Ogawa, S Oh, V A Okorokov, B S Page, R Pak, A Pandav, Y Panebratsev, B Pawlik, D Pawlowska, H Pei, C Perkins, L Pinsky, R L Pintér, J Pluta, J Porter, M Posik, N K Pruthi, M Przybycien, J Putschke, H Qiu, A Quintero, S K Radhakrishnan, S Ramachandran, R L Ray, R Reed, H G Ritter, O V Rogachevskiy, J L Romero, L Ruan, J Rusnak, N R Sahoo, H Sako, S Salur, J Sandweiss, S Sato, W B Schmidke, N Schmitz, B R

Schweid, F Seck, J Seger, M Sergeeva, R Seto, P Seyboth, N Shah, E Shahaliev, P V Shanmuganathan, M Shao, A I Sheikh, W Q Shen, S S Shi, Y Shi, Q Y Shou, E P Sichtermann, R Sikora, M Simko, J Singh, S Singha, N Smirnov, W Solyst, P Sorensen, H M Spinka, B Srivastava, T D S Stanislaus, M Stefaniak, D J Stewart, M Strikhanov, B Stringfellow, A A P Suaide, M Sumbera, B Summa, X M Sun, X Sun, Y Sun, Y Sun, B Surrow, D N Svirida, P Szymanski, A H Tang, Z Tang, A Taranenko, T Tarnowsky, J H Thomas, A R Timmins, D Tlusty, M Tokarev, C A Tomkiel, S Trentalange, R E Tribble, P Tribedy, S K Tripathy, O D Tsai, Z Tu, T Ullrich, D G Underwood, I Upsal, G Van Buren, J Vanek, A N Vasiliev, I Vassiliev, F Videb\aek, S Vokal, S A Voloshin, F Wang, G Wang, J S Wang, P Wang, Y Wang, Y Wang, Z Wang, J C Webb, P C Weidenkaff, L Wen, G D Westfall, H Wieman, S W Wissink, R Witt, Y Wu, Z G Xiao, G Xie, W Xie, H Xu, N Xu, Q H Xu, Y F Xu, Y Xu, Z Xu, Z Xu, C Yang, Q Yang, S Yang, Y Yang, Z Yang, Z Ye, Z Ye, L Yi, K Yip, Y Yu, H Zbroszczyk, W Zha, C Zhang, D Zhang, S Zhang, S Zhang, X P Zhang, Y Zhang, Y Zhang, Z J Zhang, Z Zhang, Z Zhang, J Zhao, C Zhong, C Zhou, X Zhu, Z Zhu, M Zurek, and M Zyzak. Comparison of transverse single-spin asymmetries for forward π^0 production in polarized pp, pAl and pAu collisions at nucleon pair c.m. energy $\sqrt{s_N N} = 200\ GeV$. *Phys. Rev. D*, 103(7):72005, apr 2021.

[7] Joseph Adams, Annika Ewigleben, Sierra Garrett, Wanbing He, Te-Chuan Huang, Peter M Jacobs, Xinyue Ju, Michael A Lisa, Michael Lomnitz, Robert Pak, Rosi Reed, Alexander Schmah, Prashanth Shanmuganathan, Ming Shao, Xu Sun, Isaac Upsal, Gerard Visser, and Jinlong Zhang. The STAR Event Plane Detector. *Nuclear Instruments and Methods in Physics Research Section A: Accelerators, Spectrometers, Detectors and Associated Equipment*, 968:163970, dec 2019.

[8] Christine A Aidala, Steven D Bass, Delia Hasch, and Gerhard K Mallot. The spin structure of the nucleon. *Reviews of Modern Physics*, 85(2):655–691, apr 2013.

[9] I Alekseev, C Allgower, M Bai, Y Batygin, L Bozano, K Brown, G Bunce, P Cameron, E Courant, S Erin, J Escallier, W Fischer, R Gupta, K Hatanaka, H Huang, K Imai, M Ishihara, A Jain, A Lehrach, V Kanavets, T Katayama, T Kawaguchi, E Kelly, K Kurita, S.Y Lee, A Luccio, W.W MacKay, G Mahler, Y Makdisi, F Mariam, W McGahern, G Morgan, J Muratore, M Okamura, S Peggs, F Pilat, V Ptitsin, L Ratner, T Roser, N Saito, H Satoh, Y Shatunov, H Spinka, M Syphers, S Tepikian, T Tominaka, N Tsoupas, D Underwood, A Vasiliev, P Wanderer, E Willen, H Wu, A Yokosawa, and A.N Zelenski. Polarized proton collider at RHIC. *Nuclear Instruments and Methods in Physics Research Section A: Accelerators, Spectrometers, Detectors and Associated Equipment*, 499(2-3):392–414, mar 2003.

[10] L W Anderson. Optically pumped electron spin polarized targets for use in the production of polarized ion beams. *Nuclear Instruments and Methods*, 167(3):363–370, 1979.

[11] M Anderson, J Berkovitz, W Betts, R Bossingham, F Bieser, R Brown, M Burks, M. Calderón de la Barca Sánchez, D. Cebra, M. Cherney, J Chrin, W.R. Edwards,

V Ghazikhanian, D Greiner, M Gilkes, D Hardtke, G Harper, E Hjort, H Huang, G Igo, S Jacobson, D Keane, S.R. Klein, G Koehler, L Kotchenda, B Lasiuk, A Lebedev, J Lin, M Lisa, H.S. Matis, J Nystrand, S Panitkin, D Reichold, F Retiere, I Sakrejda, K Schweda, D Shuman, R Snellings, N Stone, B Stringfellow, J.H. Thomas, T Trainor, S Trentalange, R Wells, C Whitten, H Wieman, E Yamamoto, and W Zhang. The STAR time projection chamber: a unique tool for studying high multiplicity events at RHIC. *Nuclear Instruments and Methods in Physics Research Section A: Accelerators, Spectrometers, Detectors and Associated Equipment*, 499(2-3):659–678, mar 2003.

[12] M Anselmino, A Efremov, and E Leader. The theory and phenomenology of polarized deep inelastic scattering. *Physics Reports*, 261(1-2):1–124, jan 1995.

[13] L Aphecetche, T C Awes, J Banning, S Bathe, A Bazilevsky, S Belikov, S T Belyaev, C Blume, M Bobrek, D Bucher, V Bumazhnov, H Büsching, S Chernichenkov, V Cianciolo, M Cutshaw, D G D'Enterria, S Daniels, G David, H Delagrange, A Denisov, A Durum, Y V Efremenko, M S Emery, S L Fokin, S Frank, Y Goto, M.Grosse Perdekamp, N Heine, D E Hurst, V V Ikonnikov, M S Ippolitov, G Jackson, J P Jones, K V Karadjev, E Kistenev, C Klein-Bösing, V Kochetkov, Iou.A Koutcheryaev, V A Lebedev, V I Manko, G Martinez, Y Melnikov, T Moore, M Musrock, S A Nikolaev, A S Nyanin, V Onuchin, T Peitzmann, P Pitukhin, F Plasil, K F Read, K Reygers, R Santo, Y Schutz, V Semenov, V Shelikhov, Iou.G Sibiriak, M Simpson, D C Smith, M Smith, A Soldatov, P W Stankus, J Stewering, S P Stoll, H Torii, A A Tsvetkov, N Tyurin, A Usachev, A A Vasiliev, W Verhoeven, A A Vinogradov, M A Volkov, J W Walker, S N White, A L Wintenberg, C L Woody, G R Young, and I E Yushmanov. PHENIX calorimeter. *Nuclear Instruments and Methods in Physics Research Section A: Accelerators, Spectrometers, Detectors and Associated Equipment*, 499(2):521–536, 2003.

[14] V E Barnes, P L Connolly, D J Crennell, B B Culwick, W C Delaney, W B Fowler, P E Hagerty, E L Hart, N Horwitz, P V C Hough, J E Jensen, J K Kopp, K W Lai, J Leitner, J L Lloyd, G W London, T W Morris, Y Oren, R B Palmer, A G Prodell, D č\fii\ifmmode \acutec\else ć\fi, D C Rahm, C R Richardson, N P Samios, J R Sanford, R P Shutt, J R Smith, D L Stonehill, R C Strand, A M Thorndike, M S Webster, W J Willis, and S S Yamamoto. Observation of a Hyperon with Strangeness Minus Three. *Phys. Rev. Lett.*, 12(8):204–206, feb 1964.

[15] F Bianchi, E Castelli, P Checchia, R Cirio, M P Clara, A De Angelis, A Ferrer, G Galeazzi, D Gamba, U Gasparini, M Innocente, L Lanceri, I Lippi, A Lopez, J Marco, C Martinez, M Mazzucato, E Menichetti, M Pegoraro, C Pinori, P Poropat, R Ragazzon, G Rinaudo, A Romero, P Ronchese, A Ruiz, F Scuri, A Sebastia, M Sessa, F Simonetto, J Velasco, L Ventura, F Waldner, and G Zumerle. Transverse profile of electron showers in a lead-glass calorimeter. *Nuclear Instruments and Methods in Physics Research Section A: Accelerators, Spectrometers, Detectors and Associated Equipment*, 279(3):473–478, 1989.

[16] L C Bland, A Ogawa, Yu. A Matulenko, V V Mochalov, D A Morozov, L V Nogach, K E Shestermanov, A N Vasiliev, and G Rakness. An electromagnetic shower profile in the

lead-glass calorimeter in the energy range of 3–23 GeV. *Instruments and Experimental Techniques*, 51(3):342–350, 2008.

[17] R Brandelik and Others. Evidence for a Spin One Gluon in Three Jet Events. *Phys. Lett. B*, 97:453–458, 1980.

[18] J D Brandenburg, Y Chang, J Dong, Y He, Y Hu, B Huang, H Huang, T Huang, H Li, M Nie, R Sharma, X Sun, P Tribedy, F Videbæk, G Visser, G Wilks, P Wang, G Xie, G Yan, Z Ye, L Yi, Y Yang, S Zhang, and Z Zhang. The STAR Forward Silicon Tracker. *Nuclear Instruments and Methods in Physics Research Section A: Accelerators, Spectrometers, Detectors and Associated Equipment*, 1072:170202, 2025.

[19] M Breidenbach, J I Friedman, H W Kendall, E D Bloom, D H Coward, H DeStaebler, J Drees, L W Mo, and R E Taylor. Observed Behavior of Highly Inelastic Electron-Proton Scattering. *Physical Review Letters*, 23(16):935–939, oct 1969.

[20] John C Collins, Steve F Heppelmann, and Glenn A Ladinsky. Measuring transversity densities in singly polarized hadron-hadron and lepton-hadron collisions. *Nuclear Physics B*, 420(3):565–582, 1994.

[21] Ya. S Derbenev, A M Kondratenko, S I Serednyakov, A N Skrinsky, G M Tumaikin, and Yu. M Shatunov. RADIATIVE POLARIZATION: OBTAINING, CONTROL, USING. *Part. Accel.*, 8:115–126, 1978.

[22] Christopher J. Dilks. *Longitudinal Double-Spin Asymmetry of Forward Neutral Pions from $\sqrt{s} = 510$ GeV Polarized Proton-Proton Collisions at STAR.* PhD thesis, The Pennsylvania State University, 2018.

[23] H Geiger and E Marsden. LXI. The laws of deflexion of a particles through large angles. *The London, Edinburgh, and Dublin Philosophical Magazine and Journal of Science*, 25(148):604–623, 1913.

[24] David J. Griffiths. *Introduction to Elementary Particles.* WILEY-VCH Verlag GmbH & Co., second, re edition, 2010.

[25] Matthias Grosse Perdekamp and Feng Yuan. Transverse Spin Structure of the Nucleon. *Annual Review of Nuclear and Particle Science*, 65(1):429–456, oct 2015.

[26] H Hahn, E Forsyth, H Foelsche, M Harrison, J Kewisch, G Parzen, S Peggs, E Raka, A Ruggiero, A Stevens, S Tepikian, P Thieberger, D Trbojevic, J Wei, E Willen, S Ozaki, and S Y Lee. The RHIC design overview. *Nuclear Instruments and Methods in Physics Research Section A: Accelerators, Spectrometers, Detectors and Associated Equipment*, 499(2):245–263, 2003.

[27] Francis Halzen and Martin Alan D. *Quarks and Leptons: An Introductory Course in Modern Particle Physics.* John Wiley & Sons, Inc., 1984.

[28] G Hanson, G S Abrams, A M Boyarski, M Breidenbach, F Bulos, W Chinowsky, G J Feldman, C E Friedberg, D Fryberger, G Goldhaber, D L Hartill, B Jean-Marie, J A Kadyk, R R Larsen, A M Litke, D Lüke, B A Lulu, V Lüth, H L Lynch, C C Morehouse, J M Paterson, M L Perl, F M Pierre, T P Pun, P A Rapidis, B Richter, B Sadoulet, R F Schwitters, W Tanenbaum, G H Trilling, F Vannucci, J S Whitaker, F C Winkelmann, and J E Wiss. Evidence for Jet Structure in Hadron Production by e^+e^- Annihilation. *Phys. Rev. Lett.*, 35(24):1609–1612, dec 1975.

[29] H Huang, L A Ahrens, M Bai, K Brown, E D Courant, C Gardner, J W Glenn, F Lin, A U Luccio, W W MacKay, M Okamura, V Ptitsyn, T Roser, J Takano, S Tepikian, N Tsoupas, A Zelenski, and K Zeno. Overcoming Depolarizing Resonances with Dual Helical Partial Siberian Snakes. *Physical Review Letters*, 99(15):154801, oct 2007.

[30] A A Lednev. Electron shower transverse profile measurement. *Nuclear Instruments and Methods in Physics Research Section A: Accelerators, Spectrometers, Detectors and Associated Equipment*, 366(2):292–297, 1995.

[31] William R. Leo. *Techniques for Nuclear and Particle Physcis Experiments*. Springer-Verlag Berlin Heidelberg GmbH, New York, second rev edition, 1994.

[32] W J Llope, J Zhou, T Nussbaum, G W Hoffmann, K Asselta, J D Brandenburg, J Butterworth, T Camarda, W Christie, H J Crawford, X Dong, J Engelage, G Eppley, F Geurts, J Hammond, E Judd, D L McDonald, C Perkins, L Ruan, J Scheblein, J J Schambach, R Soja, K Xin, and C Yang. The STAR Vertex Position Detector. *Nuclear Instruments and Methods in Physics Research Section A: Accelerators, Spectrometers, Detectors and Associated Equipment*, 759:23–28, 2014.

[33] I Nakagawa, I Alekseev, A Bazilevsky, A Bravar, G Bunce, S Dhawan, K O Eyser, R Gill, W Haeberli, H Huang, Y Makdisi, A Nass, H Okada, E Stephenson, D N Svirida, T Wise, J Wood, K Yip, and A Zelenski. RHIC polarimetry. *The European Physical Journal Special Topics*, 162(1):259–265, 2008.

[34] S Navas, C Amsler, T Gutsche, C Hanhart, J. J. Hernández-Rey, C. Lourenço, A Masoni, M Mikhasenko, R. E. Mitchell, C Patrignani, C Schwanda, S Spanier, G Venanzoni, C. Z. Yuan, K Agashe, G Aielli, B. C. Allanach, J Alvarez-Muñiz, M Antonelli, E. C. Aschenauer, D. M. Asner, K Assamagan, H Baer, Sw. Banerjee, R. M. Barnett, L Baudis, C. W. Bauer, J. J. Beatty, J Beringer, A Bettini, O Biebel, K. M. Black, E Blucher, R Bonventre, R. A. Briere, A Buckley, V. D. Burkert, M. A. Bychkov, R. N. Cahn, Z Cao, M Carena, G Casarosa, A Ceccucci, A Cerri, R. S. Chivukula, G Cowan, K Cranmer, V Crede, O Cremonesi, G. D'Ambrosio, T Damour, D de Florian, A de Gouvêa, T DeGrand, S Demers, Z Demiragli, B. A. Dobrescu, M. D'Onofrio, M Doser, H. K. Dreiner, P Eerola, U Egede, S Eidelman, A. X. El-Khadra, J Ellis, S. C. Eno, J Erler, V. V. Ezhela, A Fava, W Fetscher, B. D. Fields, A Freitas, H Gallagher, T Gershon, Y Gershtein, T Gherghetta, M. C. Gonzalez-Garcia, M Goodman, C Grab, A. V. Gritsan, C Grojean, D. E. Groom, M Grünewald, A Gurtu, H. E. Haber, M Hamel, S Hashimoto, Y Hayato, A Hebecker, S Heinemeyer, K Hikasa, J Hisano, A Höcker, J Holder, L Hsu, J Huston, T Hyodo, Al. Ianni, M Kado, M Karliner, U. F.

Katz, M Kenzie, V. A. Khoze, S. R. Klein, F Krauss, M Kreps, P. Križan, B Krusche, Y Kwon, O Lahav, L. P. Lellouch, J Lesgourgues, A. R. Liddle, Z Ligeti, C.-J. Lin, C Lippmann, T. M. Liss, A Lister, L Littenberg, K. S. Lugovsky, S. B. Lugovsky, A Lusiani, Y Makida, F Maltoni, A. V. Manohar, W. J. Marciano, J Matthews, U.-G. Meißner, I.-A. Melzer-Pellmann, P Mertsch, D. J. Miller, D Milstead, K Mönig, P Molaro, F Moortgat, M Moskovic, N Nagata, K Nakamura, M Narain, P Nason, A Nelles, M Neubert, Y Nir, H. B. O'Connell, C. A. J. O'Hare, K. A. Olive, J. A. Peacock, E Pianori, A Pich, A Piepke, F Pietropaolo, A Pomarol, S Pordes, S Profumo, A Quadt, K Rabbertz, J Rademacker, G Raffelt, M Ramsey-Musolf, P Richardson, A Ringwald, D. J. Robinson, S Roesler, S Rolli, A Romaniouk, L. J Rosenberg, J. L. Rosner, G Rybka, M. G. Ryskin, R. A. Ryutin, B Safdi, Y Sakai, S Sarkar, F Sauli, O Schneider, S Schönert, K Scholberg, A. J. Schwartz, J Schwiening, D Scott, F Sefkow, U Seljak, V Sharma, S. R. Sharpe, V Shiltsev, G Signorelli, M Silari, F Simon, T Sjöstrand, P Skands, T Skwarnicki, G. F. Smoot, A Soffer, M. S. Sozzi, C Spiering, A Stahl, Y Sumino, F Takahashi, M Tanabashi, J Tanaka, M. Taševský, K Terao, K Terashi, J Terning, U Thoma, R. S. Thorne, L Tiator, M Titov, D. R. Tovey, K Trabelsi, P Urquijo, G Valencia, R. Van de Water, N Varelas, L Verde, I Vivarelli, P Vogel, W Vogelsang, V Vorobyev, S. P. Wakely, W Walkowiak, C. W. Walter, D Wands, D. H. Weinberg, E. J. Weinberg, N Wermes, M White, L. R. Wiencke, S Willocq, C. L. Woody, R. L. Workman, W.-M. Yao, M Yokoyama, R Yoshida, G Zanderighi, G. P. Zeller, R.-Y. Zhu, S.-L. Zhu, F Zimmermann, P. A. Zyla, J Anderson, M Kramer, P Schaffner, and W Zheng. Review of Particle Physics. *Physical Review D*, 110(3):030001, aug 2024.

[35] H Okada, I Alekseev, A Bravar, G Bunce, S Dhawan, K O Eyser, R Gill, W Haeberli, H Huang, O Jinnouchi, Y Makdisi, I Nakagawa, A Nass, N Saito, E Stephenson, D Sviridia, T Wise, J Wood, and A Zelenski. Absolute polarimetry at RHIC. *AIP Conference Proceedings*, 980(1):370–379, feb 2008.

[36] Satoshi Ozaki and Thomas Roser. Relativistic Heavy Ion Collider, its construction and upgrade. *Progress of Theoretical and Experimental Physics*, 2015(3):3A102–0, jan 2015.

[37] Slawomir Piatek. What is an SiPM and how does it work?, 2016.

[38] E Rutherford. LXXIX. The scattering of α and β particles by matter and the structure of the atom. *The London, Edinburgh, and Dublin Philosophical Magazine and Journal of Science*, 21(125):669–688, 1911.

[39] V. Schoefer, E.C. Aschenauer, D. Bruno, K.A. Drees, W. Fischer, C.J. Gardner, K. Hock, H. Huang, R.L. Hulsart, C. Liu, Y. Luo, I. Marneris, G.J. Marr, A. Marusic, K. Mernick, R.J. Michnoff, M.G. Minty, J. Morris, F. Méot, A. Poblaguev, V. Ptitsyn, V.H. Ranjbar, D. Raparia, G. Robert-Demolaize, J. Sandberg, W.B. Schmidke, F. Severino, T.C. Shrey, P. Thieberger, J.E. Tuozzolo, M. Valette, K. Yip, A. Zaltsman, A. Zelenski, and K. Zeno. RHIC Polarized Proton Operation in Run 22. In *Proc. 13th International Particle Accelerator Conference (IPAC'22)*, number 13 in Interna-

tional Particle Accelerator Conference, pages 1765–1767. JACoW Publishing, Geneva, Switzerland, 07 2022.

[40] Dennis Sivers. Single-spin production asymmetries from the hard scattering of pointlike constituents. *Physical Review D*, 41(1):83–90, jan 1990.

[41] P Soding, B Wiik, G Wolf, and S L Wu. The First evidence for three jet events in e+ e- collisions at PETRA: First direct observation of the gluon. In *International Europhysics Conference on High-energy Physics (HEP 95)*, pages 3–14, 1996.

[42] A A Sokolov and I M Ternov. On polarization and spin effects in the theory of synchrotron radiation. *Dokl. Akad. Nauk SSSR*, 153(5):1052–1054, 1963.

[43] STAR Collaboration. The STAR Forward Calorimeter System and Forward Tracking System.

[44] STAR Collaboration. The STAR Forward Calorimeter System and Forward Tracking System beyond BES-II.

[45] J Takano, L A Ahrens, R Alforque, M Bai, K Brown, E D Courant, G Ganetis, C J Gardner, J W Glenn, T Hattori, H Huang, A Jain, A U Luccio, W W MacKay, M Okamura, T Roser, N Tsoupas, S Tepikian, J Tuozzolo, J Wood, A Zelenski, and K Zeno. Helical dipole partial Siberian snake for the AGS. *Journal of Instrumentation*, 1(11):P11002–P11002, nov 2006.

[46] John R. Taylor, Chris D. Zafiratos, and Michael A. Dubson. *Modern Physics For Scientists And Engineers*. Pearson Education Inc., second edi edition, 2004.

[47] Yiqun Wang. *Measurement of the Inclusive Forward Neutral Pion Production in 200 GeV Polarized Proton-Proton Collisions at RHIC*. PhD thesis, The University of Texas at Austion, 2004.

[48] C A Whitten Jr. and STAR Collaboration. The Beam-Beam Counter: A Local Polarimeter at STAR. *AIP Conference Proceedings*, 980(1):390–396, feb 2008.

[49] A N Zelenski, V Klenov, S A Kokhanovski, V Zoubets, G Dutto, C D P Levy, G W Wight, J Alessi, and Y Mori. Optically pumped polarized H^- ion sources for RHIC and HERA colliders. *Hyperfine Interactions*, 127(1):475–479, 2000.

[50] Anatoli Zelenski. Optically-pumped polarized h^- and 3he++ ion sources development at rhic. Brookhaven National Lab. (BNL), Upton, NY (United States), 04 2018.

[51] Zhanwen Zhu. *Measurement fo the Transverse Single Spin Asymmetry for π^0 at Forward Direction in 200 and 500 GeV Polarized Proton-Proton Collisions at RHIC-STAR*. PhD thesis, Shandong University, 2019.

Appendix A

Peak Fitting

In order to quickly process and accurately determine the energy from the ADC vs. Tb data as seen in 2.23 a new peak finding method has been developed that will allow the elimination of peaks coming from noise. This method works because using first and second derivatives on noisy data results in noisy derivatives which can give a lot of false peaks. This method which I call peak tunneling assigns a probability to each found peak and then if the probability is below some threshold, then it will merge that peak with another on the left or the right again depending on which has the lower probability. The probability function combines two aspects of a found peak. The distance between the start and end points and the height of the found peak compared to the line formed by the start and end points. The probability function for the distance between the start and end points is given by eq. A.1

$$P_width(x_s, x_e) = \frac{1}{a * (x_e - x_s)^2 + 1} \tag{A.1}$$

Where a is some scale factor to be set, x_s is the x-value where the peak starts, and x_e is the x-value where the peak ends. This form was chosen because it has a range from 0 to 1 where it asymptotically approaches 0 as $(x_e - x_s)$ goes to infinity. Also the behavior near $(x_e - x_s) = 0$ is flat and so it more likely to stay 1 for smaller differences.

The probability coming from the height assumes that the points in y follow a uniform distribution about some mean. For this reason, the complimentary error function (Erfc) was chosen as it is the probability function for normally distributed data; the probability function is given by eq. A.2

$$P_{height} = Erfc\left(\frac{heightdiff}{\sqrt{2}\sigma}\right) \tag{A.2}$$

Where σ is the standard deviation from that normally distributed data and is user entered. The $heightdiff$ is determined by making a line from the start and end points of the peak window and then evaluating that line at the x-value of the peak. This value effectively acts as the "mean" of the normally distributed data. The difference between the peak height and the value just described is the $heightdiff$ and is given in eq. A.3, where $yline$ is the line formed from the points $x_s,\ y_s,\ x_e,\ y_e$ where y_s and y_e are the y values of the data at x_s and x_e respectively.

$$heightdiff = p_y - yline(p_x) \tag{A.3}$$

The total probability is then the multiplication of P_{width} and P_{height} from eq. A.1 and A.2 respectively. This gives the total probability that a given peak window is NOT a peak, thus a probability of 1 means not a peak, and a probability of 0 means a real peak.

For the method to work, three values are needed to be given and should be based on the information about the data you are using, they are: a for scaling in x, s for scaling in y, and a threshold. These variables are illustrated in fig. A.1.

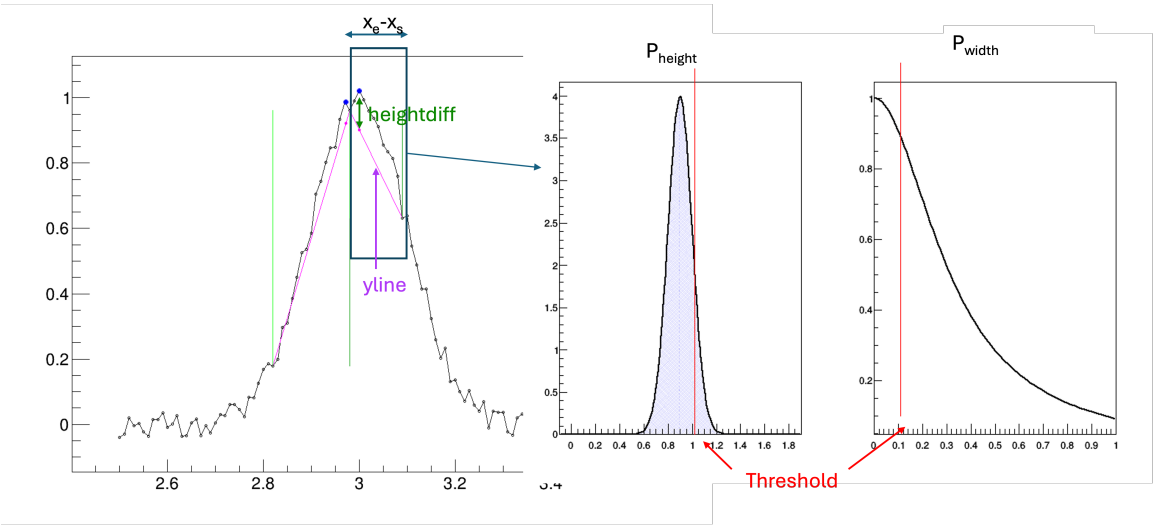

Figure A.1: An illustration showing how the variables in eq. A.1, A.2, and A.3 are computed on a simulated noisy Gaussian.

An example using a Gaussian peak with some noise is shown in fig. A.2. Subfigure a of fig. A.2 is using just a simple first and second derivative test and subfig. b of fig. A.2 shows after using the peak tunneling method. The "noise" is absorbed into the main peak in b. In this simple test I know the noise level and can adjust the parameters accordingly but for real data those parameters need to be tested to find the optimal values.

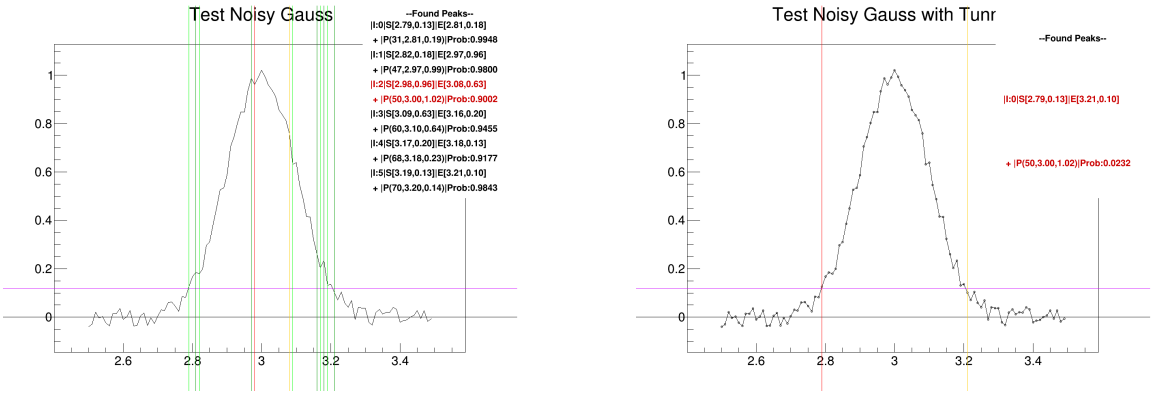

(a) Using just second derivative method

(b) Using peak tunneling

Figure A.2: Illustrating the use of peak tunneling on a simulated Gaussian with noise.